

Synthesis and Characterization of Core-Shell
Electrocatalysts for Fuel Cells Application

Dissertation

zur Erlangung des Doktorgrades der Naturwissenschaften

(Dr. rer. nat.)

der

Naturwissenschaftlichen Fakultät II

Chemie, Physik und Mathematik

der Martin-Luther-Universität

Halle-Wittenberg

vorgelegt von

Frau Heba Ali Ibrahim Khalil El Deeb

geb. am 07.06.1981 in Alexandria, Ägypten

Gutachter:

Prof. Dr. Michael Bron

Prof. Dr. Matthias Arenz

Halle (Saale), 2017

*Dedicate to my Mother and
the Soul of my Father*

Declaration

I hereby declare that the thesis has not been handed in at any other university for reasons of graduation. I declare under penalty of perjury that this thesis is entirely my own work and has been written without any help of others. I only used the mentioned sources and indicated all kind of citations correctly.

Date of submission: 29.09.2016

Date of oral presentation: 10.03.2017

Heba Ali Ibrahim Khalil El Deeb

Halle (Saale),

Table of Contents

Table of contents.....	i
Table captions	iv
Figure captions.....	v
List of abbreviations.....	ix
List of symbols.....	xi
Abstract.....	xiii
English Abstract.....	xiii
German Abstract.....	xv
1 Introduction.....	1
1.1 Fuel Cells: Principle and Classification.....	1
1.2 Polymer Electrolyte Membrane Fuel Cell (PEMFC)	3
1.3 Oxygen Reduction Reaction in the PEM Fuel Cell	5
1.3.1 ORR Mechanism	5
1.3.2 ORR Kinetics on Pt: The Origin of Sluggish ORR.....	8
1.3.3 Pt-Based Alloy Electrocatalysts for ORR	9
1.3.4 Core/Shell Nanoparticles.....	11
1.3.5 Dealloyed Pt-based Bimetallic Electrocatalysts for ORR.....	13
1.4 Aim of the Work.....	15
2 Experimental Work.....	16
2.1 Materials	16
2.2 Methods	17
2.2.1 Microwave-Assisted Polyol Synthesis of PtCu/CNTs Catalysts.....	17
2.2.2 PtCu/CNTs Electrocatalysts Synthesised by NaBH ₄ -Assisted Polyol-Reduction	19
2.2.3 Synthesis of the Chemically Dealloyed PtCu/CNTs Catalysts	20
2.2.4 Cu@Pt/CNTs Catalysts Synthesis.....	21

Table of Contents

2.3	Electrocatalyst Characterization	23
2.3.1	Structural Characterization	23
2.3.2	Electrochemical Characterization.....	24
3	Microwave-Assisted Polyol Synthesis of PtCu/Carbon Nanotube Catalysts for Electrochemical Oxygen Reduction.....	30
3.1	Introduction.....	30
3.2	Electrochemical Measurements Protocol.....	31
3.3	Results and Discussion	32
3.3.1	Metal Loading and Catalyst Composition	32
3.3.2	TEM and XRD Characterization	33
3.3.3	Electrochemical Characterization.....	37
3.4	Conclusions.....	45
4	Electrochemical Dealloying of PtCu/CNTs Electrocatalysts Synthesised by NaBH₄-Assisted Polyol-Reduction: Influence of Preparation Parameters on Oxygen Reduction Activity	47
4.1	Introduction.....	47
4.2	Electrochemical Measurements Protocol.....	47
4.3	Result and Discussion	48
4.3.1	XRD Characterization	48
4.3.2	ICP-OES and TEM Characterization	49
4.3.3	Electrochemical Characterization.....	54
4.4	Conclusions.....	63
4.5	Supporting Information.....	64
5	Electrocatalytic Reduction of Oxygen on Chemically Dealloyed PtCu/CNTs Catalyst: Influence of Dealloying Time on Structure and Activity	67
5.1	Introduction.....	67
5.2	Electrochemical Measurements Protocol.....	67

Table of Contents

5.3	Results and Discussion	68
5.4	Conclusions.....	81
5.5	Supporting Information.....	82
6	Enhanced Oxygen Reduction Reaction Activity on Core-Shell Nanocatalysts Synthesized via Dealloying of Cu@Pt/CNTs Catalyst.	83
6.1	Introduction.....	83
6.2	Electrochemical Measurements Protocol.....	83
6.3	Results and Discussion	84
6.3.1	Structural Characterization	84
6.3.2	Electrochemical Characterization.....	93
6.4	Conclusion	104
6.5	Supporting information.....	105
7	General Discussion	108
8	Appendices	117
8.1	Acknowledgment	117
8.2	Curriculum Vitae	118
8.3	List of Publications	120
8.3.1	Research Articles	120
8.3.2	Conferences Contributions	120
9	References	121

Table Captions
Chapter 3

Table 3.1: Pt-Cu alloy atomic ratios and the Wt.% measured by TGA and ICP-OES..... 33

Table 3.2: Structural parameters evaluated from the XRD and TEM analysis. 37

Table 3.3: Electrochemical surface area (ECSA), average number of electrons (n) at 0.4 V vs. RHE, mass and surface specific activity (i_m and i_s respectively) of the electrochemically dealloyed PtCu catalysts. ... 41

Chapter 4

Table 4.1: XRD data established from the 111 peak, TEM and ICP-OES data analysis of the alloyed PtCu/CNTs catalysts..... 51

Table 4.2: Electrochemical data of the dealloyed PtCu/CNTs catalysts and Pt/C. 60

Chapter 5

Table 5.1: Catalysts crystallite and particle size and the corresponding ICP-OES metal ratio. 70

Table 5.2: XPS parameters. 71

Chapter 6

Table 6.1: Average particle size established from TEM and XRD parameters. 86

Table 6.2: Total metal loading in Wt. % estimated from the ICP-OES and TGA analysis, and the Pt:Cu atomic ratio determined from the XRD, ICP-OES and XPS of the Pt/CNTs catalysts, the alloyed Cu@Pt_x catalysts and the chemically dealloyed catalysts..... 89

Table 6.3: Q_H values, Q_{CO} values, the ECSA obtained from H_{upd} and CO stripping, and the $Q_{CO}/2Q_H$ ratio of the Pt/CNTs, Pt/CNTs_{HT} and the electro/chemical dealloyed catalysts, the charges were normalized to the electrode geometric area. 98

Table 6.4: Electrochemical kinetics parameters extracted from the ORR polarization curves: the half wave potential ($E_{1/2}$), mass specific activity (i_m), surface specific activity (i_s), average number of electrons (n) at 0.6 V vs. RHE and Tafel slope. 102

Chapter 7

Table 7.1: PtCu alloy catalysts, dealloying conditions and the ORR activity with respect to the literatures. 112

Table 7.2: Electrochemical active surface area (ECSA), mass (i_m), and surface (i_s) specific activities of the optimized PtCu catalysts, in comparison with the pure benchmark Pt/C catalyst..... 115

Figure Captions
Chapter 1

Figure 1.1: The major types of fuel cells and their electrodes reactions, where: A.R is the anodic reaction, and C.R is the cathodic reaction.	3
Figure 1.2: Schematic representation of single PEM fuel cell.	4
Figure 1.3: Oxygen reduction reaction pathways in acidic solution (redrawn after [16]).	6
Figure 1.4: Oxygen reduction reaction pathways on the catalyst surface depending on the oxygen interaction types (modified after [19]).	7
Figure 1.5: Trends in oxygen reduction activity plotted as a function of the oxygen binding energy [20].	9
Figure 1.6: Schematic representation of the ligand effect in bimetallic catalyst, where: ϵ_d and ϵ_f referring to the d-band center and Fermi level respectively (modified after [34]).	10
Figure 1.7: Schematic representation of the strain effect in bimetallic catalyst, where: ϵ_d and ϵ_f referring to the d-band center and Fermi level respectively (modified after [34]).	11
Figure 1.8: Core-Shell structure.	12

Chapter 2

Figure 2.1: START 1500 Microwave reactor.	18
Figure 2.2: Schematic illustration for Cu@Pt _x catalysts preparation.	22
Figure 2.3: A) GC rotating disk electrode, and B) casted GC electrode storage system.	25
Figure 2.4: Electrochemical set-up used for the electrochemical measurements.	26
Figure 2.5: One compartment three-electrode electrochemical cell, 1) Reversible hydrogen electrode (RHE), 2) working electrode, 3) counter electrode, 4) gas inlet.	26
Figure 2.6: Linear voltammograms of the oxygen reduction measured on Pt/C catalyst at an electrode rotation speed of 900 rpm, sweep rate of 5 mV s ⁻¹ in O ₂ -saturated 0.1 M HClO ₄ electrolyte.	27
Figure 2.7: CO stripping voltammogram of Pt/C catalyst conducted in N ₂ -purged 0.1M HClO ₄ at a sweep rate of 20 mV s ⁻¹	28
Figure 2.8: Cyclic voltammograms of Pt/C catalyst conducted in N ₂ -purged 0.1 M HClO ₄ and with sweep rate of 100 mV s ⁻¹	29

Chapter 3

Figure 3.1: TEM image of the prepared catalysts A) PtCu/PVP ₆₀₀ , B) PtCu/PVP ₅₀₀ , C) PtCu/PVP ₄₀₀ , D) PtCu/PVP _{pH=11} , E) PtCu/PVP _{pH=8} , F) PtCu.	34
Figure 3.2: XRD diffractograms of, A) PtCu/PVP ₆₀₀ , B) PtCu/PVP _{pH=8} , C) PtCu/PVP _{pH=11} , D) PtCu.	36
Figure 3.3: XRD patterns of the sample PtCu/PVP alloyed at different temperatures; Ref. refers to the as-prepared PtCu/PVP catalyst.	36

Figure Captions

Figure 3.4: Cyclic voltammograms of the as-prepared (solid line) and dealloyed (dashed line) catalysts: A) PtCu/PVP ₆₀₀ , B) PtCu/PVP ₅₀₀ , C) PtCu/PVP ₄₀₀ , D) PtCu/PVP _{pH=11} , E) PtCu/PVP _{pH=8} , and F) PtCu conducted in N ₂ -purged 0.1 M HClO ₄ , and scan rate of 100 mV s ⁻¹	40
Figure 3.5: CO stripping voltammograms for all dealloyed catalysts obtained in N ₂ -saturated 0.1 M HClO ₄ with sweep rate of 20 mV s ⁻¹	42
Figure 3.6: Single sweep voltammograms of the oxygen reduction measured on dealloyed PtCu catalysts at an electrode rotation speed of 900 rpm, sweep rate of 5 mV s ⁻¹ in O ₂ -saturated 0.1 M HClO ₄ electrolyte.....	43
Figure 3.7: Koutecky-Levich plots for oxygen reduction reaction on dealloyed catalysts at 0.4 V vs. RHE, as obtained from RDE measurements in O ₂ -saturated 0.1 M HClO ₄ (comp. Figure 3.6).....	44
Chapter 4	
Figure 4.1: XRD pattern of the prepared electrocatalysts A) Pt/C, B) PtCu _{10SM} , C) PtCu _{10SC} , D) PtCu _{50SM} , E) PtCu _{50MS} , and F) PtCu _{50S}	49
Figure 4.2: TEM images of the prepared catalysts.....	53
Figure 4.3: Initial CVs (black line) in comparison with the final CV of the dealloyed samples (red line), A) Pt/C, B) PtCu _{10SM} , C) PtCu _{10SC} , D) PtCu _{50SM} , E) PtCu _{50MS} and F) PtCu _{50S}	55
Figure 4.4: CO stripping voltammograms for the catalysts: A) Pt/C, B) PtCu _{10SM} , C) PtCu _{10SC} , D) PtCu _{50SM} , E) PtCu _{50MS} and F) PtCu _{50S}	56
Figure 4.5: A) polarization curves of the dealloyed PtCu/CNTs and Pt/C catalysts, B) Koutecky-Levich plots for ORR at 0.6 V vs. RHE.....	59
Figure 4.6: Cyclic voltammetric profiles of PtCu _{50SM} catalyst for six consecutive days A) before dealloying, B) after dealloying.....	61
Figure 4.7: Effect of catalyst ink aging on the electrochemical performance of PtCu _{50SM} catalyst (the results of <i>i_m</i> and <i>i_s</i> was taken from the ORR polarization curve in O ₂ -saturated 0.1 M HClO ₄ , at 0.9 V vs. RHE and 900 rpm rotation rate).....	62
Figure SI 4.1: A) TGA analysis for the PtCu _{10SM} and PtCu _{50SM} catalysts prepared without PVP, B) TEM image for PtCu _{50SM} catalysts prepared without PVP shows the importance of introducing the PVP in during the peroration steps to avoid particles agglomeration.....	64
Figure SI 4.2: Temperature profile for the microwave synthesis of PtCu _{50MS}	65
Figure SI 4.3: XRD pattern of the unalloyed PtCu50MS catalyst.....	66
Figure SI 4.4: XPS of PtCu50SM, the stoichiometric ratio was found to be Pt33Cu66 before dealloying and Pt68Cu32 after the dealloying.....	65

Chapter 5

Figure 5.1: XRD pattern of the dealloyed catalysts A) PtCu, B) PtCu _{15min} , C) PtCu _{1h} , D) PtCu _{2h} , E) PtCu _{4h} and F) PtCu _{6h}	70
Figure 5.2: XPS spectra of the PtCu, PtCu _{15min} and PtCu _{6h} catalysts.....	71
Figure 5.3: TEM image and the corresponding histogram of A) PtCu, B) PtCu _{15min} , C) PtCu _{1h} , D) PtCu _{2h} , E) PtCu _{4h} , and F) PtCu _{6h} catalysts.....	73
Figure 5.4: A) Cyclic voltammogram profiles of the dealloyed catalysts in N ₂ -saturated 0.1 M HClO ₄ at 100 mV s ⁻¹ scan rate, B) electrochemical active surface area estimated from the CO and H _{upd} stripping peak as a function in dealloying time.	75
Figure 5.5: Schematic illustrates the formation and collapse of the Pt-rich skin alloy core structure as a function in the dealloying time.	76
Figure 5.6: A) ORR polarization curves of the dealloyed catalysts compared to the alloy precursor (black solid line) performed in O ₂ -saturated 0.1 M HClO ₄ at scan rate 5 mV s ⁻¹ with a rotation rate of 900 rpm, B) Koutecky-Levich plot at 0.4 V vs. RHE.....	78
Figure 5.7: Number of electrons estimated from the K-L plot as a function in dealloying time.	79
Figure 5.8: A) the mass activity (<i>i_m</i>) and B) the specific activity (<i>i_s</i>) of the dealloyed catalysts as a function in dealloying time, the activities were estimated at 0.9 V vs. RHE.....	80
Figure SI 5.1: A) The initial CV profile of the PtCu alloy precursor and the voltammetrically activated one, B) CO stripping voltammogram of the activated PtCu alloy and the dealloyed catalysts.....	82

Chapter 6

Figure 6.1: XRD patterns of the as-prepared catalysts.	87
Figure 6.2: A) TGA curves of the as-prepared and heat treated Pt/CNTs catalysts; inset: DTG curves, B) Microwave heating profile of the Pt-PVP/EG mixture.	88
Figure 6.3: TGA curves of the as-annealed Cu@Pt _x catalysts.....	89
Figure 6.4: TEM images of the catalysts: A) Pt/CNTs, B) Pt/CNTs _{HT} , C) Cu@Pt ₆₀₀ , D) Cu@Pt ₈₀₀ , E) Cu@Pt ₁₀₀₀ , F) Cu@Pt _{1h} , G) Cu@Pt _{4h}	92
Figure 6.5: Initial cyclic voltammograms of the alloyed catalysts Cu@Pt ₆₀₀₋₁₀₀₀	93
Figure 6.6: Cyclic voltammograms of: A) Pt/CNTs catalyst, B) the electrochemically dealloyed Cu@Pt _x catalysts and C) chemical dealloyed Cu@Pt ₁₀₀₀ catalysts (in N ₂ -saturated 0.1 M HClO ₄ , 100 mV s ⁻¹ scan rate).....	96
Figure 6.7: Representative CO stripping voltammogram of the Pt catalysts and the electrochemically/chemically dealloyed Cu@Pt _x catalysts in N ₂ -saturated 0.1 M HClO ₄ and sweep rate of 20 mV s ⁻¹	98

Figure Captions

Figure 6.8: ORR polarization curves of different catalysts conducted in O_2 -saturated 0.1 M $HClO_4$ at various rotation speed and scanning rate of 5 mV s^{-1}	100
Figure 6.9: A) Koutecky-Levich plots produced from the ORR polarization curves, B) ORR polarization curves of the different catalysts in O_2 -saturated 0.1 M $HClO_4$ at rotation speed of 900 rpm and scanning rate of 5 mV s^{-1} and, C) Tafel plots of the different catalysts.....	103
Figure SI 6.1: HRTEM of Cu@Pt_4h catalyst.	105
Figure SI 6.2: EDX-STEM analysis of the chemical dealloyed Cu@Pt_4h catalyst.	105
Figure SI 6.3: Dealloying cycles of the Cu@Pt_600 catalyst, the segregated Cu surface was completely absent after performing 200 CVs with sweep rate of 200 mV s^{-1} in N_2 -saturated 0.1M $HClO_4$ solution resulting in a stable Pt-like CV profile.	106
Figure SI 6.4: ORR polarization curves of the different catalysts in O_2 -saturated 0.1M $HClO_4$ at various rotation speed and scanning rate of 5 mVs^{-1}	107

Chapter 7

Figure 7.1: Comparison between the PtCu alloy nanoparticles synthesis strategies in terms of the synthesis conditions and observations.....	110
--	-----

List of Abbreviations

AFCs	Alkaline fuel cells
A.R	Anodic reaction
CE	Counter electrode
CNTs	Carbon nanotubes
C.R	Cathodic reaction
CV	Cyclic voltammetry
DFT	Density functional theory
DMFCs	Direct methanol fuel cells
ECSA	Electrochemical active surface area
EDAX	Energy-dispersive X-ray analysis
EG	Ethylene glycol
FCC	Face centered cubic
FWHM	Full width at half maximum
GC	Glassy carbon
GDL	Gas diffusion layer
HOR	Hydrogen oxidation reaction
HR-TEM	High resolution transmission electron microscopy
ICP-OES	Inductively coupled plasma optical emission spectroscopy
LSV	Linear sweep voltammetry
MCFCs	Molten carbonate fuel cells
MEA	Membrane electrode assembly
MW	Microwave heating
O-CNTs	Oxygen functionalized carbon nanotubes
ORR	Oxygen reduction reaction
PAFCs	Phosphoric acid fuel cells
PEM	Polymer electrolyte membrane or proton exchange membrane
PEMFCs	Polymer electrolyte membrane fuel cells or proton exchange membrane fuel cells
RDE	Rotating disk electrode
RHE	Reversible hydrogen electrode
RPM	Revolutions per minute

List of Abbreviations

RRDE	Rotating ring disk electrode
SOFCs	Solid oxide fuel cells
STEM	Scanning transmission electron microscopy
TEM	Transmission electron microscopy
TGA	Thermogravimetric analysis
UHV	Ultra-high vacuum
WE	Working electrode
XPS	X-ray photoelectron spectroscopy
XRD	X-ray diffraction

List of Symbols

\AA	Angstrom	
a_{alloy}	Lattice constant of PtCu alloy	\AA
a_{Cu}	Lattice constant of Cu	\AA
a_{Pt}	Lattice constant of Pt	\AA
at.	Atomic	%
B	Levich constant	
$B_{2\theta}$	Full wave half maximum	
C_{O_2}	Concentration of O_2 -dissolved in the electrolyte	mol L^{-1}
d	Interplanar distance	nm
D_{O_2}	Diffusion coefficient of oxygen	$\text{cm}^2 \text{s}^{-1}$
e^-	Electron	
E^0	Standard potential for half-cell reaction	V
ϵ_d	d-band center	
ϵ_f	Fermi level	
eV	Electron volt	
F	Faraday constant	C. mol^{-1}
h	Hour	
$H_{\text{ads/des}}$	Hydrogen adsorption desorption	
H_{upd}	Underpotential deposited hydrogen	
j	Overall current density	mA.cm^{-2}
j_d	Diffusion-limited current density	mA.cm^{-2}
j_k	Kinetic current density	mA.cm^{-2}
L_{Pt}	Pt loading in the electrode	mg_{Pt}
L	Crystallite size evaluated from XRD pattern	nm
n	Number of transferred electrons	
nm	Nanometer	
ω	Rotation speed	rpm
Q_{co}	Charge consumed during CO oxidation	mC
Q_{H}	Charge of the underpotential deposited hydrogen	mC
T	Temperature	$^{\circ}\text{C}$
V	Cell voltage	

List of Symbols

W	Watt	
θ	Diffraction angle	degree ($^{\circ}$)
λ	Wavelength	nm
ν	Kinematic viscosity	$\text{cm}^2 \text{s}^{-1}$

Abstract

English Version

Polymer electrolyte membrane fuel cells (PEMFCs) are a promising technology supplying electricity by converting the energy stored in chemical fuels into electrical energy with higher efficiency than combustion engines. Several challenges currently impede PEMFC commercialization such as limited membrane conductivity, low durability, high cost of the catalysts used on the anode and cathode side. However, the most critical challenge the PEMFC commercialization faces is the sluggish kinetics of the electrocatalytic oxygen reduction reaction (ORR) in acid electrolytes at monometallic catalyst surfaces including the commonly used Pt/C (Pt nanoparticles on a conducting carbon support) system. A comparably high platinum loading in the cathode would be needed which is however a challenge in terms of the cost. Moreover, Pt/C still exhibits large overpotentials for the ORR arising from the formation of stable Pt-O and Pt-OH species blocking the electrode surface. In order to resolve this issue efforts are ongoing to enhance the catalytic activity and stability of the noble metals through alloying them with a non-noble one. Core-shell nanoparticles have emerged as a novel class of catalysts with high activity for ORR, which exceeds that of Pt catalysts. The enhanced activity of the Pt-based core-shell alloys originates from the changes occurring in the electronic (ligand effect) and geometric (strain effect) structure of the Pt lattice, as a consequence the adsorption energies of the oxygenated intermediates are reduced yielding a higher number of active sites available for the ORR at lower overpotentials. Various approaches have been suggested to synthesize Pt-based metal core-shell catalysts. One approach of particular importance is the dealloying process which can be used to tailor the morphology and composition gradient of noble/non-noble metal alloy nanoparticles through selective dissolution of the non-noble components resulting in formation of a core-shell structure with a conformal noble metal shell and an alloy core. This dealloying process may be either achieved chemically through dispersing and stirring the alloy nanoparticles in an acid or electrochemically via potential cycling of an electrode containing the alloy catalyst in a way that the non-noble metal of the outer layers of the material will dissolve into the electrolyte. Following these techniques a set of PtCu/CNTs and Cu@Pt/CNTs alloy catalysts have been prepared by microwave-assisted polyol method with/without assistance of NaBH₄ in one-pot preparation step or in two steps respectively. In consequence the prepared catalysts were subjected to an annealing treatment at high

temperature ranging 400 °C to 1000 °C in reductive atmosphere (H₂/Ar) aiming to form the initial alloy metal structure. The core-shell structure was obtained through chemical or electrochemical dealloying of the prepared alloys in an acidic solution (aqueous perchloric acid, HClO₄). The influence of synthesis parameters such as: pH, stabilizer addition (Polyvinylpyrrolidon, PVP), alloying degree, the sodium borohydride (NaBH₄) molar ratio and conventional versus microwave heating were investigated and optimized. The catalysts were structurally characterized by X-ray diffraction (XRD), X-ray photoelectron spectroscopy (XPS), transmission electron microscopy (TEM) and inductively coupled plasma optical emission spectroscopy ICP-OES. It has been confirmed from structural characterization (XRD, XPS) that first an alloy structure between Pt and Cu has been formed which upon the dealloying step resulted in the formation of a core-shell structure or porous structure (confirmed by HR-TEM) depending on the particle size of the initial alloy catalysts that can be also controlled by the preparation method, preparation parameters and the dealloying protocol. Using the electrochemical methods; cyclic voltammetry (CV) and Linear Sweep Voltammetry (LSV) combined with Rotating Disk Electrode (RDE), the prepared catalysts have been tested towards ORR in acidic medium. Depending on the preparation process/parameters the most active catalysts with core-shell structure demonstrated up to 4.5 fold enhancement in the mass and specific activities compared to the benchmark commercial Pt/C (E-TEK).

German Version

Polymerelektrolytbrennstoffzellen (PEMFC) sind eine vielversprechende Technologie, um Elektrizität durch die direkte Umwandlung chemischer in elektrische Energie zu erhalten. Die Effizienz dieser Systeme ist höher als die von Wärme-Kraft-Maschinen. Allerdings erschweren derzeit verschiedene Herausforderungen die Vermarktung der PEMFCs, wie z.B. die limitierte Membranleitfähigkeit bzw. -beständigkeit oder auch die hohen Kosten für die an den Anoden und Kathoden verwendeten Katalysatoren. Das größte Problem für eine PEMFC-Kommerzialisierung stellt jedoch immer noch die träge Kinetik der elektrokatalytischen Sauerstoffreduktionsreaktion (ORR) im sauren Elektrolyten dar, die an monometallischen Katalysatoroberflächen wie dem vorrangig verwendeten Pt/C (Kohlenstoff-geträgerte Platinnanopartikel) ablaufen kann. Es ist allerdings eine vergleichsweise hohe Platinbeladung der Kathode notwendig, was erheblich zu den Kosten des Systems beiträgt. Darüber hinaus kommt es bei Pt/C durch die Ausbildung stabiler Pt-O- sowie Pt-OH-Spezies zu einer Blockade der Elektrodenoberfläche und somit zu hohen Überpotentialen bei der Reaktion. Deshalb zielt die derzeitige Forschung auf die Steigerung der elektrokatalytischen Aktivität und der Stabilität der Edelmetalle, z.B. durch Legieren mit unedlen Metallen, ab. Kern-Schale-Nanopartikel haben sich als neuartige Katalysatorklasse mit im Vergleich zu Platinkatalysatoren gesteigerter Aktivität für die ORR herausgebildet. Die erhöhte Aktivität der auf Platin basierenden Kern-Schale-Legierungen begründet sich in den Änderungen der elektronischen (Liganden-Effekt) und geometrischen (Formeffekt) Struktur des Platingitters. Daraus resultiert, dass die Adsorptionsenergie der bei der ORR auftretenden Intermediate reduziert und die Anzahl aktiver Oberflächenplätze erhöht wird. Zudem kann eine Verringerung des Überpotentials beobachtet werden. Diverse Herangehensweisen wurden vorgeschlagen um Platin-basierende Kern-Schale-Katalysatoren herzustellen. Ein Ansatz von besonderer Bedeutung ist der Entlegierungsprozess. Dieser kann benutzt werden um die Morphologie und das Mischungsverhältnis aus edlen und unedlen Metall in den Legierungspartikeln, durch selektives Auflösen der unedleren Metallkomponente, definiert einzustellen, infolgedessen es zur Bildung konformer Edelmetallschalen auf legierten Kernen kommt. Der Entlegierungsprozess kann einerseits chemisch durch Dispergieren und kontinuierliches Rühren der Legierungspartikel in Säuren vollzogen werden oder andererseits elektrochemisch durch dynamisches Zyklen eines auf einer Elektrode

aufgebrachten legierten Elektrokatalysators, in der Weise, dass das unedlere Metall in den äußeren Schalen in den Elektrolyten hinein aufgelöst wird. Auf diesen Techniken beruhend wurde in dieser Arbeit eine Reihe von legierten PtCu/CNTs- und Cu@Pt/CNTs-Elektrokatalysatoren durch die Mikrowellen-gestützte Polyol-Methode, mit und ohne Natriumborhydrid (NaBH_4), in einem einstufigen oder zweistufigen Herstellungsverfahren hergestellt. Im Anschluss wurden die präparierten Katalysatoren durch eine Hochtemperaturbehandlung ($400\text{ °C} - 1000\text{ °C}$) in reduzierender Atmosphäre (H_2/Ar) legiert, um die Ausgangsmetallegierung herzustellen. Die Kern-Schale-Struktur wurde durch chemisches oder elektrochemisches Entlegieren der hergestellten Legierungen in verdünnter Perchlorsäure erhalten. Der Einfluss verschiedener Syntheseparameter, wie z.B. pH-Wert, Zugabe von Stabilisatoren (Polyvinylpyrrolidon), Legierungsgrad, molares NaBH_4 -Verhältnis sowie konventionelles Erhitzen im Vergleich zum Mikrowellen-gestützten Erhitzen wurden untersucht und optimiert. Die Katalysatoren wurden strukturell durch Röntgenpulverdiffraktometrie (XRD), Röntgenphotoelektronen-spektroskopie (XPS), (hochauflösende) Transmissionselektronenspektroskopie (TEM) und optische Emissionsspektrometrie mittels induktiv gekoppelten Plasmas (ICP-OES) charakterisiert. Es konnte durch XRD und XPS nachgewiesen werden, dass zunächst eine PtCu-Legierung hergestellt werden konnte, welche durch den Delegierungsvorgang schließlich zur Ausbildung einer Kern-Schale-Struktur oder porösen Struktur führte. Abhängig war dies von der Partikelgröße der Ausgangslegierung, die durch Präparationsmethode und -parameter sowie den Entlegierungsvorgang eingestellt werden konnte. Mittels elektrochemischer Methoden wie der zyklischen Voltammetrie (ZV) und der Linear Sweep Voltammetrie (LSV) mit rotierenden Scheibenelektrode (RDE) in Perchlorsäure wurden die hergestellten Katalysatoren elektrochemisch charakterisiert und auf ihre Aktivität für die Sauerstoffreduktion untersucht. Dabei konnte beobachtet werden, dass, abhängig von der Präparationsmethode, die Kern-Schale-Katalysatoren eine bis zu 4,5-fach höhere spezifische und massenbezogene Aktivität im Vergleich zu kommerziellen Pt/C-Katalysatoren aufwiesen.

1 Introduction

1.1 Fuel Cells: Principle and Classification

Fuel cells are one of the oldest electrical energy conversion technologies. The invention date of the fuel cells back to the middle of the nineteenth century when Sir William Grove invented the first fuel cell in 1839 [1, 2]; however, fuel cells development in that period of time was abandoned because of the abundance of the natural energy resources. The tremendous increase in the world's population over the last few decades, combined with depletion of the natural energy resources, increasing energy demand, and increasing anxiety about the environmental consequence of fossil fuel use, reinvigorated the development of fuel cells anew. Renewable energy resources such as solar, wind, wave, and tidal energy can also be used to cover the energy demand; however, their irregular supply is considered as the main obstacle. At present, fuel cells have been widely considered as a promising alternative power generation technique because of their high energy conversion efficiency and diminished pollutant emissions.

A fuel cell is an electrochemical device that converts chemical energy into electricity, similar to the battery. The major difference between batteries and fuel cells is the way of introducing/storing the chemical reactants. Batteries store the chemical reactants that react together to produce electricity internally, and once consumed, the battery no longer produces power and must be discarded. However, some batteries are rechargeable using an external electricity/energy source. In contrast, fuel cells produce electricity through externally stored reactants, as long as the fuel and oxidant are supplied to the electrodes, electricity is produced (i.e. with fuel cells there is no limit to the amount of energy produced, assuming the electrodes are not damaged) [3]. There are different types of the fuel cells; each with its own unique chemistry, such as different operating temperatures, catalysts, electrolytes, reactants, oxidants and fuel. Commonly fuel cells are sorted by either the electrolytes used in the cell or by the operating temperature of, i.e. low- or high-temperature fuel cells [4, 6].

Low temperature fuel cells include

1. Alkaline fuel cell (AFC), AFC uses KOH or NaOH as electrolyte, OH^- is the species that migrates and reacts with fuels. An enormous range of electrocatalysts can be used in the AFC such as: non-noble metals, metal oxides, and noble metals.

2. Polymer electrolyte membrane fuel cell (PEMFC), also called proton exchange membrane fuel cell, utilizes proton exchange polymer membrane such as perfluorosulfonated acid membranes as the electrolyte (*the membrane is electrically non-conductive*); the migrating ion is H^+ . The state-of-art-catalyst used in the PEMFC is platinum supported on carbon (Pt/C).

3. Direct methanol fuel cell (DMFC), DMFC is a fuel cell type, exceptionally named according to the fuel used, H^+ is the migrating ion. DMFC usually uses the proton exchange membrane (PEM). Platinum is used as the electrocatalyst for both the anode and cathode side, however recently a mixture of platinum and ruthenium in equal proportions used in the anode side for a better performance. There is no advantage in using Pt-Ru bimetal catalyst in the cathode side.

4. Phosphoric acid fuel cell (PAFC), PAFC adopts phosphoric acid embedded in porous matrix made of chemically stable and electronic insulating material such as silicon carbide (SiC) as an electrolyte; H^+ is the migrating ion. The electrocatalyst used in the anode and the cathode side is platinum.

Usually low temperatures fuel cells are employed in vehicles and portable applications.

High temperature fuel cells include

1. Molten carbonate fuel cell (MCFC), MCFC has an electrolyte composed of molten lithium and potassium carbonates (Li_2CO_3 and K_2CO_3) mixture immobilized in a ceramic matrix, e.g. LiAlO_2 ; CO_3^{2-} is the migrating ion. Precious metal catalysts are not essential due to higher temperature (i.e higher activity) and the conditions involved.

2. Solid oxide fuel cell (SOFC), SOFC exploits solid, nonporous metal oxide usually yttria (Y_2O_3) stabilized zirconia (ZrO_2) as the electrolyte; O^{2-} is the migrating ion. High temperature fuel cells are usually employed in stationary power generation stations.

Figure 1.1 summarized the electrode reactions, namely; the anode and the cathode reaction, in the different types of fuel cells.

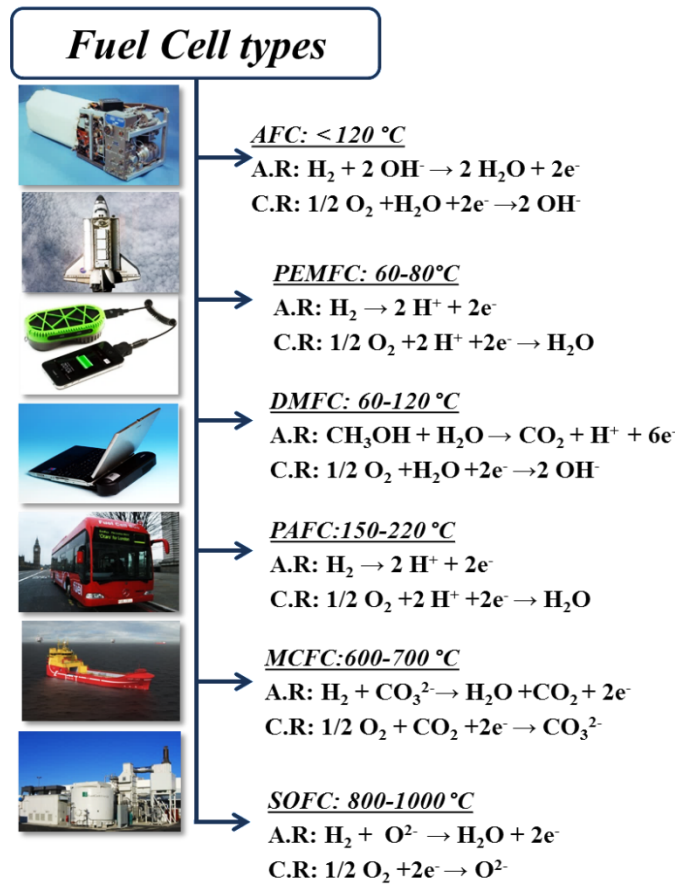


Figure 1.1: The major types of fuel cells and their electrodes reactions, where: **A.R** is the anodic reaction, and **C.R** is the cathodic reaction.

1.2 Polymer Electrolyte Membrane Fuel Cell (PEMFC)

Among the versatile types of low temperature fuel cells, the PEM fuel cell is considered a promising technology because of their high power density, high efficiency, fast start from room temperature, long lifetime, absence of a corrosive liquid electrolyte, etc. [7, 8]. The basic building block of the PEM fuel cell known is the membrane electrode assembly (MEA). The MEA encompasses: the anode gas diffusion layer (GDL) and anode catalyst, the cathode GDL and cathode catalyst, and the polymer membrane electrolyte layer separating them (the polymer membrane is impermeable to the gases and in the same time conducts protons), see Figure 1.2. However, the most important component is the anode/cathode catalyst layers, where the electrochemical reactions take place. Hydrogen is the common fuel because of its high reactivity, while

the common oxidant is oxygen, which is readily and economically available from air. The typical process is illustrated in Figure 1.2, the hydrogen is oxidized at the anode side to protons and electrons. The released electrons flow through an external circuit and are used for producing electrical power, whilst the protons pass across the electrolyte layer in the middle of the fuel cell. At the cathode side, the electrons and protons are recombined and reduce the oxygen molecules to complete the overall fuel cell reaction with only water as a by-product.

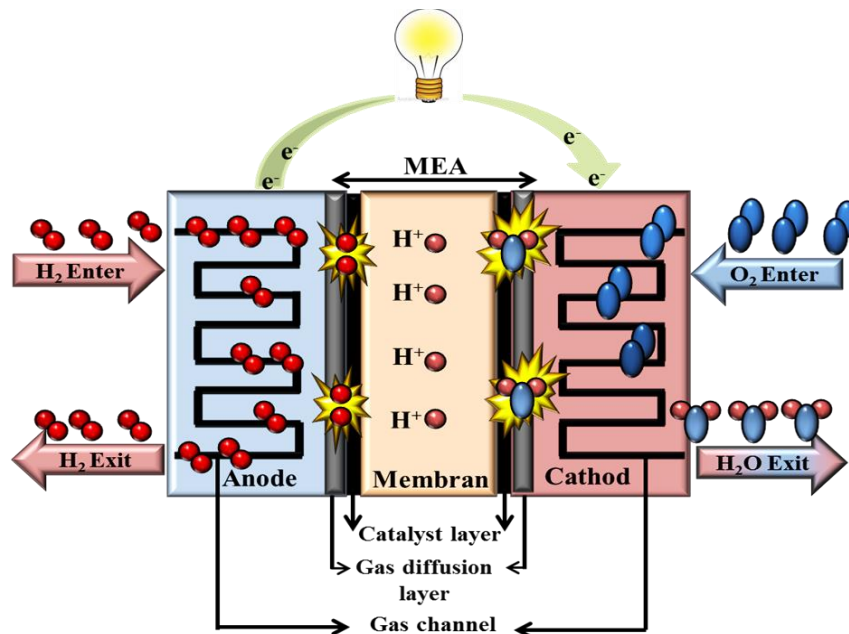


Figure 1.2: Schematic representation of single PEM fuel cell.

As mentioned before in section 1.1 platinum is considered as the best catalyst for both the hydrogen oxidation reaction (HOR) at the anode side and the oxygen reduction reaction (ORR) at the cathode, although there is a large difference between the two reactions. Hydrogen oxidation kinetics is relatively easy using the state-of-the-art Pt catalyst; however oxygen reduction kinetics is much slower [9]. The sluggish kinetics of the ORR is considered one of the major challenges hindering PEM fuel cell mass utilization because of the adverse impact on the overall performance of the fuel cell. Taking into consideration the economic perspective of using platinum as catalyst in fuel cells, i.e. the high production cost, because of the high cost and scarcity of natural resources of Pt [10, 5]. A general overview about the ORR mechanism, kinetics and electrocatalysts is presented in section 1.3.

1.3 Oxygen Reduction Reaction in the PEM Fuel Cell

The ORR mechanism is quite complicated and counts on many factors, among them the cathode electrocatalysts material and the electrolyte. The scope of this section will be: surveying some of the suggested ORR mechanisms on the-state of-art-Pt catalyst discussed in the earlier literatures from different point of view (*in acidic medium*), clarifying the reason behind the sluggish kinetics over Pt, and presenting appropriate solutions to overcome the ORR sluggish kinetics and the high production cost as well.

1.3.1 ORR Mechanism

The ORR mechanism in acid media on a catalyst surface is a multi-electron process consisting of a number of elementary steps involving different reaction intermediates. The first proposition of the possible pathways of the oxygen reduction mechanism has been reported by Damjanovic et al. [11] using the rotating ring disk electrode (RRDE) technique. RRDE is a valuable tool used in the quantitative determination of ORR intermediate. Since then, numerous schemes have been published concerning the ORR mechanism and the intermediates involved [12-15], for example, and not as a limitation: the uncomplicated scheme proposed by Wroblowa et al. [16], so far considered the most efficacious scheme to describe the oxygen reduction pathways, see Figure 1.3. As it can be seen from Figure 1.3 the ORR in acidic solutions occurs by two plausible mechanisms: the first mechanism is a direct reduction path, which reduces the oxygen to water through a 4-electron transfer whilst the second mechanism is a series 2-electron reaction path where the oxygen molecule is first reduced to hydrogen peroxide, which could be a final by-product, followed by reduction of hydrogen peroxide to water.

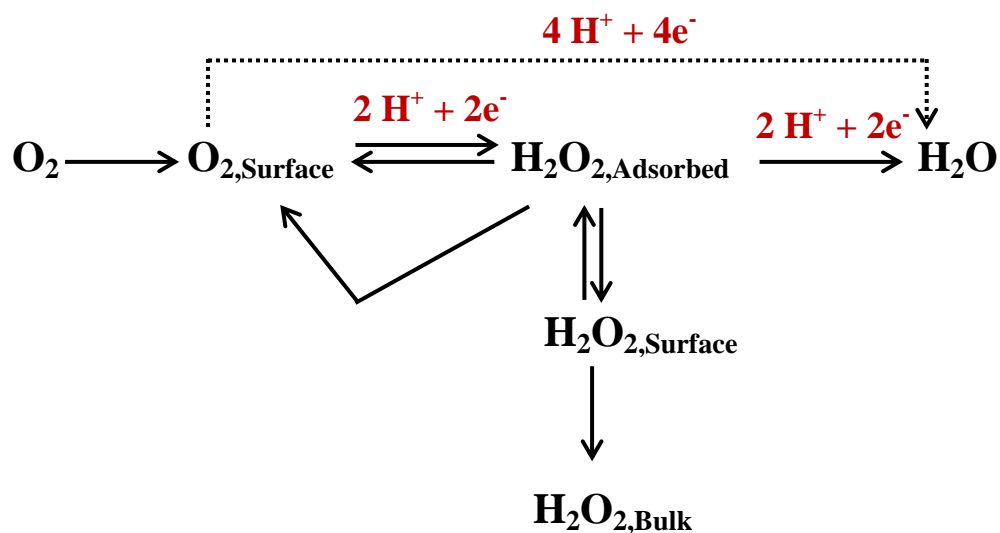


Figure 1.3: Oxygen reduction reaction pathways in acidic solution (redrawn after [16]).

Another point of view on the model of oxygen adsorption on the catalysts surface has been raised by Yeager [17]. Yeager argued that the ORR pathway and the by-products are dictated by the type of interaction between the catalyst surface and the oxygen. Three types of interactions; namely the Griffiths model (i.e. side-on), Pauling model (i.e. end-on), and bridge model, and two reduction reaction pathways (direct and indirect) were proposed as illustrated in Figure 1.4. Yeager [17] claimed that the Griffiths and the bridge interactions proceed through the direct pathway with water as a final product, the direct 4-electron reduction requires dissociation of oxygen before transferring the first electron [18]; both Griffiths and bridge-type interactions weaken the O–O bond leading to bond cleavage. On the other hand, the Pauling model interaction was suggested to proceed through indirect pathway yielding hydrogen peroxide as a final product; reduction of oxygen beyond peroxide state could occur in case of rupture of the O–O bond.

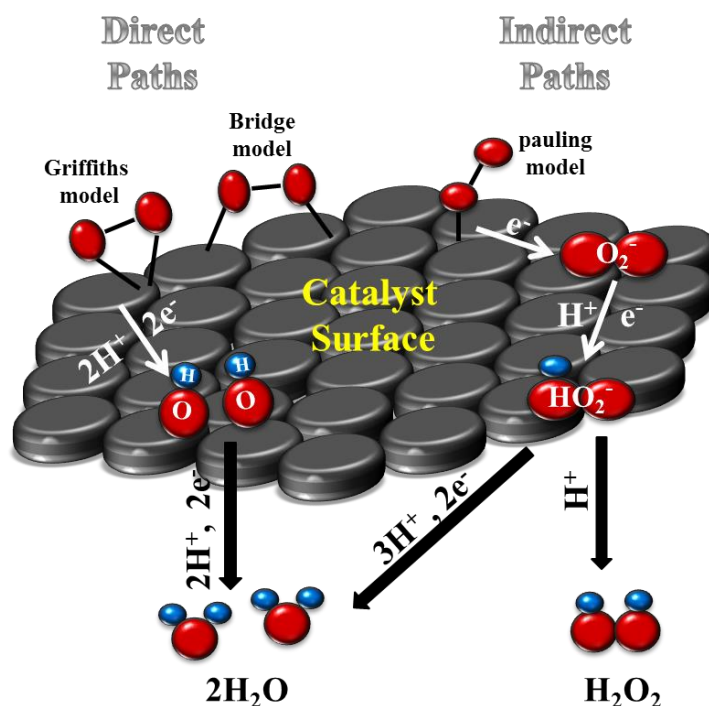
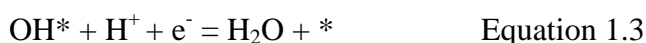


Figure 1.4. Oxygen reduction reaction pathways on the catalyst surface depending on the oxygen interaction types (modified after [19]).

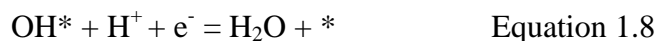
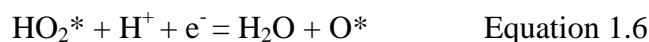
Norskov and coworkers [20] also investigated the ORR mechanism using density functional theory (DFT), to gain some insight into the cathode reaction mechanism. They elucidate that there is a correlation between the ORR pathway and the electrode potential. They proposed two possible mechanisms: the dissociative mechanism at low current density (Equations 1.1-1.3) and the associative mechanism at high current density (Equations 1.4-1.8). However, contributions from both mechanisms in the ORR may occur depending on the metal and the electrode potential.

Dissociative mechanism



Associative mechanism





Where * denotes a site on the catalyst surface. Both mechanisms do not exhibit peroxide formation, however the possibility of peroxide formation in the associative mechanism exist since molecular oxygen is present and the O–O bond may not be broken resulting in H₂O₂ formation which could be further reduced to H₂O or be a final product.

1.3.2 ORR Kinetics on Pt: The Origin of Sluggish ORR

The thermodynamic potential of ORR is 1.23 V vs. SHE (SHE is the hydrogen scale at standard conditions). At such a high potential neither Pt nor any other electrode materials could stay pure consequently, the ORR electrode materials undergoes oxidation which alters their surface properties (Equation 1.9 shows the oxidation reaction of Pt [10, 21]).



Thus, in the presence of oxygen the Pt surface is a mixture of Pt and PtO at potential higher than 0.8 V while, at lower potentials the Pt surface is pure Pt (i.e. ORR kinetics on Pt is not the same in different potential ranges). Wang et al. [22] reported that the ORR kinetics is slower on an oxidized Pt surface than on a pure Pt surface at a given potential. They claimed that the surface oxygen species such as surface hydroxide or oxide are poisoning species rather than intermediates, and the reaction rate is controlled by un-poisoned sites. According to the classic catalytic volcano plot, i.e. relationship between the oxygen reduction activity of metals and the binding energy, the maximum reaction rate can be achieved when the surface adsorbed oxygen species are strongly bound to the surface to weaken or break the O–O bonds, but in the same time are weakly bound to the surface after electron transfer to allow desorption for product formation [20]. Pt alloys were found to be able to enhance the catalytic activity of the

ORR through shifting the onset potential of adsorbed oxidized species above 0.8 V vs. RHE, depending on the alloying elements [23].

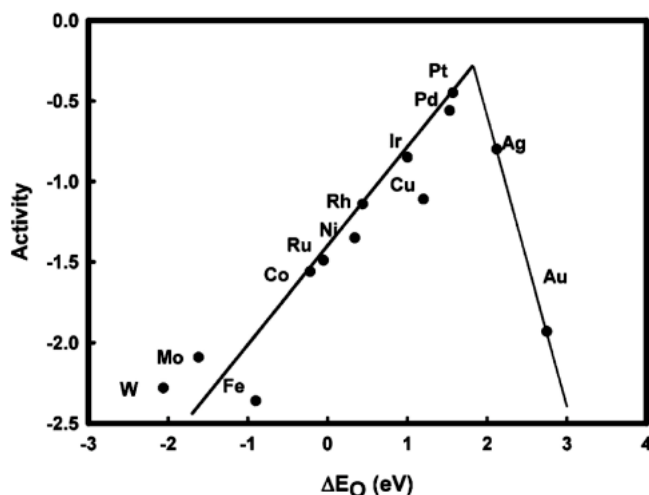


Figure 1.5: Trends in oxygen reduction activity plotted as a function of the oxygen binding energy [20].

1.3.3 Pt-Based Alloy Electrocatalysts for ORR

Various strategies have been put forward in recent years concerning fuel cell electrocatalysis and particularly the ORR electrocatalysts because the ORR kinetics are much slower than the anodic HOR kinetics and the fuel cell voltage drop is mainly due to the ORR overpotential. Overcoming the oxygen reduction reaction kinetic limitations and at the same time reducing the amount of Pt catalyst in the fuel cell stack requires a breakthrough in electrocatalysis development.

According to Hammer et al. the reactivity of any metal can be changed significantly by: (i) changing the surface structure, (ii) alloying, or (iii) introducing additional adsorbates onto the surface. They reported that the reactivity of transition metals towards a certain adsorbate (i.e. adsorption energy) varies with the position of the d-band center relative to the Fermi level. Hammer and co-worker used the d-band center shift as a descriptor to indicate the variation in the electronic structure and binding energies of surface adsorbates and reactive intermediates on metal surfaces, and to explain the changes in the catalytic reactivity [24]. Briefly, the variation in the reactivity of transition metals towards a certain adsorbate is controlled by the shape, antibonding versus bonding orbital occupancy and the position of the d-band center.

Alloying of Pt with non-precious metals such as 3d-transition metals is considered to be a promising approach to improve the ORR kinetics and reduce the financial burden of the fuel cell electrocatalysts [25-28]. Pt-based alloy electrocatalysts achieve at least double the mass activities than a pure Pt catalyst while reducing the Pt content and therefore the total cost of the cells component [29]. The enhanced activity of the Pt-based alloys originates from the changes occurring in the electronic and geometric structure of the Pt lattice, i.e. alloying Pt induces changes in the d-bands width, *for details see below*. Consequently the adsorption energies of the oxygenated intermediates are reduced yielding a higher number of active sites available for the ORR at lower overpotentials [25, 30-32].

Electronic or Ligand effect

According to Hammer et al. the electronic structure of the metals may be changed by alloying [24]. The d-electrons in less noble metal such as Cu, Co, Ni, and Fe tend to transfer to the noblest one such as Pt causing down shifts in the d-band center of the latter due to the upshift of the Fermi level [33], as illustrated in Figure 1.6. Accordingly, the bond strength of the adsorbed species and thereby their reactivity will be changed.

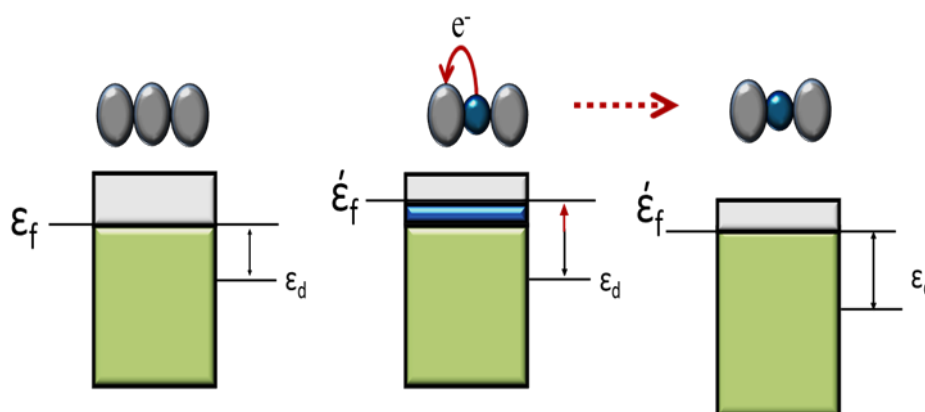


Figure 1.6: Schematic representation of the ligand effect in bimetallic catalyst, where: ϵ_d and ϵ_f referring to the d-band center and Fermi level respectively (modified after [34]).

Geometrical or Strain effect

Ruban et al. [35] studied the effect of alloying metals on the d-band center. They reported that the shift of the d-band depend on the difference in the size of the metals. For example, when Pt is modified with a second metal with a larger lattice constant; the Pt lattice is exposed to tensile strain (i.e. narrower d-band and an up-shift in the d-band center) as shown in the left side of Figure 1.7. In contrast, if the Pt is modified with another metal that has a smaller lattice constant, the d-band becomes broader and the d-band center shifts down, see the right side in Figure 1.7. Jalan et al. [36] revealed that decreasing the Pt-Pt interatomic distance enhances the ORR activity. They proposed that inducing contraction in the Pt lattice (i.e. decreasing the Pt-Pt bond distance) provides more favorable sites for the dissociative adsorption of oxygen while those with lattice expansion are less active.

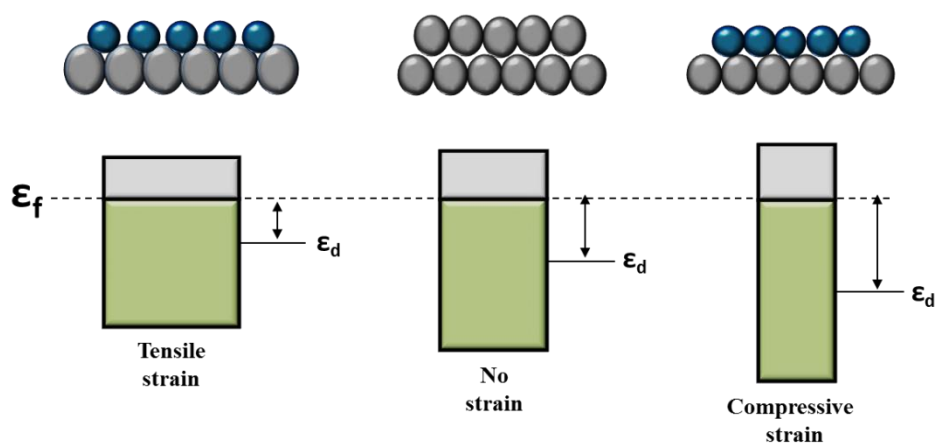


Figure 1.7: Schematic representation of the strain effect in bimetallic catalyst, where: ϵ_d and ϵ_f referring to the d-band center and Fermi level respectively (modified after [34]).

1.3.4 Core/Shell Nanoparticles

The improvement of catalysts for the direct oxygen reduction reaction path ($4 e^-$) remains a critical challenge for fuel cells and other electrochemical energy technologies. Over the past decade attention focused on the development of metal alloys with nanostructured compositional gradients such as the core-shell structures which exhibit higher activity than supported Pt and Pt-based alloy nanoparticles [37-41]. Core-shell structure electrocatalysts as illustrated in Figure 1.8 are composed of an alloy or pure 3d-metal core enveloped by a pure noble-metal-shell.

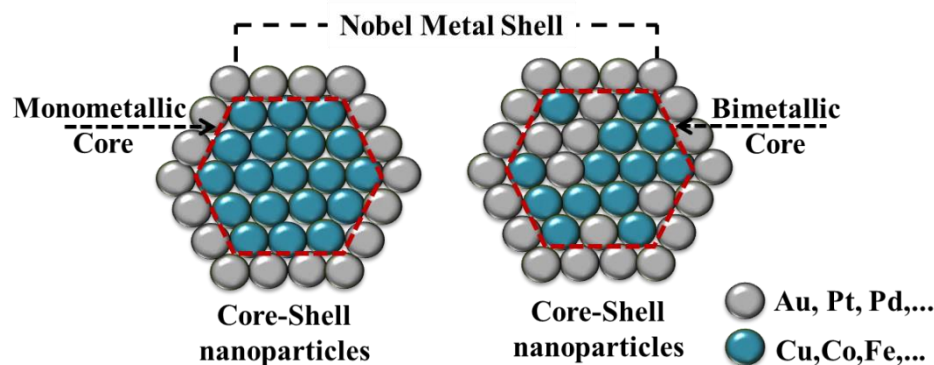


Figure 1.8: Core-Shell structure.

Core-shell nanoparticles can be synthesised through two general approaches: top-down approach and bottom-up approach. The top-down approach employs externally controlled tools, either traditional workshop or microfabrication methods to cut, mill, and shape materials into the desired shape and order [42-48]. In contrast, bottom-up approaches use the chemical properties of the molecules to cause them to self-organize or self-assemble into some useful conformation [49-51]. However, bottom-up approaches have more eminent advantages over the top-down methods such as the ability to produce much smaller sized particles, the absolute accuracy, complete process control, and economically effective.

Versatile and fabulous chemical synthesis approaches have been developed for bimetallic core-shell nanocatalyst synthesis. For example, carbon supported AuNi, PdCo and PtCo core shell alloys were prepared by Zhang et al. [52] via surface segregation of the noble metals at elevated temperature. Lee et al. [53] prepared Pt rich Pt₃Au/C alloys using adsorbate induced surface segregation where the catalyst powder was heat treated at 200 °C for 10 h under a CO atmosphere. Pd rich Pd_xCo/C alloy nanoparticles were prepared using the same approach. This approach is based on the higher adsorption enthalpy of CO on the noble metal than on non-noble metals [54]. Additionally the redox exchange of underpotentially deposited Cu by e.g. Pt [55], and the direct electrodeposition of a noble metal around a pre-formed metal-core can be used [56, 57]. Among all these approaches one route of particular importance is the dealloying route. Dealloying is a facile synthesis route used to tailor the morphology and composition gradient of noble/non-noble metal alloy nanoparticles through

selective dissolution of the less-noble components to form dealloyed bimetallic core-shell nanoparticles [58].

1.3.5 Dealloyed Pt-based Bimetallic Electrocatalysts for ORR

Dealloyed Pt bimetallic ORR electrocatalysts were discovered totally by coincidence in 2005 by Strasser and coworkers as a result of equipment malfunction during the preparation of Pt-Cu bimetallic alloy catalysts [59, 60]. Dealloying is a common corrosion process during which an alloy is parted by the selective dissolution of the most electrochemically active species [61]. This destructive process causes restructuring inside the bulk of the alloy leading to either a three-dimensional nanoporous alloy or core-shell structure surface enriched with the nobler (unreactive) alloy components, depending on the size scale for the alloy structure [62]. The dealloying process could be achieved either chemically through dispersing and stirring the alloy nanoparticles in a corrosive medium [26, 63, 64] or electrochemically via potential cycling of an electrode containing the alloyed electrocatalyst in a way that the less-noble metal of the outer layers of the material will dissolve into the electrolyte solution [37, 65]. The origin of the improved ORR activity is mainly due to the lattice strain in the noble-metal-rich shell, which weakens the chemisorption energies of adsorbed oxygen intermediates.

The question which should be asked is *‘what actually happens during the dealloying process?’* A model has been developed by Erlebacher et al. [66] to simulate the dealloying process of a silver-gold alloy, the selective dissolution of silver from the Ag-Au alloy was achieved by immersing the Ag-Au alloy in nitric acid; the dealloying conditions were optimized to dissolve the silver atoms and kept the gold atoms intact. They propose that the whole process starts with the dissolution of a single silver atom from the flat alloy surface with face centered cubic (111) orientation, leaving behind a surface terrace vacancy. The atoms coordinating this vacancy have less lateral neighbours than other silver atoms in the terrace and thus are more liable to dissolution. With time, the entire terrace is stripped leaving behind gold atoms with no lateral coordination (ad-atoms), these gold ad-atoms diffused and start to agglomerate into islands. Thereby, the alloy surface involves two distinct regions, first the pure gold clusters region that locally passivate the surface, and the un-dealloyed region exposed to the electrolyte. As the selective dissolution proceeds gold clusters are mounds that are

gold-rich at their peaks and that have alloy composition at their bases, this rough surface is referred to in the literature as a “*skeleton*” nanostructure [30, 38, 67]

M-Skin and M-monolayer nanostructures are other terminologies that exist in the literature (where M is a noble metal such as Pt, Au, etc.). The M-skin nanostructure could form either by thermally induced surface segregation or by adsorbate induced surface segregation. The former is achieved through annealing the bimetallic alloy at elevated temperature, however the later by heat treatment of the alloy nanoparticles in gases such as CO, NO, H₂ and O₂, where the noblest metal in the alloy tends to segregate on the surface [53, 54]. On the other hand, M-monolayer nanostructures are formed by electrodeposition of a noble metal around a pre-formed pure metal or alloy core via redox exchange of underpotentially deposited metal, e.g. replacement of Cu by Pt [55].

1.4 Aim of the Work

ORR on the Pt electrode surface is one of the most extensively studied electrochemical reaction mechanisms since it is a very slow, complex reaction and industrially important. It was shown that the key to the sluggish ORR kinetics is the strong adsorption of the oxygenated species such as O and OH on the Pt surface. Alloying platinum with non-precious metals such as 3d-transition metals is considered as a promising approach to improve the ORR kinetics and reduce the financial burden of the fuel cell electrocatalysts. In this thesis, we aim to synthesis a set of PtCu catalysts supported on oxygen-functionalized carbon nanotubes for enhancement the ORR using the microwave-assisted polyol synthesis for the first time. CNTs as a support were used owing to their unique mechanical and electrical properties compared with carbon black in addition to providing better dispersion and distribution of the catalysts nanoparticles. The influence of synthesis parameters such as pH, stabilizer addition (Polyvinylpyrrolidone, PVP), alloying temperature, sodium borohydride (NaBH_4) as a co-reductant and conventional versus microwave heating was investigated and optimized to obtain catalytically active core-shell catalysts for the ORR. The PtCu core-shell structure was obtained either by electrochemical or chemical dealloying of the PtCu alloys (Cu-rich surface) in acidic medium. The dealloying process allows the selective dissolution of the surface metal constituents with less-noble character (i.e. Cu) leaving behind a Pt-enriched surface alternatively. The results demonstrated that the catalytic efficiency of the dealloyed catalysts influenced by the morphology, particle size, composition, and dealloying procedure of the PtCu alloy nanoparticles, however, the dealloyed catalysts consider promising materials for ORR in terms of their mass and specific activity when compared with the benchmark Pt/C catalyst.

2 Experimental Work

2.1 Materials

Name	Specification	Supplier
Multi walled carbon nanotubes	Baytubes C 150P	Bayer Material Science AG
Alummina Suspension	1 μm and 0.3 μm	LECO Corporation, Germany
Ethanol, $\text{C}_2\text{H}_6\text{O}$	$\geq 99\%$ HPLC grade	Carl Roth, Germany
Ethanol absolute, $\text{C}_2\text{H}_6\text{O}$	99.9 % HPLC grade	Chemsolute, Germany
Ethylene Glycol, $\text{C}_2\text{H}_6\text{O}_2$	$\geq 99\%$ for synthesis	Carl Roth, Germany
2-Propanol, $\text{C}_3\text{H}_8\text{O}$	$\geq 99.98\%$ LC-MS grade	Carl Roth, Germany
Perchloric acid, HClO_4	70%	Carl Roth
Nitric Acid, HNO_3	$\geq 65\%$ p.a. ISO	Carl Roth, Germany
Polyvinylpyrrolidone, $(\text{C}_6\text{H}_9\text{NO})_x$	M. Wt. = 10000	Sigma Aldrich
Sodium Hydroxide, NaOH	$\geq 99\%$ p.a. ISO, Pellets	Carl Roth, Germany
Sodium Borohydride, NaBH_4	99 %	Acros organics, USA
Nafion 117 solution	5% in mixture of lower aliphatic alcohol and water	Sigma-Aldrich, USA
Hexachloroplatinic acid hexahydrate, $\text{H}_2\text{PtCl}_6 \cdot 6\text{H}_2\text{O}$	M. Wt. = 409.82 g, 99.9%	Acros organics, USA
Pt/C	20 Wt.% Pt on carbon vulcan XC-72	E-TEK, USA
copper sulfate pentahydrate $\text{CuSO}_4 \cdot 5\text{H}_2\text{O}$	M. Wt. = 285.82 g, 99.995%	Sigma-Aldrich, USA
Ar gas		Air Liquid, Germany
N_2 gas	99.999%	Air Liquid, Germany
CO gas	10 % in He	Air Liquid, Germany
H_2 gas	99.999%	Air Liquid, Germany
Glassy Carbon rode	Sigradur ® G	HTW, Germany

2.2 Methods

2.2.1 Microwave-Assisted Polyol Synthesis of PtCu/CNTs Catalysts

2.2.1.1 Oxidative Treatment of MWCNTs

The as-received MWCNTs were first heat treated at 800 °C for one hour under argon flow to remove any volatile compounds. To create anchoring sites for enhanced metal impregnation on the more or less inert nanotubes, it is a common approach to introduce defects into the surface by strong oxidants. These oxidants attack the graphitic structure by electrophilic reaction and generate active sites such as –OH, –COOH, and C=O. Here, 1 g heat treated MWCNTs were refluxed in 200 ml of 5 M HNO₃ for 6 h at 100 °C, then the reaction mixture was diluted with 400 ml deionized water and stirred overnight. The functionalized MWCNTs were washed several times with deionized water till the pH of the filtrate is close to 7 and collected by centrifugation (centrifuge 4807, Eppendorf) for 20 min at 5000 rpm. Finally the nanotubes were dried overnight at 110 °C. Thus the oxygen functionalized CNTs (O-CNTs) were used as supports for the electrocatalysts [65].

2.2.1.2 Catalyst preparation

PtCu alloy nanoparticles with nominal Pt:Cu ratio of 20:80 at.% supported on O-CNTs were synthesized via microwave-assisted polyol reduction. Cu and Pt precursor solutions were prepared by dissolving appropriate amounts of copper sulfate pentahydrate (CuSO₄·5H₂O) and hexachloroplatinic acid hexahydrate (H₂PtCl₆·6H₂O) in ethylene glycol (EG) respectively. 300 mg of O-CNTs were dispersed in 80 ml EG for 30 min, afterward 10 ml H₂PtCl₆/EG (0.0285 M) followed by 40 ml CuSO₄/EG (0.0285 M) were added dropwise to the O-CNTs suspension to obtain a metal loading of 30 Wt.% (13 Wt.% Pt and 17 Wt.% Cu). 276.25 mg Polyvinylpyrrolidone (PVP, molecular weight 10000) dissolved in 20 ml EG were added dropwise to the suspension which amounts to a molar ratio between PVP and metals of 5:1 (related to PVP monomer units). Catalysts prepared in this way are labelled PtCu/PVP and the pH of the preparation solution was 2.5. Since the pH has a strong influence on the polyol synthesis, additional catalysts were prepared in solutions with adjusted pH. For this purpose, 1 M NaOH dissolved in EG was added dropwise to the suspension until the desired pH was reached. Catalysts prepared in the same way as above but at pH 8 and

11, respectively, are labelled PtCu/PVP_{pH=8} and PtCu/PVP_{pH=11}. Furthermore, for comparison one sample was prepared in the same way as above but without PVP (“PtCu”; pH 5.7).

In any case the suspension was left under continuous stirring for 3 h followed by ultra-sonication for 30 min to aid homogeneous metal impregnation onto the O-CNTs. The reaction mixture was then heated by pulsed microwave (MW) irradiation in a START 1500 Microwave reactor (Milestone Srl, Figure 2.1), operated at 700 W for 10 min (150 s on followed by 60 s off) under reflux conditions and stirring. After MW heating, the suspension was left to cool down to room temperature and kept stirring overnight before it was separated by centrifugation at 5000 rpm for 20 min. The collected precipitate was washed thoroughly with deionized water and dried at 100 °C overnight. Finally, all catalysts were annealed for 6 h at 600 °C (10 °C min⁻¹ heating rate) in a continuous flow of 5% H₂/Ar. In order to evaluate the influence of annealing temperature on catalyst structure and activity, the freshly prepared samples PtCu/PVP were also reduced at 400 or 500 °C and the reduction temperature is added to the catalyst name in this case (e.g., PtCu/PVP₄₀₀). After cooling, air was very slowly bled into the tube before removing the sample to prevent rapid air oxidation of the catalysts [68].



Figure 2.1: START 1500 Microwave reactor.

2.2.2 PtCu/CNTs Electrocatalysts Synthesised by NaBH₄-Assisted Polyol-Reduction

2.2.2.1 Catalyst Preparation

Synthesis of a 30% Pt₂₀Cu₈₀/CNTs precursor involves the impregnation of Pt and Cu salts from solution on a weighed amount of O-CNTs dispersed in ethylene glycol, where PVP was used to control and stop the growth of metal particles and inhibit agglomeration. The detailed procedure has been reported in section 2.2.1.2. Metal impregnation is followed by reduction of the metal salts first by dropwise addition of freshly prepared 0.5 M NaBH₄/EG (molar ratio of NaBH₄:metal= 10 and 50) under vigorous stirring. After stirring for 3 h at room temperature and sonication for half an hour, the reaction mixture was heated up for 10 min using microwave pulsed irradiation under reflux and stirring conditions (700 W, 150 s on followed by 60 s off). The reaction mixture was subsequently cooled down to room temperature and the PtCu/CNTs catalysts were separated by centrifugation (5000 rpm, 20 min), washed several times with deionized water, dried overnight at 100 °C and crushed to a very fine powder. Finally, the as-prepared PtCu/CNTs catalysts were alloyed by annealing at 600 °C for 6 h under 10% H₂/Ar atmosphere. The catalysts prepared were labelled as “PtCu_{XSM}” where X is the molar ratio of NaBH₄: metal and the abbreviations S and M indicate the order of reduction steps (S= sodium borohydride, M = microwave irradiation). The abbreviation C is used for polyol reduction under conventional heating in an oil bath for 8 h at 170 °C instead of MW. A catalyst from ETEK (Pt/C, 20% Pt on Vulcan XC72) was used for comparison [65].

2.2.3 Synthesis of the Chemically Dealloyed PtCu/CNTs Catalysts

2.2.3.1 Catalyst Preparation

The PtCu/CNTs alloy precursor was prepared according to the earlier procedure described in section 2.2.1.2, particularly the as-prepared PtCu_{50SM} catalyst. Succinctly, 117 mg H₂PtCl₆, 286 mg CuSO₄ and 111 mg PVP (molar ratio PVP:metal= 5, Pt:Cu ratio 1:4) were dissolved in appropriate amounts of EG and dropwisely added to 300 mg of O-CNTs well dispersed in EG. The reaction mixture was stirred for 3 h at ambient temperature before adding 0.5 M NaBH₄/EG (molar ratio NaBH₄:metal= 50) to reduce the metal precursors. Thereafter, the temperature of the reaction mixture was raised up for 10 min by pulsed microwave irradiation under reflux and stirring conditions (700 W, 150 sec on and 60 sec off). This two-step reduction turned out to be necessary to fully reduce both Cu and Pt precursors. The prepared catalysts were collected by centrifugation, washed 4-5 times with deionized water and dried overnight at 100 °C before annealing at 600 °C for 6 h under reductive atmosphere (10 % H₂, 90% Ar). For the chemical dealloying, 100 mg of PtCu/CNTs alloy precursor were dispersed in 40 ml 1 M HClO₄ under stirring for 15 min, 1 h, 2 h, 4 h, and 6 h, respectively, at room temperature. Afterwards the acid solution was decanted and the dealloyed catalysts were washed several times with deionized water and separated by centrifugation for 10 min each at 5000 rpm. The resulting material was dried overnight at 100 °C and labelled as PtCu_x, where x refers to the dealloying time.

2.2.4 Cu@Pt/CNTs Catalysts Synthesis

2.2.4.1 Catalyst Preparation

A Cu@Pt/CNTs catalyst (Pt:Cu atomic ratio of 1:4) was prepared through two consecutive preparation steps, involving firstly the preparation of Pt/CNTs by polyol reduction followed by impregnation of the Pt/CNTs with a copper precursor. Subsequently the catalyst was subjected to a thermal decomposition step as schematically illustrated in Figure 2.2. In detail, for preparation of Pt/CNTs, 300 mg from the O-CNTs were homogeneously dispersed by magnetic stirring for 30 min in 80 ml ethylene glycol (EG) which acts as a solvent and reducing agent (heating up ethylene glycol solution generates acetaldehyde [69] or glycolaldehyde [70] as a major product which in turn act as a reductant). Thereafter, 10 ml 0.02297 M H_2PtCl_6 /EG solution was added dropwise to the O-CNTs/EG mixture followed by addition of 20 ml PVP/EG solution (PVP, $M = 10000$) with a metal to PVP ratio of 1:5 (based on the unit monomer of PVP). The reaction mixture was left under continuous stirring for 3 h followed by sonication for 30 min before being subjected to a microwave irradiation at 700 W in a pulsed mode with t_{on} 150 s and t_{off} 60 s with total irradiation time of 10 min. Afterward the reaction mixture was kept under overnight stirring. Subsequently 100 ml absolute ethanol was added to the reaction mixture to sediment the particles, the reaction mixture stood for 1 h before washing. The Pt/CNTs catalyst was washed several times with water and dried overnight at 100 °C. The Pt content in a typical synthesis should amount to 13 wt. % of nominal metal loading; however, the actual measured loading established from the TGA analysis was ca. 10.5 wt. %, which was expected based on our earlier results in chapter 3&4. The as-prepared Pt/CNTs catalyst was heat treated in a horizontal tube furnace at 185 °C under open-air atmosphere for 5 h to remove any remaining PVP traces and to spur its catalytic activity [71, 72]; this catalyst is labelled as Pt/CNTs_HT. For the second impregnation step, 200 mg Pt/CNTs_HT was dispersed in 80 ml absolute ethanol for 30 min before dropwise addition of 20 ml 0.02157 M $CuSO_4$ /EtOH solution followed by stirring at room temperature overnight. Thereafter, the catalyst suspension was kept at 40 °C in a water bath until thick black slurry was obtained, then the catalyst slurry was overnight dried in an oven at 60 °C and grounded in a mortar. To obtain the final Cu@Pt/CNTs catalyst, an alloying step was carried out as follows: first, heat treatment of the catalyst under flowing of H_2 /Ar stream (10% H_2) with a heating rate of 10 °C/min for 2 h at 250 °C to thermally decompose the copper

precursor, followed by annealing the catalyst for 6 h at elevated temperatures of 600, 800, and 1000 °C in the same atmosphere. The alloyed catalysts were cooled down to room temperature by natural convection in Ar atmosphere to avoid carbon burning and labelled as Cu@Pt_x, where x: refers to the annealing temperature. For formation of a core-shell structure, the annealed catalyst in a form of thin layer electrode was subjected to an electrochemical dealloying step under voltammetric dissolution conditions by potential cycling the electrode in acid electrolyte solution (0.1 M HClO₄) for specific cycles at higher scan rate (200 potential cycle at scan rate of 200 mV/s). These electrochemical stress conditions allow the selective dissolution of the surface metal constituents with less-noble character (Cu surface), leaving behind a Pt enriched surface. Alternatively, the dealloying process has been carried out chemically in acid solution for a specific time to distinguish the two methods of dealloying and their effect on the catalysts activity towards ORR. Cu@Pt₁₀₀₀ catalyst was selected for this differentiation, due to its higher alloying degree in comparison with the catalysts annealed at lower temperatures (i.e. 600 °C and 800 °C; see results in section 6.3). More details about the dealloying processes will be given in the electrochemical measurements part and through the discussion part in chapter 6.

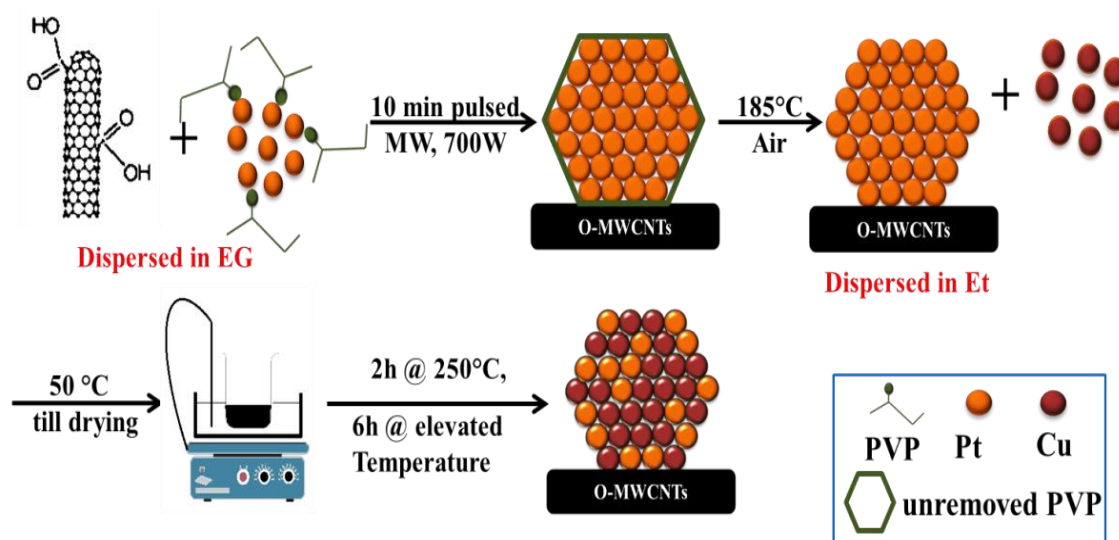


Figure 2.2: Schematic illustration for Cu@Pt_x catalysts preparation.

2.3 Electrocatalyst Characterization

2.3.1 Structural Characterization

2.3.1.1 X-Ray Diffraction (XRD)

The crystalline structure of the alloyed and dealloyed catalysts was examined by X-ray diffraction (Bruker AXS D8 diffractometer) with $\text{CuK}\alpha$ ($\lambda = 0.15406$ nm) radiation in the 2θ range of $5-80^\circ$ at a scan rate of 2° min^{-1} . The stoichiometric ratio of the alloyed catalysts was determined using Vegard's rule (Equation 2.1). The mean crystallite size was determined according to Scherrer's equation (Equations 2.2) while the interplaner distance was evaluated from (Equation 2.3). The lattice parameter of the alloyed nanoparticles was determined from (Equation 2.4).

$$a_{\text{alloy}} = x a_{\text{Pt}} + (1 - x) a_{\text{Cu}} \quad \text{Equation 2.1}$$

$$L = \frac{0.9 \lambda}{B_{2\theta} \cos \theta_{\text{max}}} \quad \text{Equation 2.2}$$

$$d = \frac{\lambda}{2 \sin \theta_{\text{max}}} \quad \text{Equation 2.3}$$

$$a = \frac{\sqrt{h^2 + k^2 + l^2}}{2 \sin \theta_{\text{max}}} \lambda \quad \text{Equation 2.4}$$

Here, a is the lattice parameter in \AA , L is the crystallite size in nm, d is the interplaner distance in nm, λ is the wavelength (0.15406 nm), $B_{2\theta}$ is the full width at half maximum (FWHM) in radians, θ_{max} is the 2θ angle at the peak maximum, (hkl) is the miller indices, x is the fraction of Pt atoms ($0 \leq x \leq 1$, x defines the fraction, not the wt. %). The platinum lattice constant is $a_{\text{Pt}} = 3.9242$ \AA while for copper it is $a_{\text{Cu}} = 3.6148$ \AA [73].

2.3.1.2 X-Ray Photoelectron Spectroscopy (XPS)

XPS measurements were carried out in an ultra-high vacuum (UHV) set-up equipped with a monochromatic Al $\text{K}\alpha$ X-ray source (1486.6 eV; anode operating at 14 kV and 30 mA) and a high resolution Gamdata-Scienta SES 2002 analyzer. The binding energies were calibrated basing on the graphite C 1s peak at 284.5 eV. Data reduction and treatment was performed using CasaXPS software.

2.3.1.3 Transmission Electron Microscopy (TEM)

TEM images were recorded on a LEO 912, Japan, operating at an acceleration voltage of 120 keV. Sample preparation involved sonicating the catalyst powder in ethanol for at least one hour and then deposition of a few drops from the suspension onto a carbon film supported by a copper grid. The evaluation of TEM images was performed with the Lince242e software. The particle size distributions for the catalysts were obtained by manually analyzing nearly 200 particles from the micrographs and the mean particle size diameter (d) was calculated by the following formula (Equation 2.5):

$$d = \sum_i n_i d_i / \sum_i n_i \quad \text{Equation 2.5}$$

Where n_i is the number of particles with diameter d_i (i = integernumber).

2.3.1.4 Thermogravimetric Analysis (TGA)

The total metal loadings of the catalysts were detected by thermogravimetric analysis (NETZSCH, STA 449 F1, Jupiter) with a heating rate of 10 °C min⁻¹ under O₂/Ar up to a temperature of 1000 °C. Under these conditions the carbon is completely oxidized, allowing for the determination of the metal loading.

2.3.1.5 Inductively Coupled Plasma-Optical Emission Spectroscopy (ICP-OES)

ICP-OES performed with a ULTIMA 2, HORIBA JOBIN YVON, was utilized to determine bulk catalysts composition, after they were being digested in aqua regia under microwave digestion.

2.3.2 Electrochemical Characterization

2.3.2.1 Working Electrode Preparation

Prior to electrode preparation, a glassy carbon rotating disk electrode (GC, Ø 4 mm, 0.125 cm², embedded in teflon, Figure 2.3A) was first polished with a polishing cloth using 1 and 0.3 µm alumina slurry respectively followed by washing with 1:1 (v/v) ethanol/water mixture and water respectively in an ultrasonic bath, each for 15 min. In order to prepare the catalyst ink, 2.5 mg catalyst was mixed with 350 ml of a mixture of 2-propanol, and a small amount of nafion solution (35 ml, 5 wt. %). After sonicating at room temperature in an ultrasonic bath for 1 h, the ink was stirred for 3 h at 1500 rpm. Afterward, 10 ml from the ink was deposited onto the glassy carbon disk via a micropipette. The films were allowed to dry under ambient temperature in a 2-

propanol saturated atmosphere, Figure 2.3B. The electrode preparation is a critical issue regarding the experimental error respectively reproducibility of the electrochemical experiments. The above described preparation route is a result of an optimization process in electrode preparation resulting in an experimental error below 20%. This error likely results from slightly inhomogeneous electrode coverage and slight differences in catalyst loading.

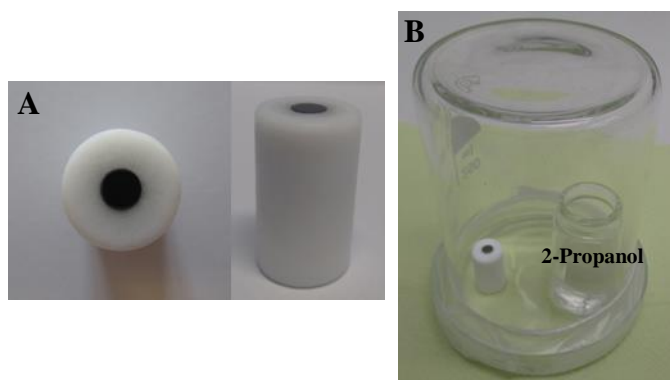


Figure 2.3: A) GC rotating disk electrode, and B) casted GC electrode storage system.

2.3.2.2 Electrochemical Setup

The electrochemical measurements were performed using an Autolab potentiostat/galvanostat (PGSTAT128N, Metrohm) controlled by the NOVA 1.8 software. A rotator EDI 101 with CTV101 speed control unit (Radiometer analytical) was used for the rotating disk electrode (RDE) setup, see Figure 2.4. A one compartment glass cell (three-electrode cell) was used for the electrochemical measurements (Figure 2.5). In this configuration the potential of the working electrode (WE) was monitored relative to a reference potential (RHE, reversible hydrogen electrode). The tip of the reference electrode should be placed as close as possible to the working electrode in order to minimize solution resistance, for the counter electrode (CE) a piece of Pt net with surface area much larger than that of the working electrode was used. The purpose of a larger counter electrode surface area is to accelerate the electrochemical reaction occurring on it, so it doesn't impede the reaction occurring on the working electrode [74]. The electrolyte used was 0.1 M HClO_4 (prepared by diluting 70% HClO_4 , with deionized water). All measurements were conducted at room

temperature. The electrochemical dealloying protocol of the as-prepared alloy catalysts to obtain the core-shell structure will be described later in details in each chapter.



Figure 2.4: Electrochemical set-up used for the electrochemical measurements.

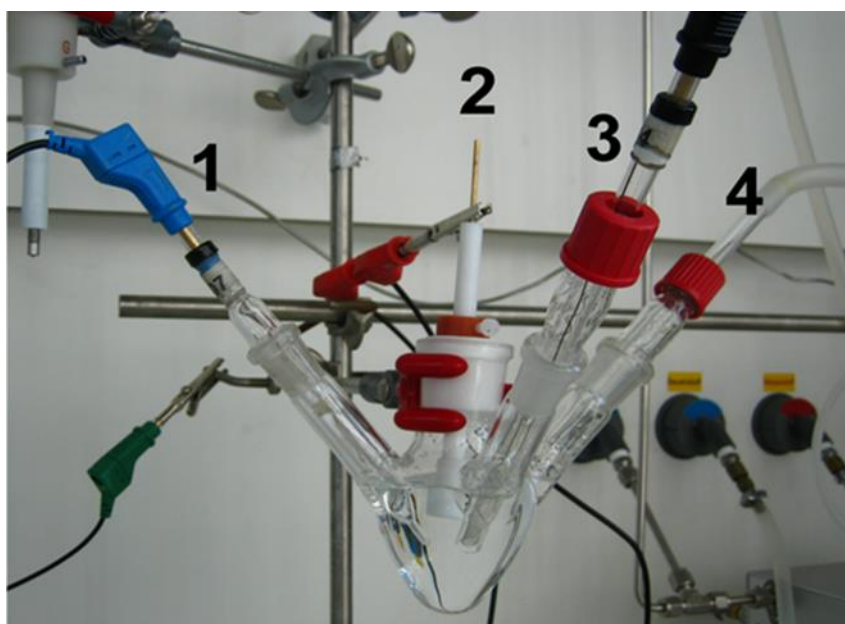


Figure 2.5: One compartment three-electrode electrochemical cell, 1) Reversible hydrogen electrode (RHE), 2) working electrode, 3) counter electrode, 4) gas inlet.

2.3.2.3 Linear Sweep Voltammetry (LSV)

Regarding the electrochemical characterization of the ORR activity, LSV measurements were conducted using the RDE technique. LSV were achieved by sweeping the potential of the working electrode positively from 0.05 to 1.1 V vs. RHE in oxygen saturated 0.1 M HClO₄ with a sweep rate of 5 mV s⁻¹ and rotation speed of 900 rpm as illustrated in Figure 2.6. For the Koutecky-Levich plot (j^{-1} vs. $\omega^{-1/2}$) the rotation speed was varied in the range between 400-1600 rpm. As shown in the Figure 2.6 the ORR LSV exhibits three distinctive potential regimes, the plateau region between 0.05-0.65 V vs. RHE characteristic to the diffusion-limited regime, the mixed (kinetic and diffusion) regime, thereafter the kinetic regime. The mass and the specific activities were evaluated at 0.9 and 0.85 V vs. RHE.

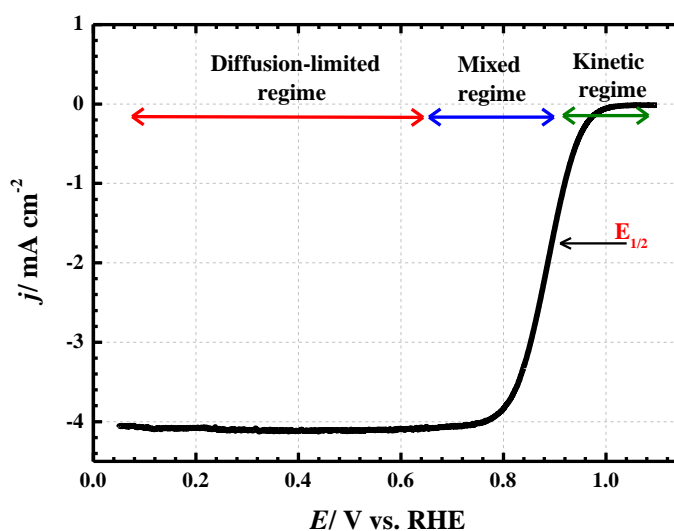


Figure 2.6: Linear voltammograms of the oxygen reduction measured on Pt/C catalyst at an electrode rotation speed of 900 rpm, sweep rate of 5 mV s⁻¹ in O₂-saturated 0.1 M HClO₄ electrolyte.

2.3.2.4 Electrochemical Active Surface Area (ECSA) Determination

2.3.2.4.1 Carbon Monoxide (CO) Stripping

The oxidation of adsorbed CO was used to determine the electrochemically active surface area (ECSA) of the electrocatalysts assuming that CO adsorbs onto the surface of Pt to form a monolayer. The 0.1 M HClO₄ electrolyte solution was purged with CO for 20 min to allow for complete adsorption of CO onto the catalyst. Afterwards excess CO in the electrolyte was purged out with N₂ for 20 min holding the potential at 0.05 V. Thereafter, three CV were recorded at a scan rate 20 mV s⁻¹ between 0.05 and 1.1 V vs. RHE, see Figure 2.7. During the first sweep, electrochemical oxidation of adsorbed CO to CO₂ [$CO + H_2O = CO_2 + 2 H^+ + 2 e^-$] [75] occurs, while the other two cycles were carried out to ensure that all adsorbed CO was removed from the catalyst surface and to monitor the baseline.

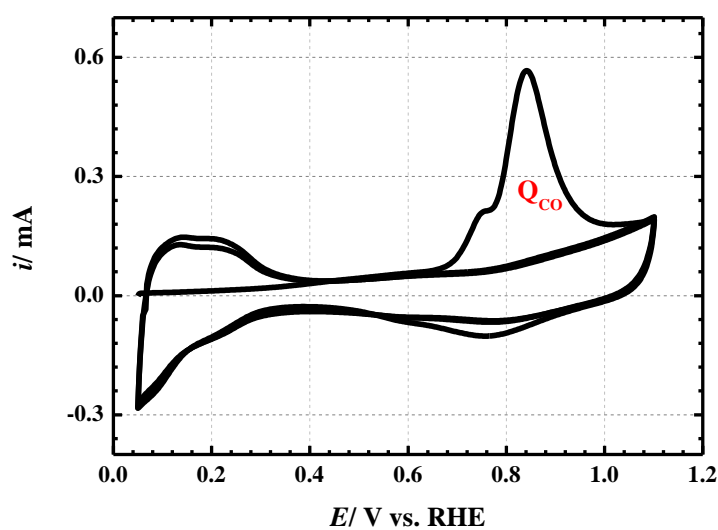


Figure 2.7: CO stripping voltammogram of Pt/C catalyst conducted in N₂-purged 0.1M HClO₄ at a sweep rate of 20 mV s⁻¹.

The ECSA of the catalysts was estimated from the CO stripping charge corrected for double layer capacitance, Equation 2.6, by assuming that one CO molecule occupies one Pt atom surface site in a linear adsorption configuration.

$$ECSA = \frac{Q_{CO} [mC]}{0.420 [mC.cm^{-2}] * L_{Pt} [mg]} \quad \text{Equation 2.6}$$

Here Q_{CO} is the charge under the CO stripping peak in coulomb which is related to the reaction: $Pt-CO + H_2O \rightarrow Pt + CO_2 + 2e^- + 2H^+$, L_{Pt} is the Pt loading on the electrode and the value 0.420 in $mC\ cm^{-2}$ represent the charge density required to oxidized a monolayer of CO on a Pt surface [76].

2.3.2.4.2 Hydrogen underPotential Deposition (H_{upd})

The ECSA of the electrocatalysts was also evaluated from Equation 2.7 using the normalized charge of the underpotential deposited hydrogen stripping using the cyclic voltammogram scan performed after the electrochemical dealloying cycles, Figure 2.8.

$$ECSA = \frac{Q_H [mC]}{0.210[mC.cm^{-2}] * Pt\ loading[mg]} \quad \text{Equation 2.7}$$

Q_H is the measured charge, and $0.210\ mC\ cm^{-2}$ is the theoretical value of a one electron transfer assuming one H atom per Pt atom [77-78]

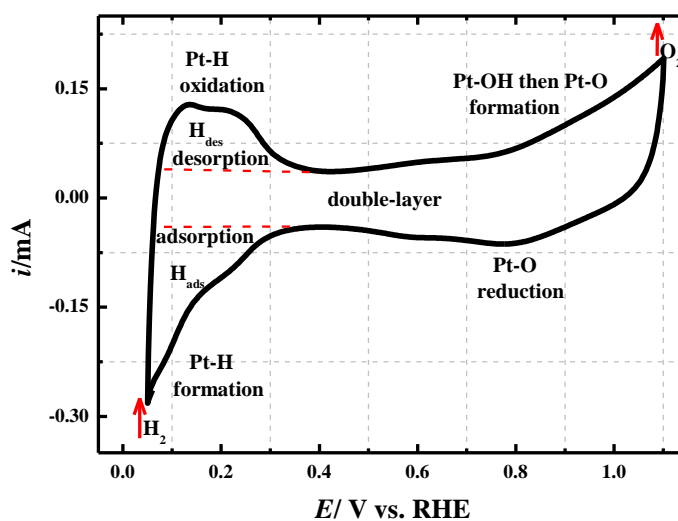


Figure 2.8: Cyclic voltammogram of Pt/C catalyst conducted in N_2 -purged $0.1\ M\ HClO_4$ and with sweep rate of $100\ mV\ s^{-1}$.

3 Microwave-Assisted Polyol Synthesis of PtCu/Carbon Nanotube Catalysts for Electrocatalytic Oxygen Reduction

Reprinted from ref. [68] with permission of Elsevier, copyright© 2015.

3.1 Introduction

Different techniques could be used for core-shell nanoparticles preparation, see section 1.3.4; however dispersion and reduction of the metal salt to its metallic form are the fundamental steps. Polyol process is a promising chemical reduction method for the preparation of nano-scaled particles, and it was described for the first time by F. Fievet et al. as a novel route for the preparation of finely divided metal powders [79, 81]. In the polyol process, the metal precursor is dispersed in a liquid polyol such as the commonly used ethylene glycol (EG). EG has a dual function: it acts as a solvent and as a reducing agent at the same time. EG upon heating decomposes and generates species that reduce the metallic ions to metal particles [79, 82]. Usually conventional heating with its inherent heterogeneous temperature distribution is used to thermally activate the polyol, but in recent years microwave (MW) dielectric heating is quickly emerging as a widely accepted new processing technology for a variety of inorganic and organic syntheses [83-85]. The main advantages, besides the acceleration in the reduction rate, are the high homogeneity in the distribution and the nanoparticles size [82, 86-88].

In conventional thermal processing, thermal energy is delivered to the surface of the reaction vessel and is transferred to the bulk of the material via conduction and convection. In contrast, the microwave irradiation is delivered directly into the bulk of the reaction mixture through molecular interaction with the electromagnetic field (i.e. electromagnetic energy converted to thermal energy), and the interaction of microwaves with the solvent is related to its dielectric constant and dielectric loss. This difference in the way of energy delivery results in many potential advantages when using microwaves in materials processing. The main advantages of microwave assisted reactions are i) increasing the reaction kinetics, ii) formation of new phases, and iii) energy saving [89, 90].

Irrespective of the mode of heating, one important aspect in the polyol process is the ability to keep the nanoparticles physically isolated from each other to prevent

agglomeration. This isolation process is commonly accomplished by using a suitable capping agent such as polyvinylpyrrolidone (PVP).

Synthesising PtCu alloy particles with high degree of alloying, small particle size and high activity for the ORR remains a challenge. Under this regards, in this chapter, the microwave-assisted polyol method is used for the synthesis of PtCu alloy catalysts supported on functionalized carbon nanotubes (see section 2.2.1). Compared to reported synthesis procedures, considerably low annealing temperatures of 400-600 °C were used to obtain alloyed catalysts, leading to very small alloy particle sizes. The influence of different synthesis parameters such as the addition of PVP and the pH value on the structure of the synthesised catalysts and their activity towards ORR are evaluated. The dealloying process for preparation of the prospective active catalyst (core-shell) is carried out electrochemically in acid solution.

3.2 Electrochemical Measurements Protocol

Cyclic voltammetry (CV) was carried out in N₂-purged electrolyte (30 min) under N₂ atmosphere in a potential range between 0.05 V and 1.2 V vs. RHE. The dealloying process started with three CVs recorded at a low scan rate (100 mV s⁻¹) in order to monitor the early stages of Cu dissolution. Afterward, the electrocatalysts were subjected to 1600 fast CVs at a scan rate 1000 mV s⁻¹ in the same potential range, followed again by three slow CVs at 100 mV s⁻¹, in order to detect the changes that occurred in the electrocatalysts surface during the fast scans. The platinum electrochemical surface area (Pt-ECSA) of the catalyst was determined by CO stripping measurements as described in section 2.3.2.4.1. Oxygen reduction activity was determined with the RDE using linear sweep voltammetry (LSV) conducted in 0.1 M HClO₄ saturated with O₂ gas for 30 min and under O₂ atmosphere. All RDE measurements were carried out by sweeping the potential from 0.05 V to 1.1 V vs. RHE at scan rate of 5 mV s⁻¹, using three different rotation speeds: 400, 900 and 1600 rpm. The Faradic current density (i.e. the current caused by oxygen reduction) was obtained by subtracting the capacitive current (measured in N₂-saturated 0.1 M HClO₄) from the one measured in the O₂ saturated solution. Mass and surface specific activities were established at 850 mV vs. RHE and 900 mV vs. RHE and corrected for mass transport limitation.

3.3 Results and Discussion

3.3.1 Metal Loading and Catalyst Composition

The metal loadings determined by both TGA and ICP-OES as well the molar Pt:Cu ratio obtained from ICP-OES for each catalyst are presented in Table 3.1 together with the molar ratio calculated from XRD data (Vegard's law Equation 2.1). Loadings are calculated assuming that PVP was completely removed during heat treatment. The calculated molar ratio and the measured one are quite the same and the metal loadings determined from both the TGA and ICP-OES analysis are nearly the same. However, the total metal loading is much lower than the expected one of 30%. It has been reported [91] that PVP as stabilizer may impede nanoparticle deposition onto the support. On the other hand, also for the catalyst sample prepared by without PVP (PtCu), the metal loading is quite low. A more detailed view however indicates, that the nominal Pt loading is nearly reached (>11 wt. % measured, 13 wt. % nominal), while the Cu loading in neither case reaches the expected 17 wt. %. Considering the reduction potentials, it is well known that at least in aqueous solutions Pt ions should be more easily reduced than Cu ($\text{Cu}=\text{Cu}^{+2}:0.345\text{ V vs. SHE}$; $\text{Pt}=\text{PtCl}_6^{-2}:0.726\text{ V vs. SHE}$). Furthermore redox exchange may occur in a way that PtCl_6^{-2} oxidizes already reduced Cu to Cu ions while it is reduced to Pt. Obviously only parts of the Cu ions are finally reduced to Cu during these complex redox equilibria. A higher pH leads to a decrease in the Pt loading and an increase in the Cu loading. The latter is not attributed to Cu ion reduction but to Cu hydroxides precipitation (see below). A lower Pt loading at higher pH using polyol reduction has been also reported by others [92, 93] It was suggested that during polyol reduction negatively charged particles form due to the stabilization of the nanoparticles with e.g. glyconate ions. Since the CNTs used by us are oxidized, i.e. they contain carboxylic groups at their surface, which de-protonate at higher pH, they are negatively charged as well, weakening the interaction with the nanoparticles during catalyst preparation. Similarly in previous investigations on PtNi catalysts, a reduced Pt loading at higher pH was found [87, 94]. In chapter 4 we aim to enhancing the Cu loading with keeping high Pt loading by introducing a second reduction step.

Table 3.1: Pt-Cu alloy atomic ratios and the Wt.% measured by TGA and ICP-OES.

Catalyst	Pt:Cu _{XRD}	Pt:Cu _{ICP}	Total Wt.% _{TGA}	Wt.% _{ICP}		
				Pt	Cu	Total
PtCu/PVP ₆₀₀	Pt ₇₂ Cu ₂₈	Pt ₆₇ Cu ₃₃	14.88	11.76	2.08	13.84
PtCu/PVP ₅₀₀	Pt ₈₆ Cu ₁₄	Pt ₆₃ Cu ₃₇	13.38	11.23	2.21	13.44
PtCu/PVP ₄₀₀	Pt ₈₃ Cu ₁₇	Pt ₆₃ Cu ₃₇	13.87	11.33	2.2	13.53
PtCu/PVP _{pH=11}	Pt ₂₅ Cu ₇₅	Pt ₃₅ Cu ₆₅	16.73	4.86	8.91	13.77
PtCu/PVP _{pH=8}	Pt ₁₆ Cu ₈₄	Pt ₃₅ Cu ₆₅	3.74	0.976	1.77	2.74
PtCu	Pt ₅₆ Cu ₄₄	Pt ₅₁ Cu ₄₈	16.91	11.55	3.58	15.13

3.3.2 TEM and XRD Characterization

Figure 3.1 shows TEM images of the catalysts of this study. Spherical, uniform and well dispersed metal nanoparticles on the surface of the O-CNTs are visible in the catalysts prepared with addition of PVP and annealed at different temperatures (400-600 °C), Figure 3.1A-C. The heat treatment has no effect on the dispersion of the nanoparticles while it has a small effect on the particle size Table 3.2. On the other hand, the catalysts prepared at higher pH in presence of PVP (PtCu/ PVP_{pH=11}) and the one prepared without modification of the solution pH and without PVP (PtCu) show a high extent of agglomeration (Figure 3.1D-F) and it was difficult to calculate the mean particle size because of this agglomeration. It is obvious that the PVP and the pH play an important role in the dispersion of the catalyst nanoparticles on the supporting material.

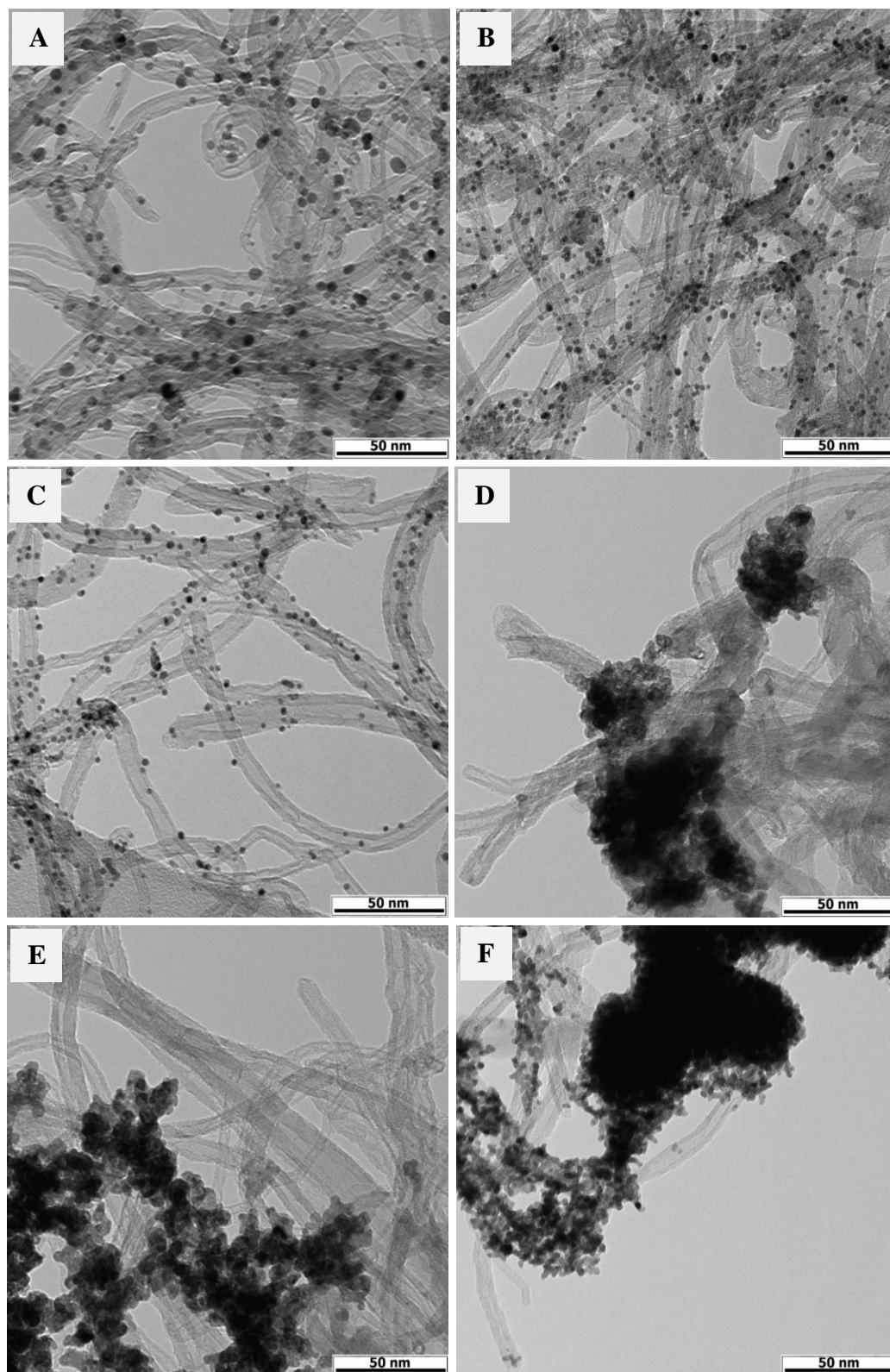


Figure 3.1: TEM image of the prepared catalysts A) PtCu/PVP₆₀₀, B) PtCu/PVP₅₀₀, C) PtCu/PVP₄₀₀, D) PtCu/PVP_{pH=11}, E) PtCu/PVP_{pH=8}, F) PtCu.

Figure 3.2 illustrates the X-ray diffraction patterns of the synthesised PtCu catalysts. The peak at a diffraction angle of ca. 26° is related to the 002 plane of the supporting CNTs material. Furthermore, all catalysts display three main diffraction peaks of the 111, 200 and 220 lattice planes [95, 96] which are located at scattering angles higher than 39.9° , 46.5° and 67.8° of pure Pt (green solid lines) and lower than 44° , 51° and 74° of pure Cu (red dash lines), indicating alloy formation between Pt and Cu. However, the composition of the catalysts and thus the peak position is different for all samples, as will be discussed below. The peaks marked with the red triangles or green asterisks are corresponding to $\text{Cu}(\text{OH})_2$ [97, 98] and Cu_2O [89, 99] respectively. These peaks are observed in the samples prepared where the pH has been adjusted to higher values with sodium hydroxide. Thus they are likely due to the precipitation of copper species and not to their polyol reduction, explaining the higher Cu contents of these samples as displayed in Table 3.1. Figure 3.3 shows the diffractograms of catalysts prepared with PVP and alloyed at different annealing temperatures. It is intriguing that already after an annealing at temperatures as low as 400°C an alloy can be observed. This indicates that after catalyst preparation via microwave the Pt and Cu species already are in an intimate contact. It is, however, important to note at this instance that no alloy formation was observed in the as prepared, non-heat treated catalyst.

The changes in the lattice constant of the prepared PtCu alloy nanoparticles at the 111 peak were calculated via (Equation 2.4) while the crystallite size at the same peak was calculated using the Debye-Scherrer equation (Equation 2.2). The alloying extent and therefore the atomic ratio of Pt:Cu were calculated using Vegard's law (Equation 2.1). The results are summarized in Table 3.2 while the Pt:Cu atomic ratio has already been displayed in Table 3.1.

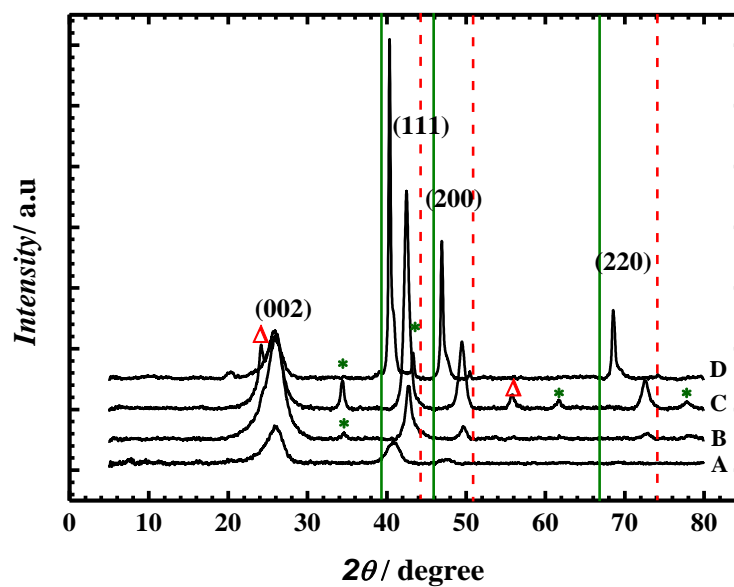


Figure 3.2: XRD diffractograms of, **A)** PtCu/PVP₆₀₀, **B)** PtCu/PVP_{pH=8}, **C)** PtCu/PVP_{pH=11}, **D)** PtCu.

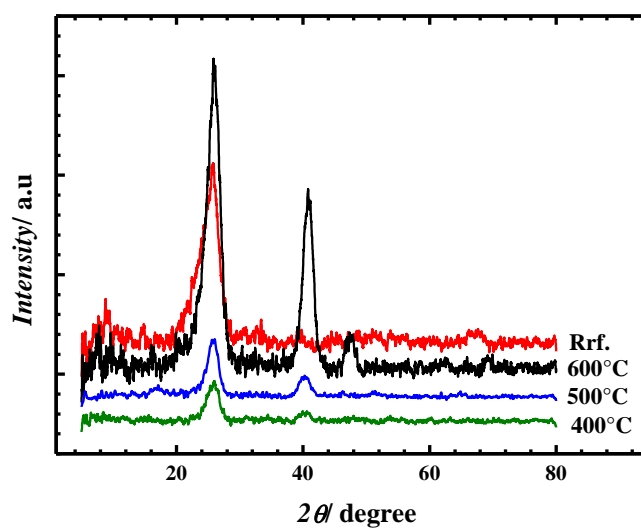


Figure 3.3: XRD patterns of the sample PtCu/PVP alloyed at different temperatures; Ref. refers to the as-prepared PtCu/PVP catalyst.

Table 3.2: Structural parameters evaluated from the XRD and TEM analysis.

Catalyst	$a_{\text{alloy}}/\text{\AA}$	$2\theta_{111}$	FWHM	Crystallite size/nm ^[a]	Particle size/nm ^[b]
PtCu/PVP ₆₀₀	3.8366	40.7	1.9375	4.6	3.7
PtCu/PVP ₅₀₀	3.8823	40.2	1.9776	4.3	2.7
PtCu/PVP ₄₀₀	3.8730	40.3	1.9436	4.3	2.5
PtCu/PVP _{pH=11}	3.6931	42.4	0.8085	10.5	-
PtCu/PVP _{pH=8}	3.6647	42.7	1.0776	7.9	-
PtCu	3.7870	40.3	0.3304	25.9	-

[a]established from XRD, [b] established from TEM

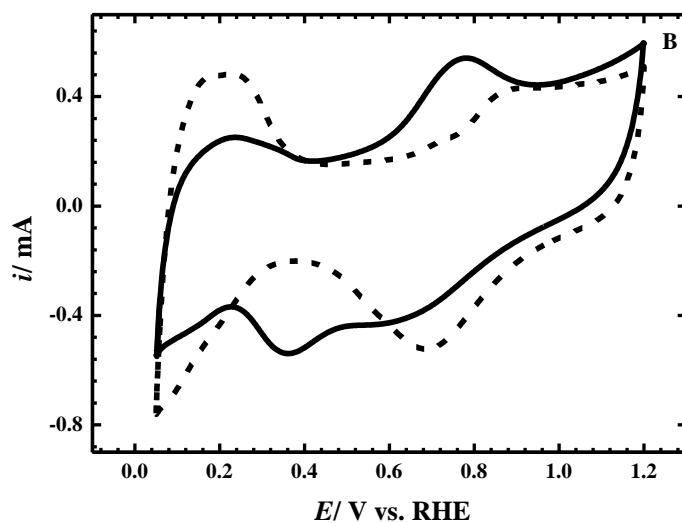
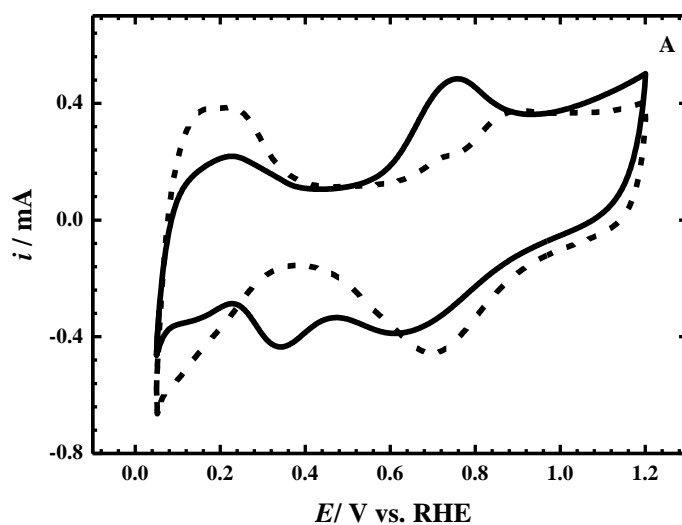
As already expected from visual inspection of Figure 3.2 and as documented in Table 3.1, depending on the preparation conditions Pt-Cu alloys with different Pt:Cu ratios are synthesised.

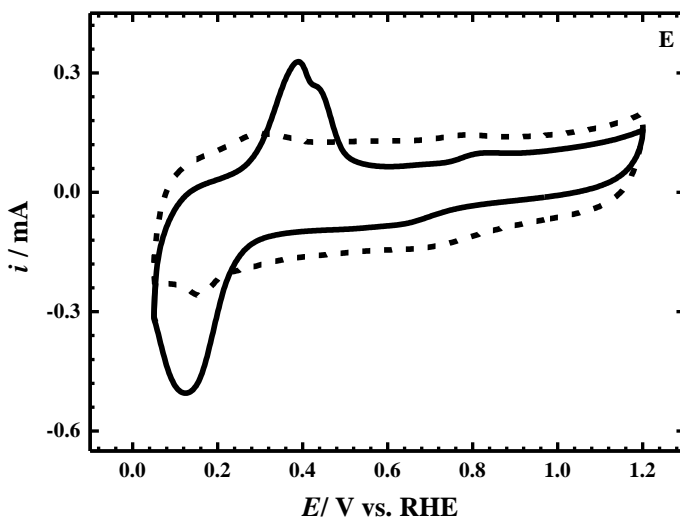
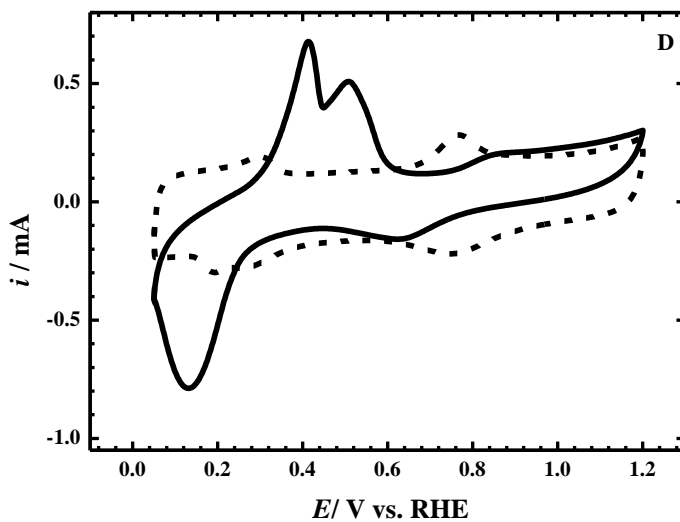
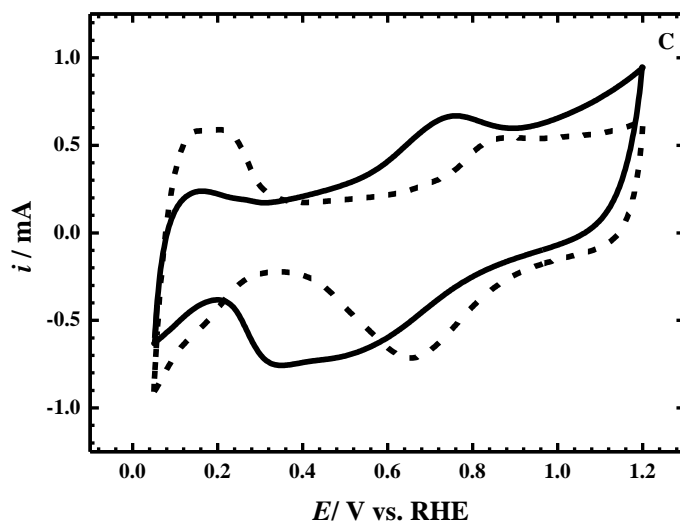
Regarding the crystallite size calculated from XRD (Table 3.2), it is obvious that at higher pH values or in the absence of PVP, considerably large nanoparticles form. Thus it can be summarized that on one hand, a low pH is necessary to avoid Cu hydroxides precipitation during catalyst synthesis, and on the other hand PVP is needed to avoid particle agglomeration at low pH.

3.3.3 Electrochemical Characterization

The initial cyclic voltammograms (CVs) obtained from the alloyed PtCu catalysts in addition to the final CVs of the dealloyed samples are presented in Figure 3.4. The samples PtCu/PVP₄₀₀, PtCu/PVP₅₀₀, and PtCu/PVP₆₀₀ displayed in Figure 3.4A-C exhibit similar electrochemical characteristics. A broad current peak in the potential range between 0.5 and 0.9 V/RHE during the positive potential sweep was observed in the initial CV, signifying the Cu dissolution from the PtCu alloy nanoparticles [37]. The appearance of the $H_{\text{ads/des}}$ regime in the potential range between 0.05 and 0.3 V/RHE in the first cycle indicates the presence of Pt atoms on the particle surface. A Pt rich surface could be explained by the low copper content in these electrocatalysts. Furthermore, the intensity of $H_{\text{ads/des}}$ peaks starts to increase gradually with the fast dealloying CVs and after the dealloying process the Pt features are well-developed while no remaining surface copper dissolution is visible in the CVs. On the other hand, the initial CVs of PtCu/PVP_{pH=11/pH=8} and PtCu catalysts Figure 3.4D-F don't

displayed any peak related to a Pt surface (i.e. no H_{upd} behaviour), which is a good indication of the formation of Cu rich surfaces, as confirmed by two current peaks in the first CV at 0.4 and 0.55 V/RHE related to the dissolution of Cu from different surface environments in the PtCu alloy [37]. Upon Cu dissolution from the surface of the alloyed catalysts during the fast dealloying CVs the position of these two peaks shifts to 0.34 V/RHE and 0.76 V/RHE where the former relates to Cu dissolution from Cu and the latter to Cu dissolution from a PtCu alloy, respectively. Pt features are less pronounced in these samples.





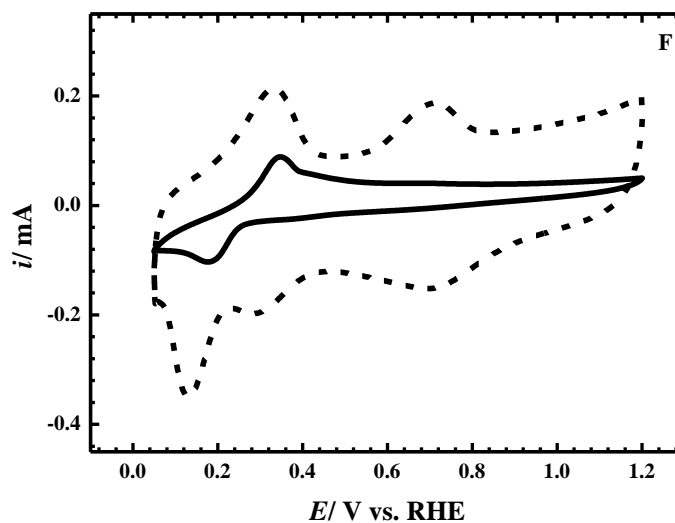


Figure 3.4: Cyclic voltammograms of the as-prepared (solid line) and dealloyed (dashed line) catalysts: **A)** PtCu/PVP₆₀₀, **B)** PtCu/PVP₅₀₀, **C)** PtCu/PVP₄₀₀, **D)** PtCu/PVP_{pH=11}, **E)** PtCu/PVP_{pH=8}, and **F)** PtCu conducted in N₂ -purged 0.1 M HClO₄, and scan rate of 100 mV s⁻¹.

In order to evaluate the intrinsic electrocatalytic activity of Pt based electrocatalysts, it is important to determine the real surface area of such electrocatalysts, which is required to calculate the specific activity of a given electrochemical process. The oxidation of an adsorbed monolayer of carbon monoxide on a platinum surface (so-called CO stripping) is an established technique for active surface area determination. The electrochemical active surface area (ECSA) of the electrocatalysts was calculated using (Equation 2.6) and is presented in Table 3.3.

Table 3.3: Electrochemical surface area (ECSA), average number of electrons (n) at 0.4 V vs. RHE, mass and surface specific activity (i_m and i_s respectively) of the electrochemically dealloyed PtCu catalysts.

Catalyst	ECSA/m ² g ⁻¹ Pt	n	i _m / mA mg ⁻¹ Pt		i _s / μA cm ⁻²	
			0.85V	0.9V	0.85V	0.9V
PtCu/PVP ₆₀₀	50.02	3.6	188.9	49.13	377.76	98.23
PtCu/PVP ₅₀₀	68.87	3.4	257.26	60.79	373.51	88.26
PtCu/PVP ₄₀₀	83.17	3.5	188.02	39.38	224.32	47.87
PtCu/PVP _{pH=11}	24.52	3.7	332.11	83.72	1354	341.3
PtCu/PVP _{pH=8}	24.97	3	137.13	31.63	549.16	126.3
PtCu	7.95	3.6	25.23	5.19	317.29	42.81

The CO stripping voltammograms of the Pt-Cu electrocatalysts are shown in Figure 3.5. The catalysts prepared with PVP and annealed at different temperatures show the typical behavior for Pt based catalysts: at low potentials in the forward scan a featureless CV is observed due to the poisoning of the surface with CO. An oxidation peak around 0.81 V vs. RHE follows, which is identical to the CO oxidation peak on a pure Pt surface [88]. In the backward scan, reduction of Pt oxides can be observed at ca. 0.7 V as well as the formation of adsorbed H (H_{upd}) between 0 and 0.2 V vs. RHE on the surface liberated from CO during the forward scan. However, the behavior is different for the catalysts PtCu/PVP_{pH=11/pH=8} and PtCu; these show a ~50 mV shift of the CO oxidation peak to less positive potentials. Probably during the leaching process low coordinated Pt atoms form which serves as active adsorption sites for water activation, resulting in adsorbed OH species that help to remove CO. Furthermore, in the low potential region these catalysts exhibit peaks attributed to the dissolution and deposition of Cu, indicating that even after extended leaching still Cu may be liberated from the catalysts surface.

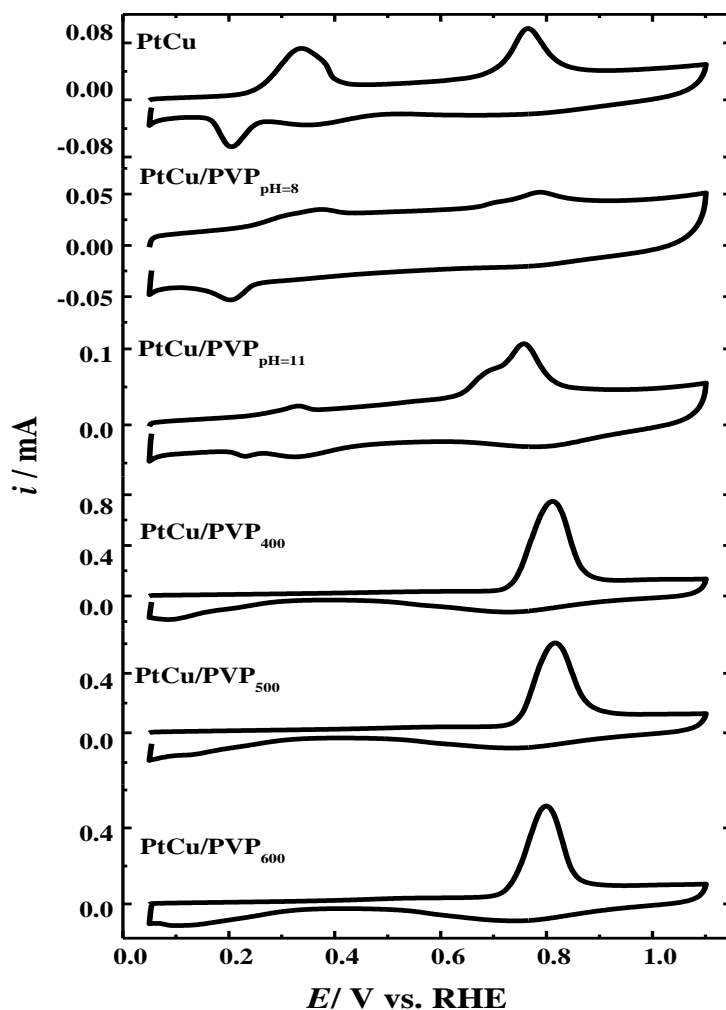


Figure 3.5: CO stripping voltammograms for all dealloyed catalysts obtained in N_2 -saturated 0.1 M $HClO_4$ with sweep rate of 20 mV s^{-1} .

Selected linear sweep voltammograms (LSV) of the dealloyed PtCu alloy electrocatalysts for ORR obtained with the rotating disk electrode in oxygen saturated 0.1 M $HClO_4$ are displayed in Figure 3.6. The dealloyed catalysts prepared with PVP at different annealing temperatures and the one prepared at pH=11 exhibit well-defined diffusion limited currents for ORR in the potential range from 0.05 to 0.7 V followed by a mixed kinetic-diffusion regime in a potential range from 0.7 to 0.95 V while at higher potentials the reaction is mainly under kinetic control. For the dealloyed catalyst prepared without modification and that prepared at pH=8 these values are shifted negatively by ca. 100 mV, indicating lower activity of the electrode for ORR (however,

see below for specific activities). In particular for the catalysts prepared without PVP or at higher pH, the dissolution and deposition of Cu may also occur as seen e.g. in the CO stripping voltammograms of Figure 3.5. However it is expected that these currents do not influence the oxygen reduction results directly due to two reasons: The Cu-related currents occur at a potential of ca. 0.2-0.4 V vs. RHE, while the region of kinetic control of oxygen reduction is much more positive, as mentioned above. Secondly, the RDE measurement is carried out at very low scan rates (5 mV s^{-1}), i.e. in a stationary regime, and thus surface-bound effects like upd will only marginally influence the results.

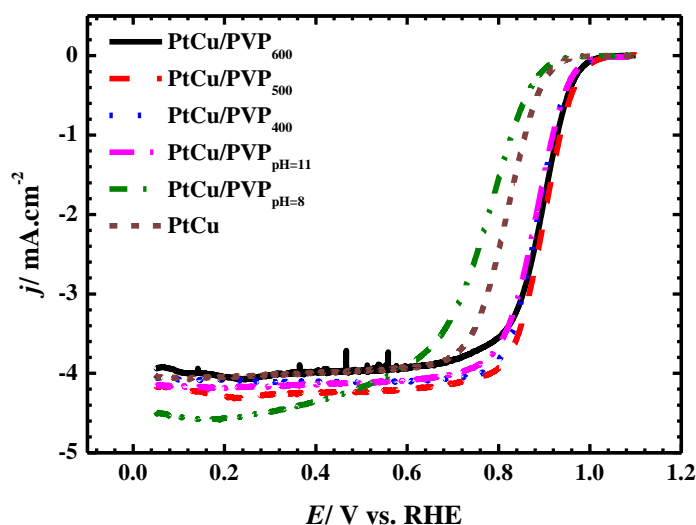


Figure 3.6: Single sweep voltammograms of the oxygen reduction measured on dealloyed PtCu catalysts at an electrode rotation speed of 900 rpm, sweep rate of 5 mV s^{-1} in O_2 -saturated 0.1 M HClO_4 electrolyte.

The kinetic current density for the ORR of the dealloyed PtCu catalysts was calculated by the Koutecky-Levich equation (Equations 3.1 and 3.2) [28, 100, 101].

$$\frac{1}{j} = \frac{1}{j_k} + \frac{1}{j_d} = \frac{1}{j_k} + \frac{1}{B\omega^{1/2}} \quad \text{Equation 3.1}$$

$$j_d = 0.62nFD^{2/3}\nu^{-1/6}C\omega^{1/2} = B\omega^{1/2} \quad \text{Equation 3.2}$$

Where j is the measured current density, j_k kinetic current density, j_d refers to the measured diffusion limited current density, B is a constant, ω is the electrode rotation speed, n is the number of electrons, F is the Faraday constant (96485 C mol^{-1}), D is the diffusion coefficient of oxygen ($1.93 \times 10^{-5} \text{ cm}^2 \text{ s}^{-1}$), ν is the kinematic viscosity of the

solution ($1.009 \times 10^{-2} \text{ cm}^2 \text{ s}^{-1}$), and C is the concentration of O_2 dissolved in electrolyte ($1.26 \times 10^{-3} \text{ mol L}^{-1}$) [100, 101].

The Koutecky-Levich plots in Figure 3.7 display the inverse of the current density vs. the inverse of the square root of the rotation speed at a fixed potential. The slope ($1/B$) of the straight line can be used to calculate the average number of electrons participating in the oxygen reduction reaction, while the intercept is used to evaluate the kinetic current density, which is usually taken as a measure of electrocatalytic activity. For comparison between the individual samples, the activity is either expressed as surface specific activity (i.e., kinetic current per active surface area (ECSA) as determined above) or as mass specific activity (i.e., kinetic current per mass of Pt). The mass and surface specific activities at 0.85 and 0.9 V vs. RHE for the dealloyed PtCu catalysts are presented in Table 3.3.

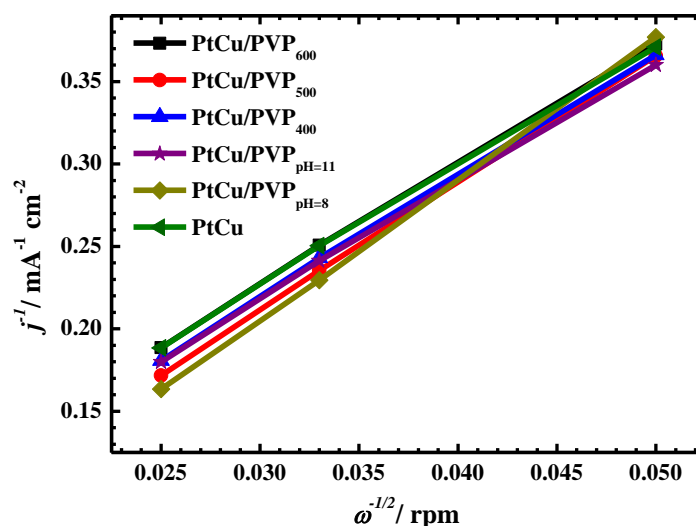


Figure 3.7: Koutecky-Levich plots for oxygen reduction reaction on dealloyed catalysts at 0.4 V vs. RHE, as obtained from RDE measurements in O_2 -saturated 0.1 M HClO_4 (comp. **Figure 3.6**)

$\text{PtCu/PVP}_{\text{pH}=11}$ shows the highest mass specific and surface specific activity towards oxygen reduction reaction at both potentials although its electrochemical active surface area is much lower than that of the samples PtCu/PVP_{400} , PtCu/PVP_{500} and PtCu/PVP_{600} . The low surface area certainly is due to the lower Pt content and the high degree of agglomeration. The higher surface-specific activity could be attributed to the

higher Cu content compared to the other catalysts. As confirmed from XRD analysis based on the positive shift in the 2θ , Cu incorporates into the face centred cubic (FCC) structure forming a PtCu alloy with altered electronic structure, which remains after core-shell formation upon dealloying. It should be noted that the PtCu/PVP_{pH=11} catalyst exhibits activities approaching that demonstrated by Koh and Strasser [37]. Furthermore, the PtCu/PVP_{pH=11} catalyst displays higher mass and surface specific activity than Pt_xCu_{1-x} nanoparticles supported on nitrogen doped carbon nanotubes synthesised via ultrasound-assisted redox replacement [102]. In particular, the mass activity of our PtCu/PVP_{pH=11} catalyst was found to be 7.5 and 2 times higher than the activity of Pt₂₅Cu₇₅ and Pt₅₀Cu₅₀ catalysts respectively and 1.5 times higher than that of Pt₅₀Cu₅₀ at 0.9 V vs.RHE however, the Pt₂₅Cu₇₅ catalyst showed no activity towards ORR at 0.9 V vs. RHE [102]. Furthermore, PtCu/PVP_{pH=11} exhibits higher mass and surface specific activities in comparison with other bimetallic systems such as Pt_xPd_{1-x}/MCNTs catalyst, where the highest mass and specific activity achieved was 64 mA/mg_{Pt} and 378 mA/cm⁻² respectively [103], or PtNi@Pt/C catalysts [104]. In the latter case, the lower activity was attributed to (i) using 0.5M H₂SO₄ as the electrolyte and (ii) applying a negative voltage sweep for ORR activity determination. By avoiding these two issues, slightly enhanced ORR activity could be observed [27]. Finally higher activities were obtained compared to alloyed and non-alloyed PtCo/C, PtCr/C and PtCoCr catalysts [105].

3.4 Conclusions

In this chapter microwave-assisted polyol synthesis was used for preparation of PtCu catalysts. The influence of preparation conditions on the structure of PtCu/CNTs catalysts was investigated and evaluated towards oxygen reduction activity. PVP as a stabilizer during the preparation steps resulted in catalysts with high Pt loading, high dispersion but small Cu loadings. Increasing the pH of the polyol synthesis in the presence of PVP increased the Cu loading, probably by precipitation, but decreased the loading of Pt, and the nanoparticles were highly agglomerated on the CNTs. A low pH in absence of PVP resulted in agglomerated Pt-Cu nanoparticles with high Pt loading. Obviously, PVP plays an important role in metal nanoparticles dispersion, while the pH during microwave-assisted polyol reduction can control the metal loading. In general, it can be concluded that the polyol reduction is an easy and feasible way to prepare PtCu catalysts with low particle size and high dispersion on the supporting CNTs. High

surface-specific activity was found for the copper-rich sample PtCu/PVP_{pH=11}, however with the drawback of low Pt loading and high agglomeration. In chapter 4, further activities have been done aiming to enhancing the Cu loading in the catalyst to achieve high surface specific activities while maintaining high Pt content and high dispersion.

4 Electrochemical Dealloying of PtCu/CNTs Electrocatalysts Synthesised by NaBH₄-Assisted Polyol-Reduction: Influence of Preparation Parameters on Oxygen Reduction Activity

Reprinted from ref. [65] with permission of Elsevier, copyright© 2015.

4.1 Introduction

In chapter 3 the PtCu/CNTs alloy catalysts were prepared by microwave assisted polyol synthesis and the influence of different synthesis parameters on the structure of the synthesized catalysts and their activity towards oxygen reduction reaction (ORR) was evaluated. During these investigations it turned out that it is a considerable challenge to prepare bimetallic nanoparticles containing Pt and Cu in a single reduction step using the polyol method, similar as reported before for PtNi and PtRu [87, 106]. In continuation of these activities we discuss in this chapter the synthesis efforts of PtCu/CNTs nanoparticles in two reduction steps procedure (see section 2.2.2). The first reduction step fulfill by using NaBH₄ (reducing agent) while the second step accomplished by the microwave-assisted-polyol reduction, in which ethylene glycol is used as a solvent and reducing agent. The influence of reduction conditions such as: the metal to NaBH₄ ratio, conventional heating vs. MW irradiation, and the order of reduction steps has been optimized towards ORR activity. The alloyed PtCu/CNTs electrocatalysts were dealloyed electrochemically to form PtCu_{core}Pt_{shell} structures and were investigated towards ORR.

4.2 Electrochemical Measurements Protocol

Cyclic voltammetry (CV) experiments were conducting in N₂-deaerated 0.1 M HClO₄ electrolyte and under N₂ atmosphere in a potential window from 0.05 V to 1.2 V vs. RHE. The dealloying protocol started with three CVs at a scan rate of 100 mV s⁻¹ to observe the initial dissolution of Cu from the catalyst, followed by 1600 CVs at 1000 mV s⁻¹ in order to induce considerable Cu dissolution from the sample. Finally, three CVs with a scan rate of 100 mV s⁻¹ were recorded to determine the electrochemical surface area of the dealloyed catalysts. Thereafter, the oxygen reduction activity of the dealloyed catalysts was monitored by linear sweep voltammetry (LSV) performed in O₂ saturated 0.1 M HClO₄ electrolyte solution by sweeping the potential positively from 0.05 to 1.1 V vs. RHE at a scan rate of 5 mV s⁻¹. The oxygen reduction reaction (ORR)

polarization curve were recorded at rotation speeds of 400, 900 and 1600 rpm and corrected for mass transport limitation to determine the kinetic current.

4.3 Result and Discussion

4.3.1 XRD Characterization

Figure 4.1 compares the X-ray diffraction profiles of the heat treated PtCu/CNTs electrocatalysts with the commercial Pt/C. Pt and Cu both display the cubic closed-packed structure [107], which gives characteristic XRD diffraction peaks associated with the 111, 200 and 220 planes at 2θ values of 44° , 51° and 74° for Cu and 39.9° , 46.5° and 67.8° for Pt respectively [55, 95]. The XRD patterns of the Pt/C catalyst and the PtCu catalysts displays one major diffraction peak corresponding to the 111 plane. The position of this peak is shifted for the PtCu catalysts to a higher diffraction angle relative to Pt/C, indicating incorporation of copper atoms into the platinum fcc structure to form an alloy phase accompanied by a lattice contraction. However the extent of shifting (and thus the degree of alloying) strongly depends on the synthesis procedure. For the catalyst PtCu_{50MS} (trace E), there is a slight shift to higher 2θ with an additional shoulder at higher diffraction angles (see below). A medium shift is observed for the samples where first the sodium borohydride reduction was carried out (B, C and D in Figure 4.1) while the sample PtCu_{50S} shows a 111-peak close to the value of Cu (trace F). An additional narrow peak or shoulder nearby to the main diffraction peak is seen in most of the PtCu samples, indicating the presence of unalloyed Cu or a very Cu rich alloy. The stoichiometric ratio of the alloyed catalysts was determined using Vegard's rule using Equation 2.1. The mean crystallite size, the interplaner distance, and the lattice parameters of the alloyed nanoparticles have also been determined using Equations 2.2-2.4). The most intense peak corresponding to the plane 111 was employed for these calculations and the data is summarized in Table 4.1.

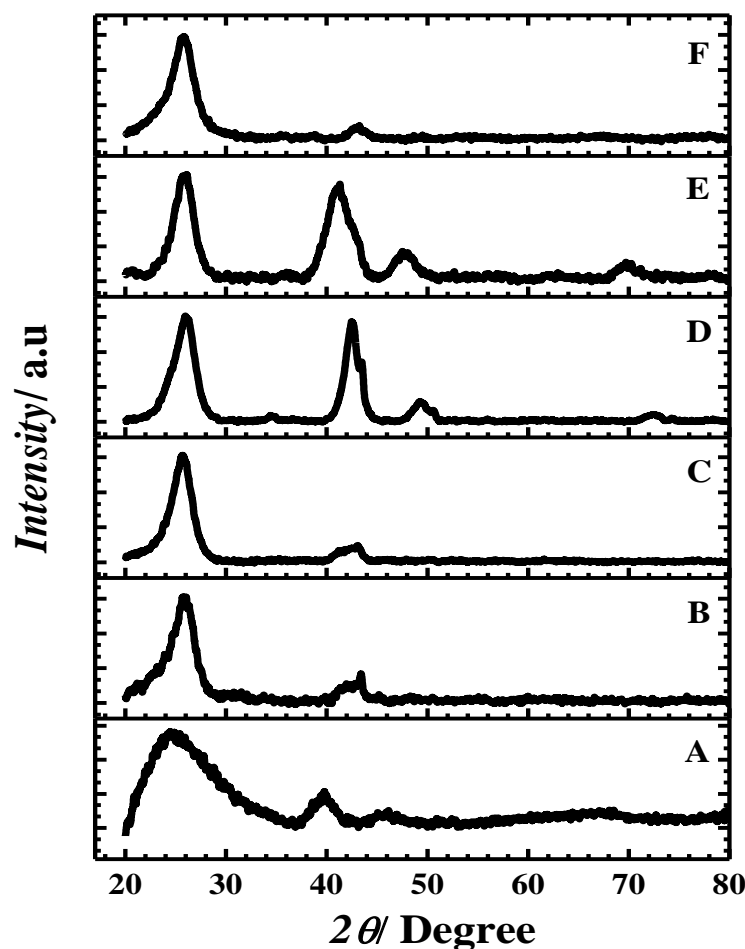


Figure 4.1: XRD pattern of the prepared electrocatalysts A) Pt/C, B) PtCu_{10SM}, C) PtCu_{10SC}, D) PtCu_{50SM}, E) PtCu_{50MS}, and F) PtCu_{50S}.

4.3.2 ICP-OES and TEM Characterization

The ICP-OES results of the synthesized catalysts presented in Table 4.1 show that the nominal metal loading (30%) has not been accomplished. The maximum loading was ca. 15% for the PtCu_{50SM} catalyst. In the previous chapter (chapter 3), we have described that the presence of PVP leads to a loading lower than the nominal one in microwave assisted reduction. Similarly, in the present case in absence of PVP high metal loadings are achieved, however at the price of high agglomeration (Figure SI 4.1). It seems that even with two reduction steps as in this study achieving high metal loadings remains a challenge when using PVP. During the MW reduction step the temperature of the reaction mixture (as shown in Figure SI 4.2) is higher than the melting point of the PVP ca.150 °C. It has been suggested that PVP forms a skin layer

on the metal surface in a core-shell like structure [108], stabilizing the nanoparticle however facilitating its removal during the washing step. Anyhow, the two-step reduction presented in this chapter is clearly advantageous compared to the previously used one step procedure employing only the polyol reduction step (chapter 3) since the relative copper loading is much higher in the two step-approach. We conclude that while the polyol approach is fine to prepare monometallic Pt catalysts, it is less suited to prepare PtCu catalysts with a high Cu loading. Here, the second reduction step using NaBH₄ is necessary to achieve high Cu loadings. It should be mentioned that NaBH₄ reduction alone equally does not lead to high loading. From Table 4.1 one can see that the total metal loading ca. 3.5% determined from the ICP-OES for the PtCu_{50S} sample is far below that of the other samples. Easton et al. [109] face also a challenge concerning the metal loading during the preparation of PtCu/C and Pt(Cu)/C catalysts where the reduction was achieved by NaBH₄ through one and two reduction step-processes, respectively. The loading of their catalysts as determined from the ICP-OES was found to be lower than the nominal one for both catalysts, with an increase in atomic percent of Pt and a decrease in Cu atomic percent.

Table 4.1: XRD data established from the 111 peak, TEM and ICP-OES data analysis of the alloyed PtCu/CNTs catalysts.

Catalyst	$2\theta_{\max}$	d/ nm	a_{alloy} Å°	FWHM	Crystallite size _{XRD} /nm	Particle size _{TEM} /nm	Pt:Cu ^[a]	Pt:Cu ^[b]	Wt. % Measured by ICP		
									Pt	Cu	Total
Pt/C	39.6	0.232	4	2.3	3.5	2.3	Pt ₁₀₀	Pt ₁₀₀	20	—	20
PtCu _{10SM}	42.6	0.212	3.68	2.9	2.8	2.7	Pt ₂₂ Cu ₇₈	Pt ₂₃ Cu ₇₇	4.5	4.7	9.2
PtCu _{10SC}	42.3	0.213	3.69	3.1	2.6	2.4	Pt ₂₈ Cu ₇₂	Pt ₂₄ Cu ₇₆	3.1	3.3	6.5
PtCu _{50SM}	42.5	0.212	3.67	1.7	4.7	3.3	Pt ₂₀ Cu ₈₀	Pt ₁₉ Cu ₈₁	5.9	8.4	14.3
PtCu _{50MS}	41.3	0.218	3.91	3.0	2.7	2.5	Pt ₅₃ Cu ₄₇	Pt ₄₂ Cu ₅₈	8.5	4.0	12.6
PtCu _{50S}	43.1	0.209	3.69	1.9	4.3	2.1	Pt ₇ Cu ₉₃	Pt ₁₀ Cu ₉₀	0.8	2.6	3.4

[a] calculated from Vegard's rule, [b] calculated from ICP.

From Table 4.1 it is furthermore obvious that the order of reduction steps additionally influences the metal loading. If the polyol reduction is applied first, a high Pt loading however with a relatively lower Cu loading is achieved (comp. PtCu_{50MS} and PtCu_{50SM}). Probably on the Pt particles formed in the first reduction step, NaBH₄ is catalytically decomposed and thus is not available for Cu ions reduction, in agreement with the dependence of the Cu loading on NaBH₄ ratio (comp. PtCu_{10SM} and PtCu_{50SM}). The lower Pt loading for those samples prepared by NaBH₄ reduction in the first reduction step is more difficult to explain.

TEM images of the Pt/C and the alloyed PtCu catalysts Figure 4.2 were recorded to elucidate the morphologies and the particle sizes. The mean particle sizes of the alloyed catalysts were in the range of 2.1 to 3.3 nm and close to the results obtained from XRD (Table 4.1). Moreover, TEM measurement for the alloyed catalysts revealed that particle size and metal dispersion over the CNTs depend strongly on the order of reduction steps. PtCu_{10SC} shows a higher degree of agglomeration in comparison with PtCu_{10SM} underlining the role of uniform heating by MW in avoiding nanoparticles agglomeration. Furthermore, starting with the microwave polyol reduction instead of NaBH₄ in PtCu_{50MS} gives rise to highly dispersed, uniform, and spherical nanoparticles in comparison with the PtCu_{50SM} catalyst.

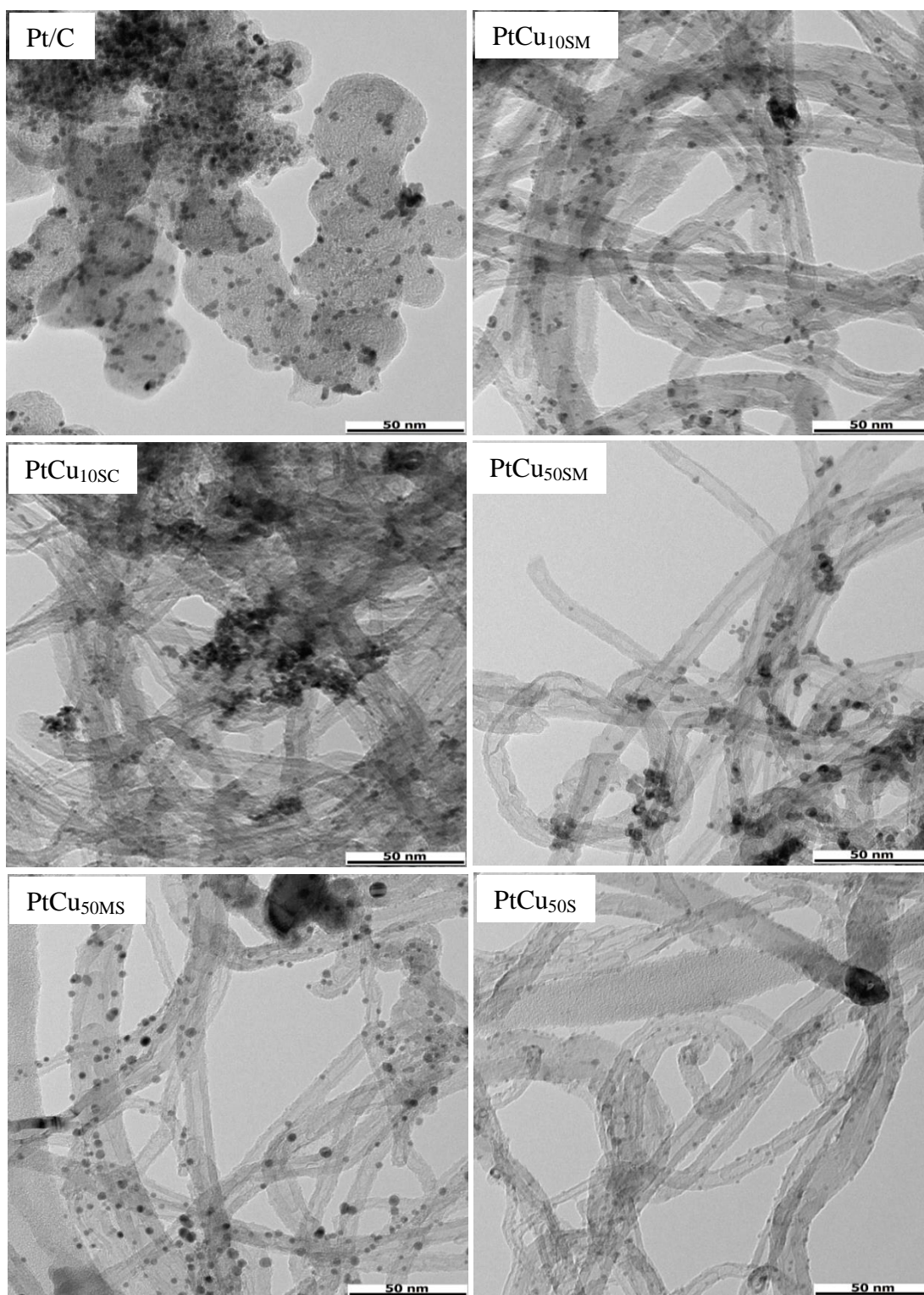


Figure 4.2: TEM images of the prepared catalysts.

4.3.3 Electrochemical Characterization

The initial cyclic voltammograms (CVs) of the alloyed PtCu catalysts in comparison with the dealloyed profiles (red lines) are illustrated in Figure 4.3. The initial CVs show no hydrogen adsorption/desorption peaks ($H_{\text{ads/des}}$, 0.05-0.3 V vs. RHE), indicating a surface mainly covered by Cu in the Cu-rich alloys. All PtCu catalysts exhibit an anodic peak at 0.3-0.6 V vs. RHE, indicating the dissolution of pure unalloyed Cu occurring close to the Cu standard potential [110]. An exception is the PtCu_{50MS} catalyst where a peak at 0.45-0.85 V vs. RHE is attributed to Cu dissolution from a PtCu alloy. This difference is in agreement with the XRD results, where for the latter sample a Pt reflex with a shoulder in the region of PtCu alloys was found, while the former samples had reflexes close to that of pure copper.

Upon further dealloying, the intensity of the Cu dissolution peak decreases while the $H_{\text{ads/des}}$ peak intensity increase gradually resulting in CV profiles resembling those of Pt. The $H_{\text{ads/des}}$ peak however is barely visible for the dealloyed PtCu_{50S} catalyst which is attributed to the low Pt content in this catalyst system. Figure 4.4 shows the CO stripping voltammetry of the catalysts of this study. The disappearance of the anodic current peaks due to H_{des} upon CO adsorption indicates that a complete CO monolayer is formed [111]. Total CO oxidation was confirmed from the presence of $H_{\text{ads/des}}$ peaks in the following CVs. The CO oxidation peaks of the dealloyed catalysts are shifted to a lower potential in comparison with the Pt/C catalyst. A lower CO stripping peak potential could be attributed to the modification of the electronic structure of the Pt surface, which may translate into an earlier formation of weakly adsorbed states of OH on platinum surface, at the same time enhancing the ORR as well [9]. The PtCu_{50SM} catalyst which has the most negative CO stripping peak potential of ca. 0.75 V vs. RHE was the most active catalysts towards the ORR, although its ECAS was 1.3 time lower than that of Pt/C (see below, Table 4.2).

The CO stripping peaks were used to determine the electrochemically active surface area (ECSA). The ECSA of the PtCu_{10SM} catalyst is 2.1 times higher than that of PtCu_{10SC}, underlining the advantages of MW processing compared to conventional heating. In the latter, a higher degree of agglomeration is leading to the lower surface area (comp. TEM-images, Figure 4.2). The ECSA of PtCu_{50MS} was found to be 1.5 times higher than that of PtCu_{50SM}, which can be attributed to different particle sizes.

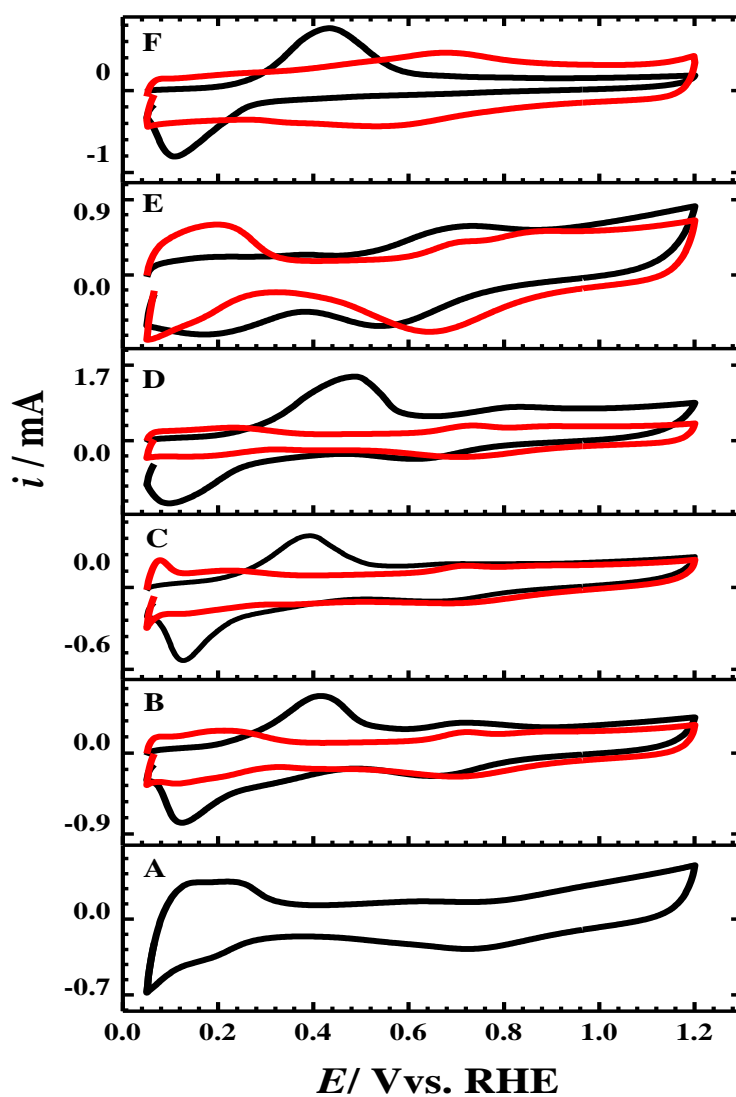


Figure 4.3: Initial CVs (black line) in comparison with the final CV of the dealloyed samples (red line), **A)** Pt/C, **B)** PtCu_{10SM}, **C)** PtCu_{10SC}, **D)** PtCu_{50SM}, **E)** PtCu_{50MS} and **F)** PtCu_{50S}.

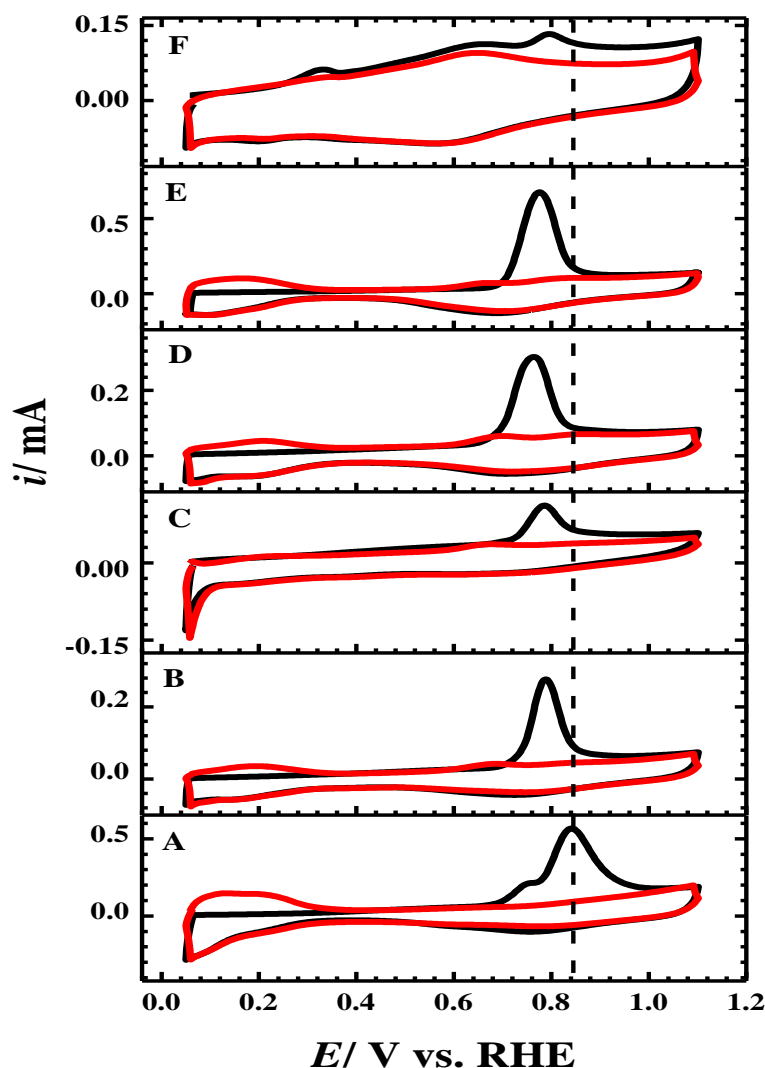


Figure 4.4: CO stripping voltammograms for the catalysts: **A)** Pt/C, **B)** PtCu_{10SM}, **C)** PtCu_{10SC}, **D)** PtCu_{50SM}, **E)** PtCu_{50MS} and **F)** PtCu_{50S}.

ORR polarization curves of the catalysts of this study, as obtained with the rotating disc electrode, are displayed in Figure 4.5A, showing the typical appearance with kinetically controlled and diffusion limited currents as well as the mixed kinetic/diffusion control. The diffusion controlled current density (j_d) in a rotating disc experiment is achieved when the surface concentration of the reactant drops to zero and is described by the Levich equation (Equation 3.2). The diffusion-limited regime turns into a mixed regime where the current is affected by both the reaction kinetics and the mass transport rate, finally the reaction rate is mainly kinetically controlled. The overall current density (j) in the entire potential region is related to the diffusion controlled

current density (j_d) and the kinetic current density (j_k) according to the Koutecky-Levich Equation 3.1.

According to Koutecky-Levich equation ($j^{-1}=j_k^{-1}+B^{-1}\omega^{-1/2}$), a plot of j^{-1} vs. $\omega^{-1/2}$ at a fixed potential yields a straight line with the slope $1/B$, as shown in Figure 4.5 B. The slope was used to determine the average number of electrons transferred per reduced oxygen molecule (n) which are given in Table 4.2.

The ORR polarization curves of Figure 4.5A were measured at 900 rpm. Differences in the diffusion-limited current densities could be attributed to the unequal electrode coverage with catalyst [112]. The onset and half wave ($E_{1/2}$) potentials of the ORR polarization curve are often used to compare the electrocatalytic activity of different electrocatalysts. For PtCu_{50SM} both potentials show the most positive shift indicating high ORR activity. However, for a more precise comparison of the samples, it is necessary to use the mass (i_m) and surface (i_s) specific activities. Both values were calculated according to Equations 4.1 and 4.2 respectively and the data are listed in Table 4.2. The mass specific activity is of importance from a commercial point of view since the cost of a fuel cell electrode largely dependent on the amount of Pt used, while the surface specific activity provides a measure of the intrinsic electrocatalytic activity of Pt atoms in the surface.

$$i_m = \frac{j_k}{L_{Pt}} * A \quad \text{Equation 4.1}$$

$$i_s = \frac{j_k}{ECSA} * A \quad \text{Equation 4.2}$$

Where j_k is the kinetic current density at the 0.9 V vs. RHE, L_{Pt} is the mass of Pt on the electrode, A is the electrode area (0.125 cm²) and ECSA is the electrochemical surface area obtained from CO stripping. The value of the mass specific activity of the catalysts increases in the order of: PtCu_{50MS} < PtCu_{50S} < Pt/C < PtCu_{10SC} < PtCu_{10SM} < PtCu_{50SM}. The catalyst PtCu_{50SM} is the most active sample with a 3.3 and 4.3 fold increases in the mass and surface specific activities respectively, compared to the commercial Pt/C catalyst. However, the PtCu_{50MS} catalyst shows a surface specific activity similar to Pt/C with a lower mass specific activity. The low activity of PtCu_{50MS} could be explained considering preparation and characterization. During preparation, first Pt is reduced to form Pt nanoparticles, as suggested by the X-ray diffractogram of the unalloyed catalyst Figure SI 4.3. These Pt nanoparticles might serve as catalytic

sites for the reduction of Cu and are possibly surrounded with Cu after the second reduction step. After heat treatment, a Pt core surrounded by a PtCu shell might form, in agreement with XRD, where a peak attributed to Pt with a shoulder attributed to PtCu alloy is visible and in agreement with CV, where a Cu dissolution from an alloy was observed in the initial scans. Likely during dealloying, major parts of Cu from the shell are lost, leaving behind a catalyst mainly consisting of Pt, in agreement with the Pt-like activity observed with this sample. However, certainly the mentioned experimental observations would also be in agreement with other catalyst structures, e.g. with nanoparticles consisting of pure Pt in parallel with PtCu alloy particles, which are small enough to release all their Cu during dealloying.

On the other hand, the PtCu_{SM50} sample is highly active after dealloying. In XRD the presence of a PtCu alloy with some free copper was detected. The dissolution of the latter is observed in CV. The activity improvement of the dealloyed PtCu_{50SM} catalyst is attributed to the electrochemical dissolution of the Cu atoms from the PtCu alloy and the formation of a Pt-enriched shell, as also indicated by preliminary XPS measurements shown in Figure SI 4.4. The resulting lattice strain in the Pt-enriched shell causes lowering in the Pt d-band center and weakens the chemisorption of oxygen species on the Pt surface which results in activity enhancement [113]. The mass specific activity exhibited by the PtCu_{50SM} catalyst was found to be higher than that exhibited by a PtCu catalyst prepared by the polyol method and annealed at 600 °C and 900 °C under reductive atmosphere, however, the latter shows specific activity a little bit higher [114]. Furthermore, the PtCu_{50SM} catalyst displays much higher mass and specific activities than the Pt_xM_{1-x} (M = Co, Ni, Cu) catalysts annealed at 350°C and 950 °C [115], approaching those demonstrated by Oezaslan and Strasser [116].

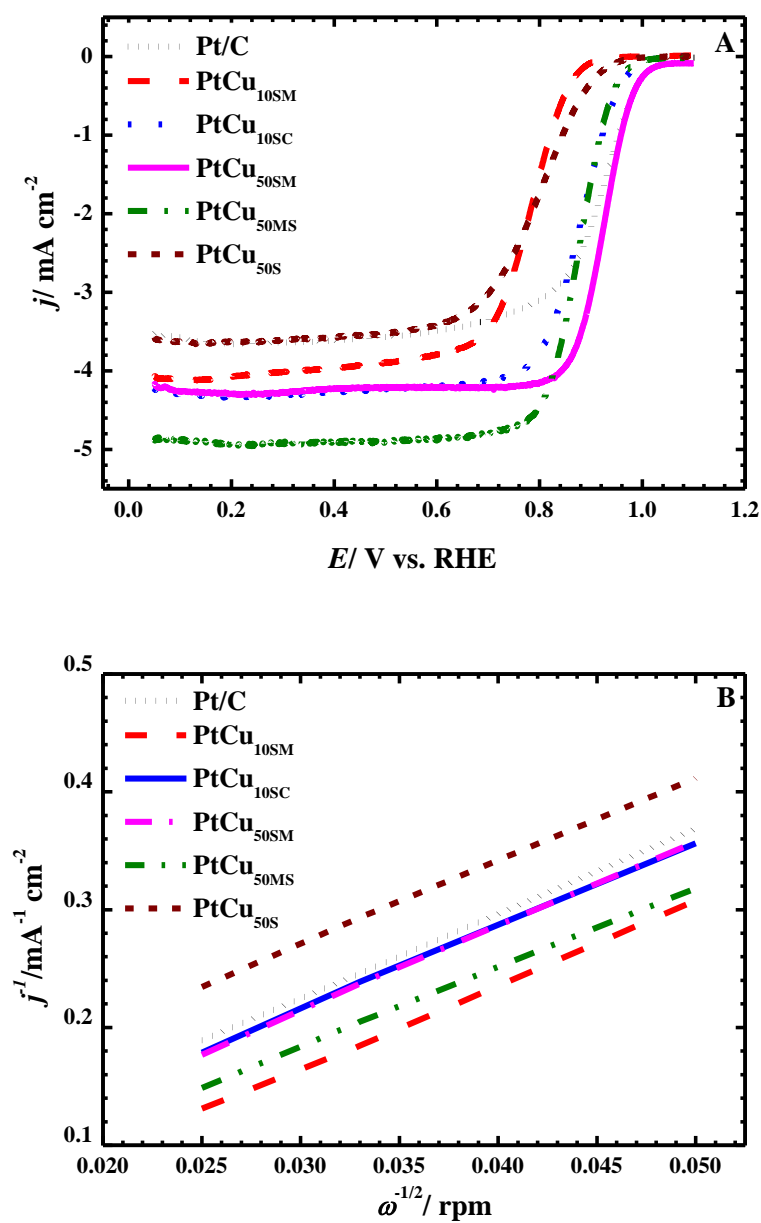


Figure 4.5: A) polarization curves of the dealloyed PtCu/CNTs and Pt/C catalysts, B) Koutecky-Levich plots for ORR at 0.6 V vs. RHE.

Table 4.2: Electrochemical data of the dealloyed PtCu/CNTs catalysts and Pt/C.

Catalyst	n	ECSA m ² g ⁻¹ _{Pt}	i _m mA mg _{Pt} ⁻¹	i _s μA cm ⁻²
Pt/C	3.6	87.18	94.19	108.04
PtCu _{10SM}	3.8	62.43	230.45	369.09
PtCu _{10SC}	3.7	29.51	135.29	458.34
PtCu _{50SM}	3.7	66.42	305.25	459.41
PtCu _{50MS}	3.9	97.9	48.01	106.16
PtCu _{50S}	3.6	29.82	74.95	251.31

In parallel to the above discussed study, the influence of the ink used for electrode preparation was investigated, since it became clear that these parameters have a strong influence on the observed activity. This study will be exemplified in the following using the most active sample PtCu_{50SM}. The changes in the electrochemical active surface area (ECSA) as well as the mass and surface specific activities upon using the same catalyst ink for electrode preparation for six consecutive days were investigated. The characteristic peak of surface copper dissolution in the initial CV of the aged catalyst gradually vanished with increasing ink age as shown in Figure 4.6 A. We attribute this to copper dissolution occurring already in the catalyst ink due to the acidic character of the Nafion solution used as binder during catalyst ink preparation. More intriguingly, changes are also found after electrochemical dealloying. As above, Pt-like features develop during dealloying, however the intensity of the H_{ads/des} peak was maximum after one day ink aging and the Pt-O reduction peak was found to shift positively suggesting an ORR enhancement Figure 4.6 B. Figure 4.7 summarizes the observed development of mass and surface specific activity as well as ECSA. The mass and surface specific activities reach its maximum value after one day of ink aging and then decrease gradually. Our result fit well with those reported by Strasser et al. [117], who suggested that the prepared catalyst inks should be left aging for at least 24 h and up to 48 h before film casting.

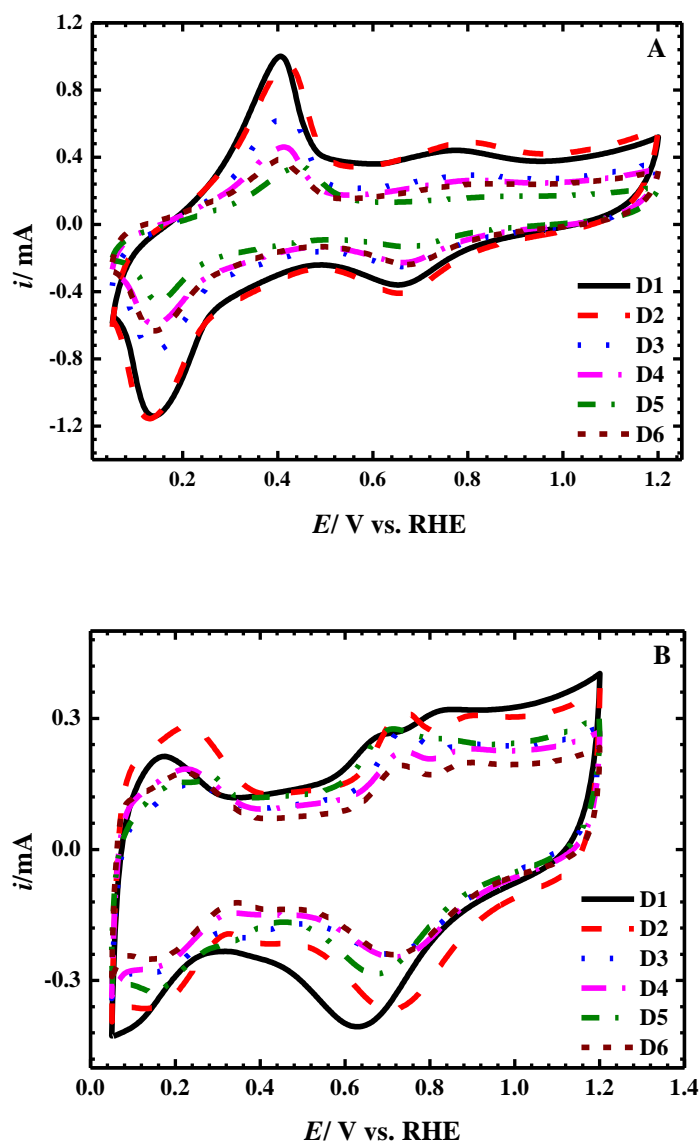


Figure 4.6: Cyclic voltammetric profiles of PtCu_{50SM} catalyst for six consecutive days A) before dealloying, B) after dealloying.

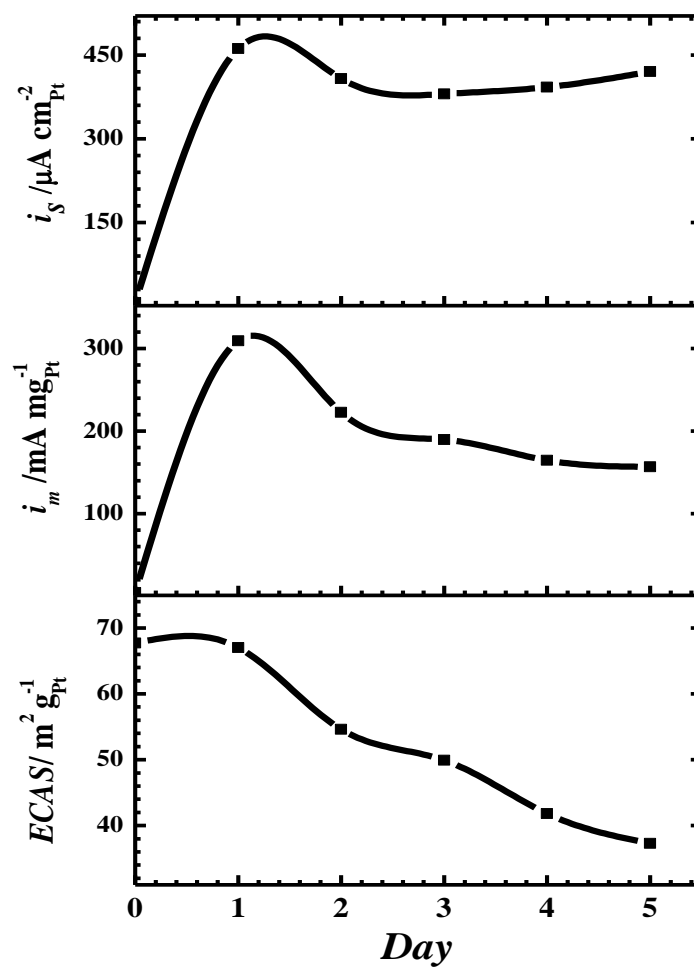


Figure 4.7: Effect of catalyst ink aging on the electrochemical performance of PtCu_{50SM} catalyst (the results of i_m and i_s was taken from the ORR polarization curve in O₂-saturated 0.1 M HClO₄, at 0.9 V vs. RHE and 900 rpm rotation rate).

4.4 Conclusions

This chapter presents a comparative study on structural and electrochemical characterization including determination of oxygen reduction reaction activity of CNTs-supported PtCu alloy nanoparticles synthesized by a modified polyol process. The addition of a second reduction step with NaBH₄ significantly enhances the copper content in the catalysts. XRD patterns of the alloyed Pt-Cu nanoparticles show a peak shift to a higher 2θ values indicating alloy formation. The Pt:Cu stoichiometric ratios were found to vary with variation in the order of the reduction steps as determined from Vegard's law and ICP-OES analysis. The dealloyed PtCu_{50SM} catalyst showed the highest activities towards ORR compared with commercial Pt/C and the other dealloyed Pt-Cu catalysts prepared under different experimental procedures. Further investigation employing on the PtCu_{50SM} catalyst shows that higher ORR activities can be achieved by aging the catalysts ink for 24 h before casting on the electrode.

4.5 Supporting Information

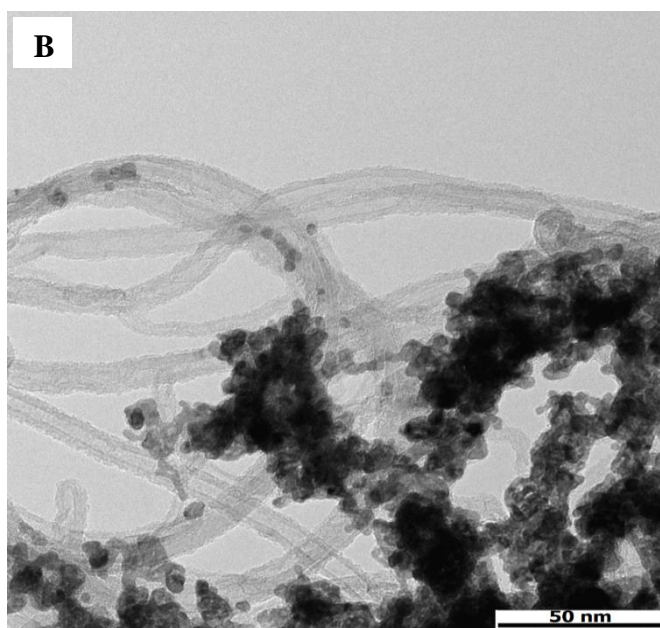
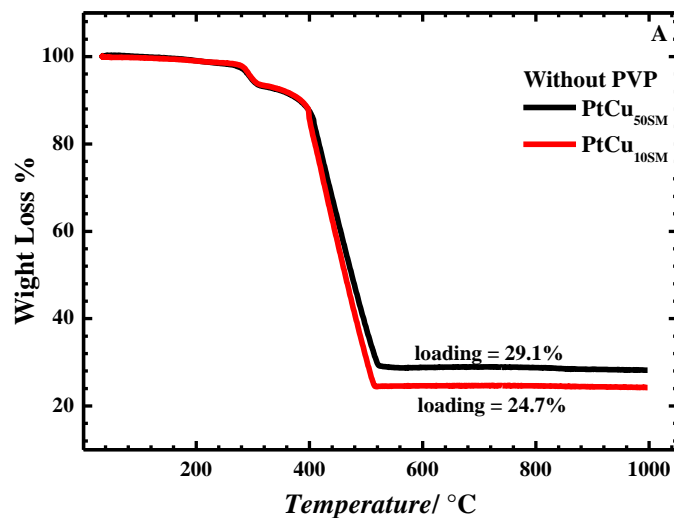


Figure SI 4.1: A) TGA analysis for the PtCu_{10SM} and PtCu_{50SM} catalysts prepared without PVP, B) TEM image for PtCu_{50SM} catalysts prepared without PVP shows the importance of introducing the PVP in during the peroration steps to avoid particles agglomeration.

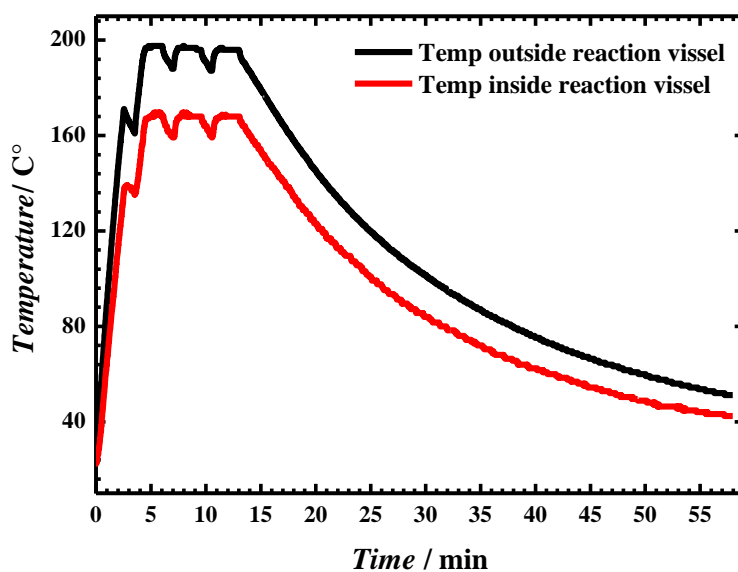


Figure SI 4.2: Temperature profile for the microwave synthesis of PtCu_{50MS}.

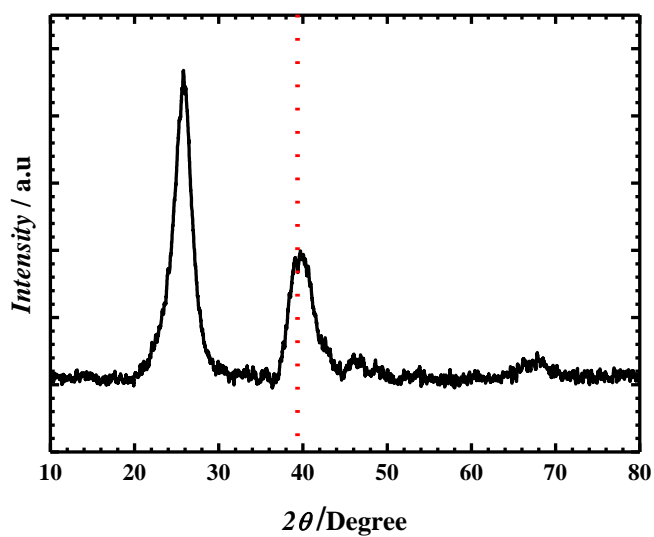


Figure SI 4.3: XRD pattern of the unalloyed PtCu_{50MS} catalyst.

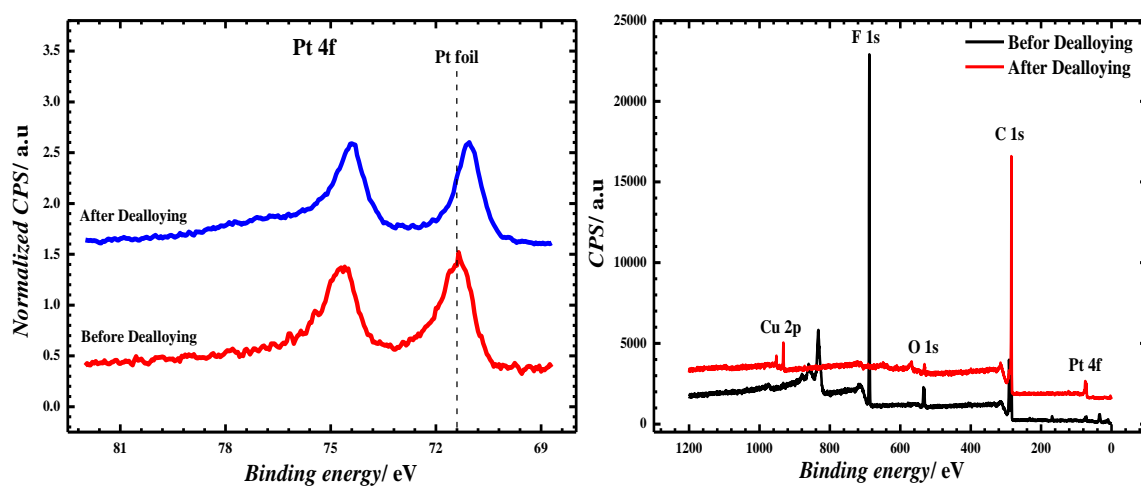


Figure SI 4.4: XPS of PtCu_{50SM}, the stoichiometric ratio was found to be Pt₃₃Cu₆₆ before dealloying and Pt₆₈Cu₃₂ after the dealloying.

5 Electrocatalytic Reduction of Oxygen on Chemically Dealloyed PtCu/CNTs Catalyst: Influence of Dealloying Time on Structure and Activity

**The following chapter is part of a publication currently prepared for submission^[a].*

5.1 Introduction

In this chapter, Pt-rich surface alloy nanostructure catalysts were prepared by chemical dealloying (i.e. selective chemical leaching of the less noble metal (M) from the M-rich Pt alloy precursor) of the optimized PtCu_{50SM} alloy precursor prepared in chapter 4. During this chapter the catalyst PtCu_{50SM} will be referred to as PtCu. The PtCu alloy nanoparticles were chemically dealloyed in 1 M HClO₄ at ambient temperature (see section 2.2.3). The influence of the dealloying time on structure and activity of the dealloyed catalysts toward oxygen reduction reaction was investigated after 15 min, 1 h, 2 h, 4 h, and 6 h of dealloying.

5.2 Electrochemical Measurements Protocol

The electrochemical measurements were performed in a conventional three-electrode cell, where the potential of the WE was monitored relative to reversible hydrogen electrode (RHE). For the counter electrode a piece of Pt net was used. For working electrode (WE) preparation, 10 μ l 24 h-aged-catalyst ink (for catalyst ink preparation, see section 2.3.2.1) were pipetted onto a polished glassy carbon rotating disk electrode with 4 mm diameter. The WE was kept under isopropanol atmosphere until complete dryness before introduction into the electrochemical cell. All electrochemical measurements were conducted in N₂ or O₂ saturated 0.1 M HClO₄, and the respective gas was purged over the electrolyte solution during the measurements. The chemically dealloyed catalysts were subjected to 25 cyclic voltammetric scans (CVs) in N₂-saturated 0.1 M HClO₄ and potential range 0.05-1.2 V vs. RHE with a scan rate of 100 mVs⁻¹ in order to, remove any surface contaminations and to obtain stable voltammograms. Thereafter, the electrochemically active surface area (ECSA) of the electrocatalysts was evaluated from the carbon monoxide stripping charge (ECSA_{CO}) and normalized charge of the underpotential deposited hydrogen stripping (ECSA_{Hupd}) as described in section 2.3.2.4.

[a] "Electrocatalytic Reduction of Oxygen on Chemically Dealloyed PtCu/MWCNTs: Influence of Dealloying Time on Structure and Activity." Heba El-Deeb, Ilja Sinev, Wolfgang Grünert, Michael Bron, in preparation.

The ORR activity was obtained through linear sweep voltammetry (LSV) by sweeping the potential in positive direction from 0.05 V to 1.1 V vs. RHE in oxygen saturated 0.1 M HClO₄ at a scan rate 5 mVs⁻¹ and rotation speeds of 400, 900, and 1600 rpm. The kinetic current density for ORR was corrected for mass transport limitations and evaluated at 0.9 V vs. RHE and 900 rpm rotation speed using Koutecky-Levich equation (Equation 3.1).

5.3 Results and Discussion

The XRD patterns of the chemical dealloyed catalysts are shown in Figure 5.1. All patterns exhibit a diffraction peak at $2\theta = 25.5^\circ$ typical for the 002 plane of the MWCNTs support and two peaks at ca. $2\theta = 41.5^\circ$ and $2\theta = 48.5^\circ$ characteristic for the 111 and 200 planes of the metal phase. The diffraction angles of the 111 and 200 planes exhibit a shift to a higher 2θ when compared with the pure Pt ($2\theta = 39.9^\circ$ and 46.5°), which is attributed to the substitution of Pt atoms with Cu atoms and the resulting contraction of the closed packed structure of the platinum lattice. Compared to the diffraction pattern of the PtCu alloy precursor pattern (A) in Figure 5.1 disappearance of the diffraction peak corresponding to the 220 plane and shifting of the diffraction angles of the 111 and 200 planes to lower 2θ values are observed, suggesting that Cu was removed from the lattice by chemical leaching. Indeed, the composition obtained by Vegard's law (Equation 2.1) Table 5.1 suggests, that the composition changes from 1:4 to a value close to 1:1, suggesting that chemical leaching dissolves significant amounts of copper from the material. The elemental surface composition was measured by X-ray photoelectron spectroscopy (XPS) and the values are summarized in Table 5.2 together with the composition determined by ICP-OES and TEM data (see below). The Pt:Cu atomic ratio on the surface of PtCu_{15min} and PtCu_{6h} is 1.82 and 2.2 times higher than that of alloy the precursor. Furthermore, the surface Pt:Cu ratio is significantly higher than the bulk values determined by XRD or ICP-OES. This clearly suggests that a Pt surface enrichment occurs during chemical leaching. Furthermore, the higher Pt:Cu ratios determined with ICP-OES compared to XRD can be easily understood by the fact that ICP-OES probes both the whole catalyst (surface and bulk) while XRD is dominated by the bulk composition. Additionally, the above findings point to the fact, that the chemical leaching does not leave the core of the alloy nanoparticle unaffected, as also recently shown [118].

Figure 5.2 shows the XPS Pt 4f and Cu 2p spectra of the dealloyed catalysts PtCu_{15min} and PtCu_{6h} in comparison with the PtCu alloy precursor along with line positions of bulk Pt and PtCu₃ references and carbon supported Pt nanoparticles of similar size. Both Pt and Cu are predominantly metallic in all samples. Pt doublets are well separated and there are no other evidences on higher Pt oxidation states formed. There is well defined shoulder at ca. 77 eV on the spectrum of the alloy precursor, which corresponds to the Cu 3p core level and disappears with copper being leached out. Copper is mostly metallic as well, however there are small indications on presence of shake-up satellites at ca. 944-945 eV typical for Cu²⁺ state. A positive shift of 0.2 and 0.3 eV in the Pt 4f_{7/2} core level binding energy parallel with a 0.2 and 0.25 eV negative shifts in the Cu 2p_{3/2} core level binding energy were observed for the PtCu_{15min} and PtCu_{6h} catalysts respectively, the shifts in the dealloyed catalysts were referenced to the PtCu alloy precursor, Table 5.2. The photoemission line positions for bulk Pt and PtCu₃ references as well as carbon supported Pt nanoparticles [87] measured using the same instrument provide allow to draw conclusions regarding platinum alloying in the samples. Carbon supported Pt nanoparticles show 0.4 eV shift to higher binding energies comparing to bulk platinum metal standard. At the same time, Pt 4f core level of PtCu alloy precursor has comparable shift in respect to PtCu₃ bulk standard indicating thus a well-alloyed structure. Shifting of the Pt 4f line to higher binding energies in chemically leached samples is clear evidence in alloy decomposition, although absolute values did not reach neither those of Pt nanoparticles nor bulk Pt standard. Notable is that Pt 4f peaks clearly change their shape upon chemical leaching the peak width increases, while asymmetry, typical for Pt⁰ state, changes. It is assumed, that this is a result of Pt 4f peaks being a formed by two overlapping peaks with close energy, most likely representing pure and alloyed Pt. Lee et al. [119] described the core-level binding energies shifts in the Pt 4f_{7/2} and Cu 2p_{3/2} peak position in the PtCu alloy as a function of the Pt concentration. They reported that when the amount of the platinum in the alloy increases the Cu 2p_{3/2} binding energy shifts to lower values which fits well with our results. For the Pt 4f_{7/2} peaks, however, the binding energy measured by Lee et al. [119] displays no measurable core level shift as the composition of the PtCu alloy changed in addition to, absence the charge transfer to the Pt d-band in the PtCu alloys. In summary, the catalyst characterization by XRD, XPS and ICP-OES suggests that the initially formed Cu-rich alloy is significantly depleted in Cu by

chemical leaching and that a core-shell-structure, where the shell composition is different to the core composition, forms.

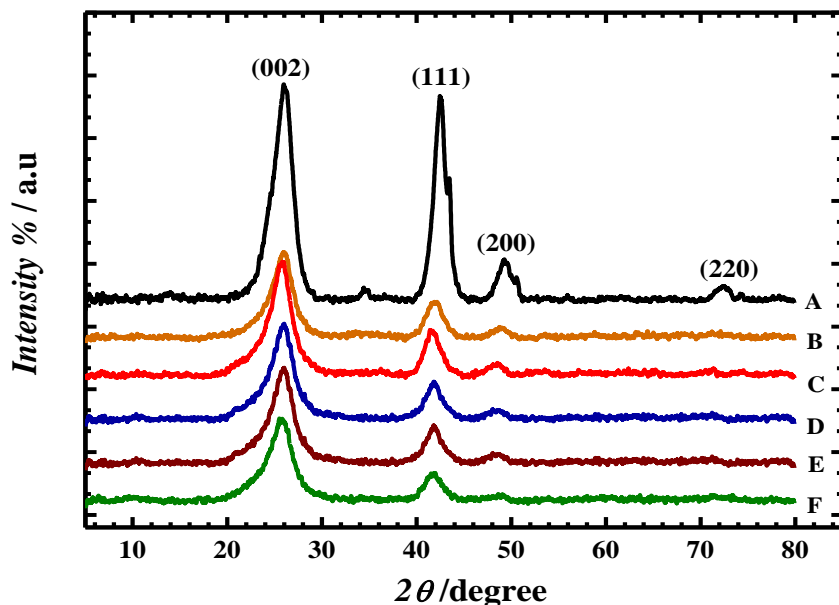


Figure 5.1: XRD pattern of the dealloyed catalysts **A)** PtCu, **B)** PtCu_{15min}, **C)** PtCu_{1h}, **D)** PtCu_{2h}, **E)** PtCu_{4h} and **F)** PtCu_{6h}.

Table 5.1: Catalysts crystallite and particle size and the corresponding ICP-OES metal ratio.

Catalyst	t/nm ^[a]	d/nm ^[b]	$a_{111}/\text{Å}$ ^[c]	at.% ^[d]	at.% ^[e]
PtCu	4.75	3.33	3.678	Pt ₂₀ Cu ₈₀	Pt ₂₁ Cu ₈₁
PtCu _{15min}	4.20	3.28	3.721	Pt ₃₅ Cu ₆₅	Pt ₄₉ Cu ₅₁
PtCu _{1h}	4.05	3.22	3.747	Pt ₄₄ Cu ₅₆	Pt ₄₈ Cu ₅₂
PtCu _{2h}	3.90	2.97	3.729	Pt ₃₈ Cu ₆₂	Pt ₄₄ Cu ₅₆
PtCu _{4h}	3.88	2.84	3.734	Pt ₄₀ Cu ₆₀	Pt ₄₉ Cu ₅₁
PtCu _{6h}	3.82	2.80	3.743	Pt ₅₈ Cu ₄₂	Pt ₅₂ Cu ₄₈

[a] crystallite size calculated from XRD = $\frac{0.89 \cdot \lambda}{FWHM \cdot \cos \theta_{(111)}}$, [b] mean particle sizes calculated from TEM = $\frac{\sum_i n_i d_i}{\sum_i n_i}$, n_i is the number of particles with diameter d_i (i : integer number), [c] lattice parameter $a = \frac{\sqrt{3} \cdot \lambda}{2 \sin \theta_{(111)}}$, [d] composition vegard's law and, [e] composition calculated from ICP

Table 5.2: XPS parameters.

Catalyst	Binding Energy	Binding Energy	Pt:Cu ^[a]
	Cu 2p _{3/2} /eV	Pt 4f _{7/2} /eV	
PtCu	932.47	71	Pt ₃₃ Cu ₆₇
PtCu _{15min}	932.27	71.2	Pt ₆₀ Cu ₄₀
PtCu _{6h}	932.22	71.3	Pt ₇₀ Cu ₃₀

[a] composition calculated from XPS

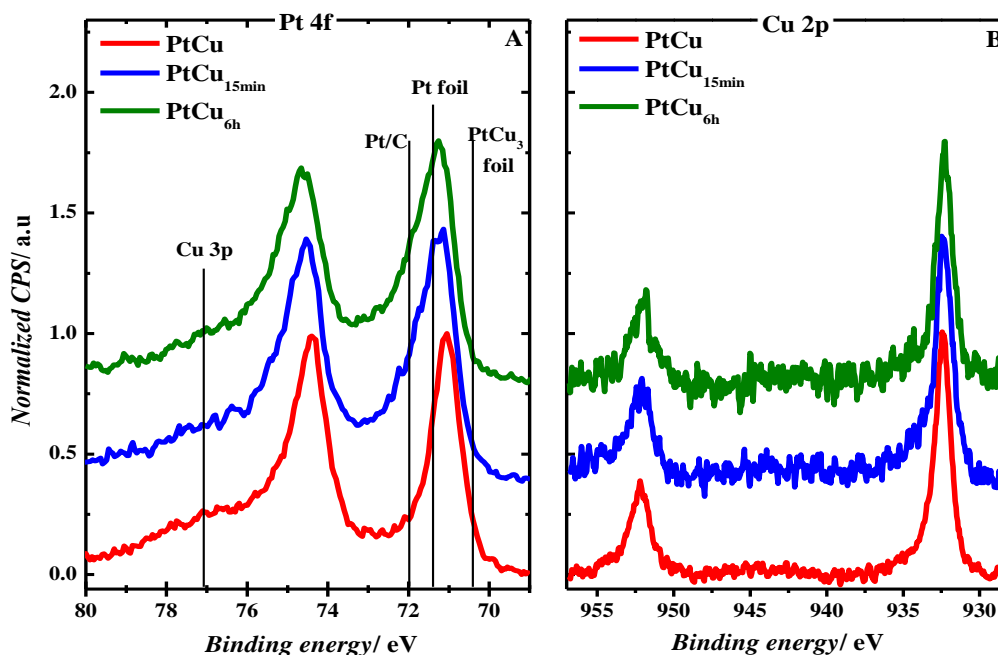
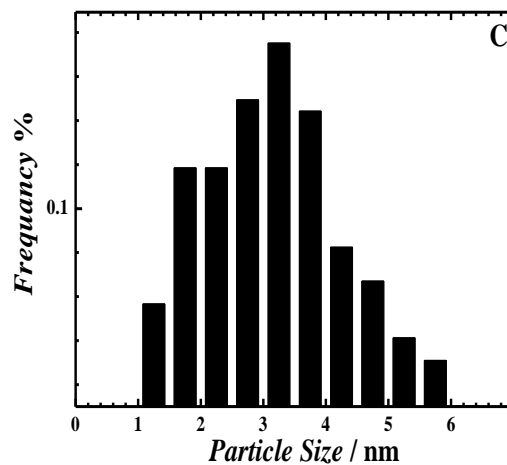
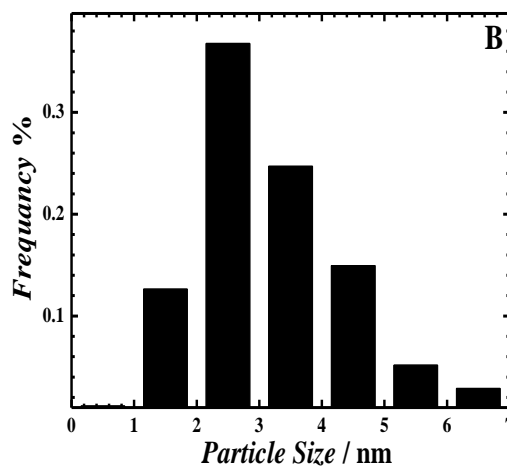
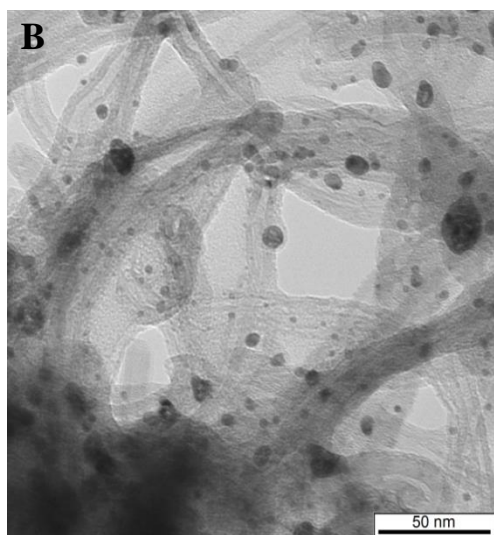
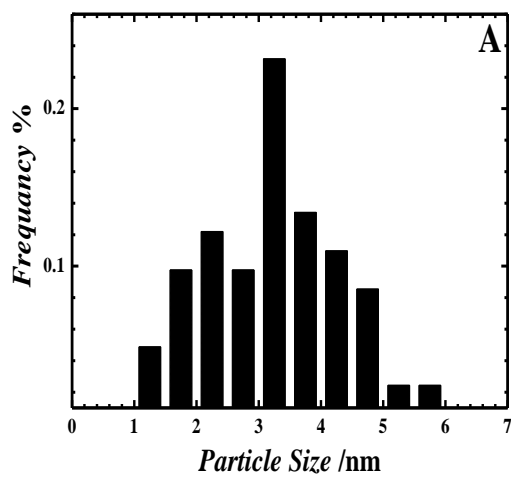
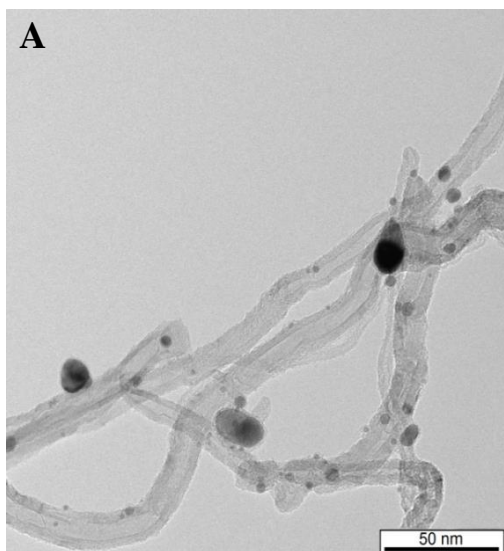
**Figure 5.2:** XPS spectra of the PtCu, PtCu_{15min} and PtCu_{6h} catalysts.

Figure 5.3 displays the transmission electron microscope (TEM) images of the alloyed precursor and the dealloyed catalysts after various dealloying times and the corresponding particle size distributions. The crystallite and the average particles size of the alloy precursor and the dealloyed catalysts were evaluated from XRD and TEM respectively and are listed in Table 5.1. The crystalline size was calculated from Scherrer's equation using the 111 peak. The size of nanoparticles established from TEM and XRD decreases gradually with increasing the dealloying time from 15 min to 6 h while the distribution of the PtCu nanoparticles over the O-CNTs support remains quite uniform. The decrease in particle size is in line with changes in the catalysts bulk composition obtained from ICP-OES data analysis and XRD, Table 5.1, i.e. with loss of material from the particles.



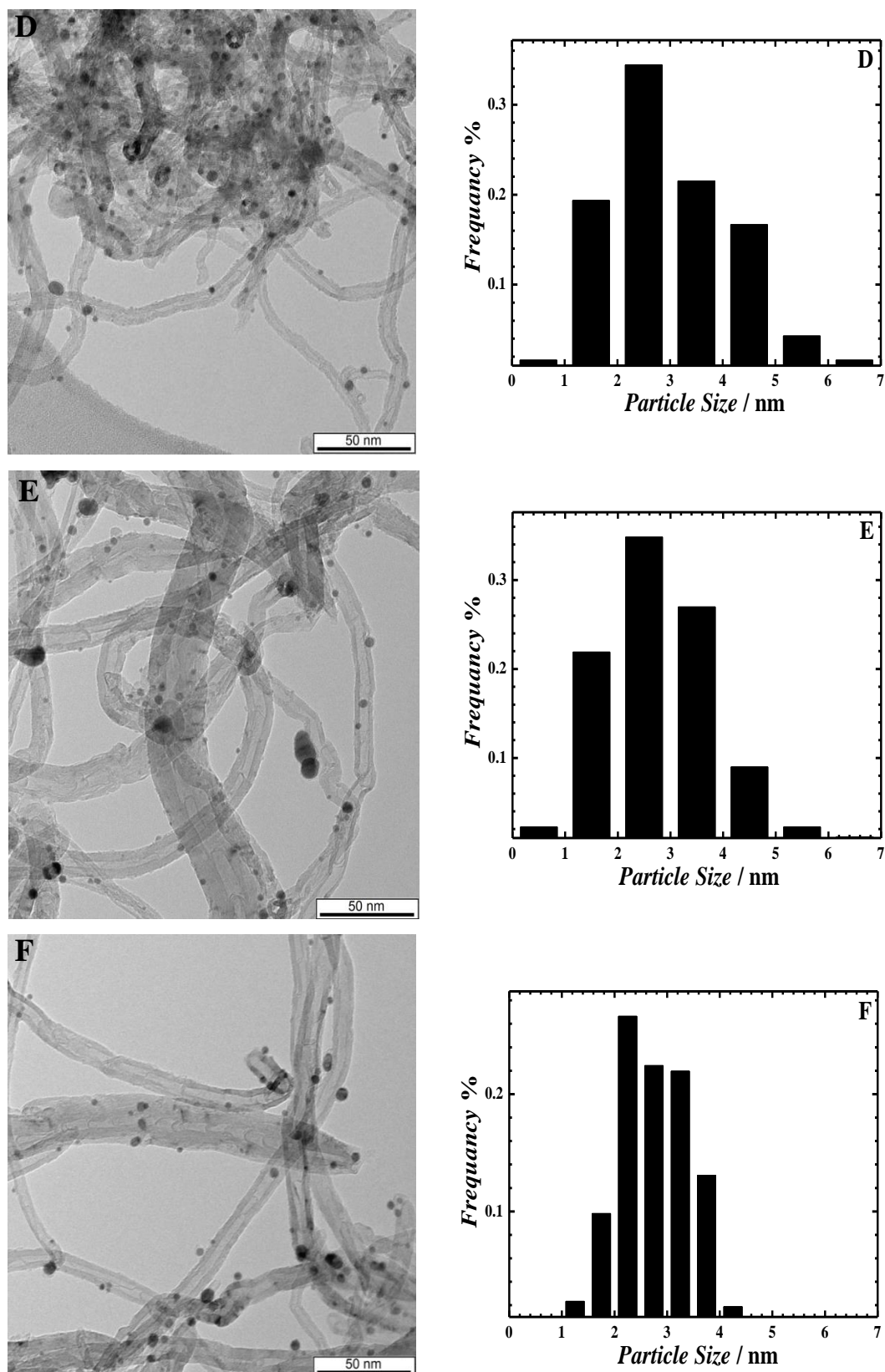


Figure 5.3: TEM image and the corresponding histogram of A) PtCu, B) PtCu_{15min}, C) PtCu_{1h}, D) PtCu_{2h}, E) PtCu_{4h}, and F) PtCu_{6h} catalysts.

The cyclic voltammograms (CVs) of the dealloyed catalysts are displayed in Figure 5.4A, resembling those of a pure platinum surface but with slight differences, (i.e. the H_{upd} stripping peaks are less pronounced). On the other hand, the initial CV of the alloy precursor displayed in Figure SI 5.1A shows no characteristic features for Pt but only an anodic stripping peak characteristic to the dissolution of pure unalloyed Cu. The latter would be consistent with Cu surface segregation in a Cu-rich Pt alloy [60]. The differences between the CV profiles of the dealloyed catalysts and the initial CV profile of the alloy precursor indicate that during dealloying copper is removed from the surface and a Pt layer terminates the catalyst particles after dealloying already after short dealloying times. However, the H_{upd} stripping charge of the dealloyed catalysts changed significantly as a function of dealloying time, indicating that significant changes in the catalyst particles occur with ongoing dealloying, which result in a strong decrease in surface area. Similar results are obtained from CO stripping Figure SI 5.1B and the electrochemical active surface areas (ECSA) of the alloy precursor and dealloyed catalysts from H_{upd} ($\text{ECSA}_{H_{\text{upd}}}$) and CO (ECSA_{CO}) are compared in Figure 5.4B. The values were recorded after 25 potential cycles (see section 5.2), and no major changes were observed in the CV profiles of the dealloyed catalysts upon cycling while the change in the CV profile of the alloy precursor after 25 CVs was severe Figure SI 5.1A. Voltammetric activation leaches out Cu atoms from the Cu-rich alloy surface as demonstrated by the disappearance of the peak at ca. 0.45 V and emerging H_{upd} peak, however an anodic peak at ca. 0.7 V vs. RHE characteristic to the Cu dissolution from a Pt-rich atomic environment still is visible after 25 cycles [65]. In general, the ECSA estimated from the H_{upd} and CO stripping behave similarly however, with higher values from CO stripping, a trend also observed in other publications [120]. It is difficult to estimate the $\text{ECSA}_{H_{\text{upd}}}$ of the PtCu alloy precursor and thus the value is not included in Figure 5.4B. The ECSA_{CO} of the chemically dealloyed catalyst achieved a significant increase by a factor of ca. 1.3 after 1 h acid treatment relative to the activated alloy precursor. Thereafter, the ECSA of the dealloyed catalysts decreases gradually with increasing the dealloying time to 2 h, 4 h and 6 h respectively. As a consequence of a collapse the Pt-rich skin structure, as illustrated in Figure 5.5 and demonstrated from decreasing the H_{upd} and CO stripping charge as the chemical dealloying time extended to more than 1 h.

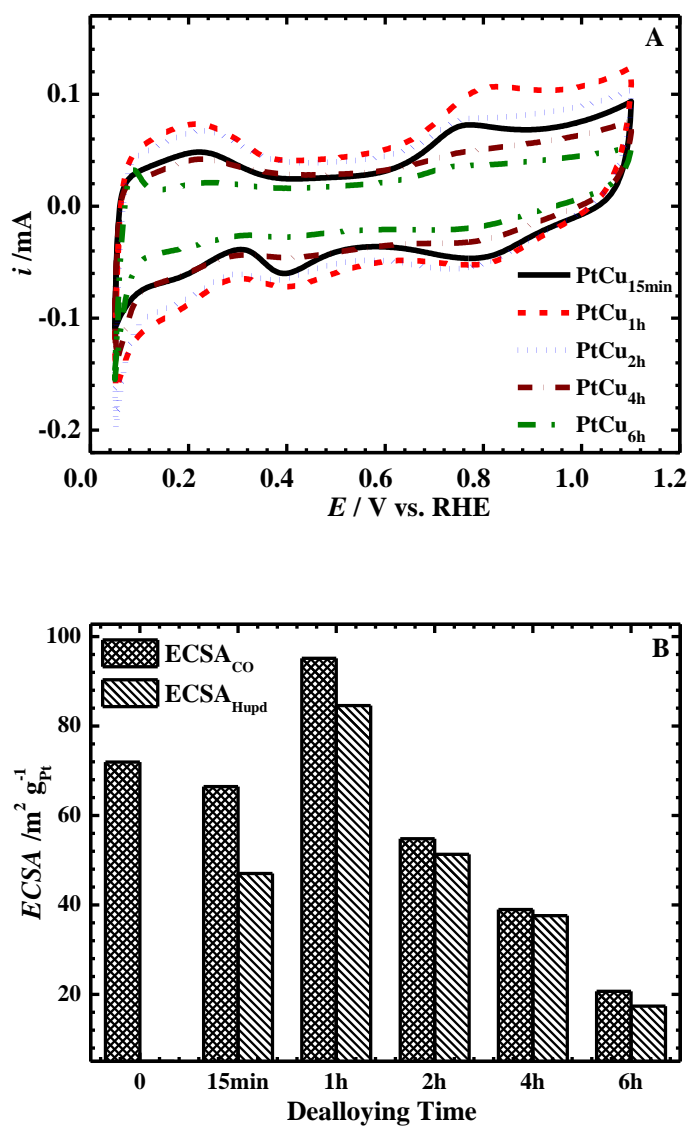


Figure 5.4: A) Cyclic voltammogram profiles of the dealloyed catalysts in N_2 -saturated 0.1 M HClO_4 at 100 mV s^{-1} scan rate, B) electrochemical active surface area estimated from the CO and H_{upd} stripping peak as a function in dealloying time.

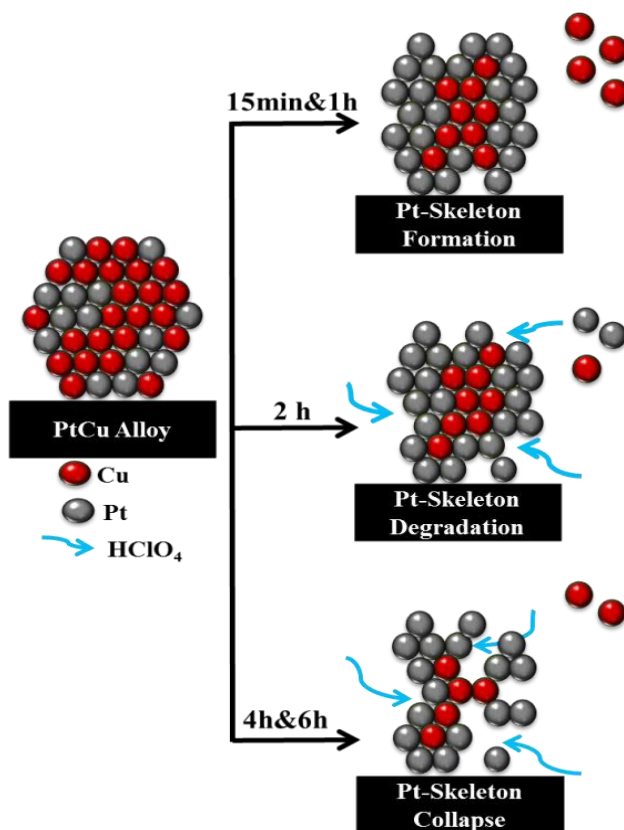


Figure 5.5: Schematic illustrates the formation and collapse of the Pt-rich skin alloy-core structure as a function in the dealloying time.

From the above experimental findings a model of catalyst structure and structural development with dealloying time can be derived as follows: after high temperature treatment under reductive atmosphere, a Cu-rich alloy forms. ICP-OES and XRD yielded similar compositions, suggesting a homogeneous structure; however XPS seems to point to a slight Pt surface enrichment. Dealloying very quickly removes Cu from the particles, and ICP-OES indicates that already after 15min a composition very close to the final one is achieved. Variations in the composition determined from Vegard's law (XRD) might point to changes within the catalyst with time however might also be due to experimental error in determination of peak positions. XPS clearly demonstrates Pt surface enrichment already after 15min dealloying, and electrochemical results indicate a Pt surface of the catalysts. It is important to point out that chemical leaching in our case affects the whole nanoparticle and not just the outer layers, as previously also reported [118], this and the fast dealloying might be due to the small particle size.

In this regard, the development of ECSA with dealloying time might shed some light on catalyst structure development. Initially the ECSA increases, which might be attributed to liberation of Pt surface sites from copper, but also to the formation of nanopores in the catalyst surface leading to a kind of structure [30]. With ongoing dealloying and electrochemical cycling, these nanopores penetrate into the bulk of the particle. At a certain point however, the structure collapses and smaller particles form, which might have a smoother surface again, explaining their lower ECSA. Figure 5.5 displays a suggested model of catalyst structure development.

Figure 5.6A displays the ORR polarization curves of the activated alloy precursor and the dealloyed catalysts obtained by sweeping the potential from 0.05 to 1.1 V vs. RHE with a rotating disk electrode (RDE) in O₂-saturated 0.1 M HClO₄ at rotation rate of 900 rpm and with 5 mV s⁻¹. The Koutecky-Levich plot (K-L, j⁻¹ vs. ω^{-1/2}) of the activated alloy precursor and the dealloyed catalysts at 0.4 V vs. RHE is shown in Figure 5.6B. Two factors are commonly used to qualify the activity of ORR electrocatalysts, namely, the onset potential (E_{onset}) and the half wave potential (E_{1/2}). Although from Butler-Volmer theory an onset potential does not exist at all (i.e., the current should increase as soon as the potential is shifted from the reversible one), it is commonly used as a semi-quantitative measure for activity. Generally, the more positive the onset potential and the half wave potential the more active the electrocatalyst is [121]. The ORR polarization curve of the PtCu alloy precursor has a ca. 30 and 50 mV vs. RHE more negative E_{onset} and E_{1/2} respectively when compared with the polarization curves of the dealloyed catalysts, which indicates that the dealloyed catalysts are more efficient for ORR than the alloy precursor. Moreover, the E_{onset} and the E_{1/2} of the dealloyed catalysts increases in the sequence: PtCu_{6h} < PtCu_{4h} < PtCu_{15min} < PtCu_{2h} ≤ PtCu_{1h}.

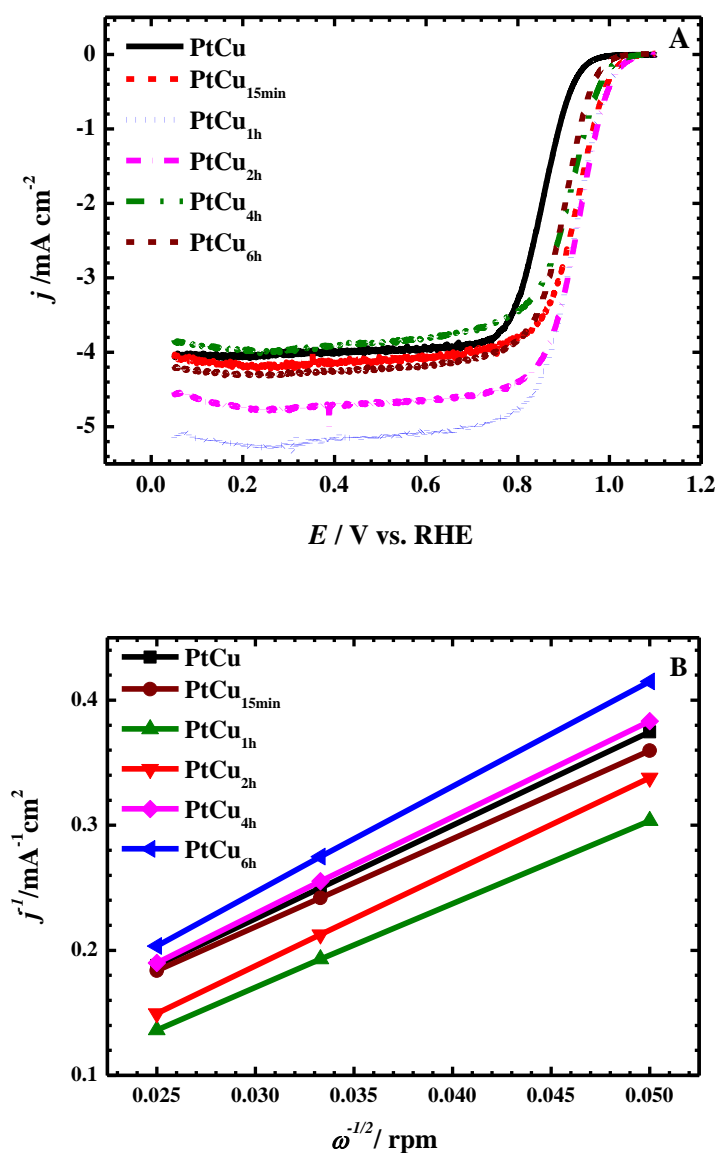


Figure 5.6: A) ORR polarization curves of the dealloyed catalysts compared to the alloy precursor (black solid line) performed in O₂-saturated 0.1 M HClO₄ at scan rate 5 mV s⁻¹ with a rotation rate of 900 rpm, B) Koutecky-Levich plot at 0.4 V vs. RHE.

Figure 5.7 illustrate the relation between the transferred electron number per oxygen molecule and the chemical dealloying time (**PtCu alloy precursor labelled as 0**). Solely, the ORR catalyzed by the dealloyed catalyst PtCu_{1h} proceeds through four electrons pathway as the ORR catalyzed by Pt catalysts, in accordance with the proposed model (see Figure 5.5), which postulates the formation of Pt-skeleton after 1 h chemical dealloying. Moreover, the overall electron transfer number was less than four (mixed two and four electron transfer pathway [15]) when the dealloying time was

either shorter or higher than 1 h in a sequence of: PtCu_{6h} < PtCu_{4h} < PtCu_{2h} < PtCu₁₅ which could be attributed to the changes occur on the catalysts surface as a function of dealloying time (see Figure 5.5).

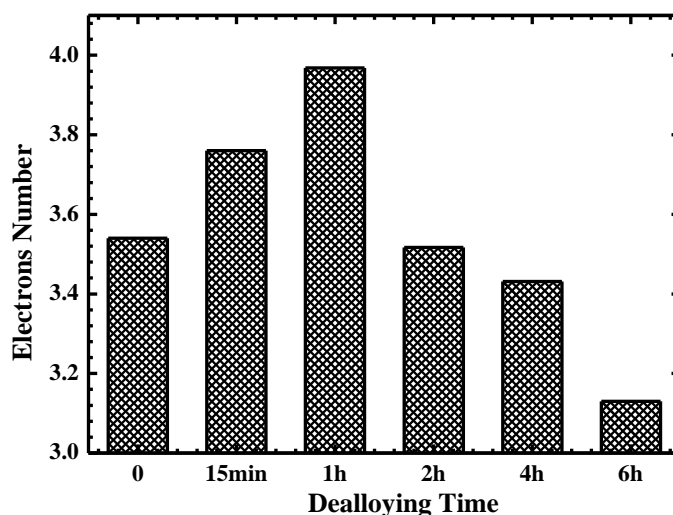


Figure 5.7: Number of electrons estimated from the K-L plot as a function in dealloying time.

For an accurate comparison of the catalysts, the wave half potential and the onset potential of the ORR polarization curve seems to be not accurate enough since their estimation is somehow arbitrary and $E_{1/2}$ is controlled by both the electrode kinetics of the catalysts and the O₂ diffusion process. Thus, for a better and accurate understanding of the role of the dealloying time on the ORR performance the mass and specific (i.e., surface related) activities of the dealloyed catalysts at 0.9 V vs. RHE were calculated by dividing the kinetic current estimated from Koutecky-Levich equation by the amount of the Pt or by the electrochemical surface area of Pt on the electrodes respectively [37]. The mass and specific activities of the alloy precursor and the dealloyed catalysts were plotted as a function of dealloying time in Figure 5.8A&B respectively. Obviously, the dealloyed catalysts display an impressive enhancement in the mass and specific activities which could be explained in terms of changes the surface electronic structure of the alloy as a consequence of the chemical dealloying process [24, 61]. The highest mass activity was observed for the PtCu_{1h} catalyst which was predictable and reasonable on the basis of the physical and electrochemical characterization, i.e. the high surface area. Indeed, the mass activity shows the same

trend as the surface area, with the exception of the precursor. On the other hand, the specific activity clearly increases with dealloying time. According to our model in Figure 5.5 shorter dealloying times lead to an open structure, whereas after longer dealloying the structure collapses and close, smooth structures form. It is known from literature that low-coordinated Pt atoms are less active for ORR due to stronger bonding of intermediates. Thus, with increasing dealloying time and the formation of a smooth Pt surface the activity increases up to impressively high 600–700 $\mu\text{A}/\text{cm}^2$. The enhanced activity compared to literature values obtained on Pt [122-124] is usually explained with strain effects in core-shell structures, and we have every reason to assume that the same mechanism is at work here too.

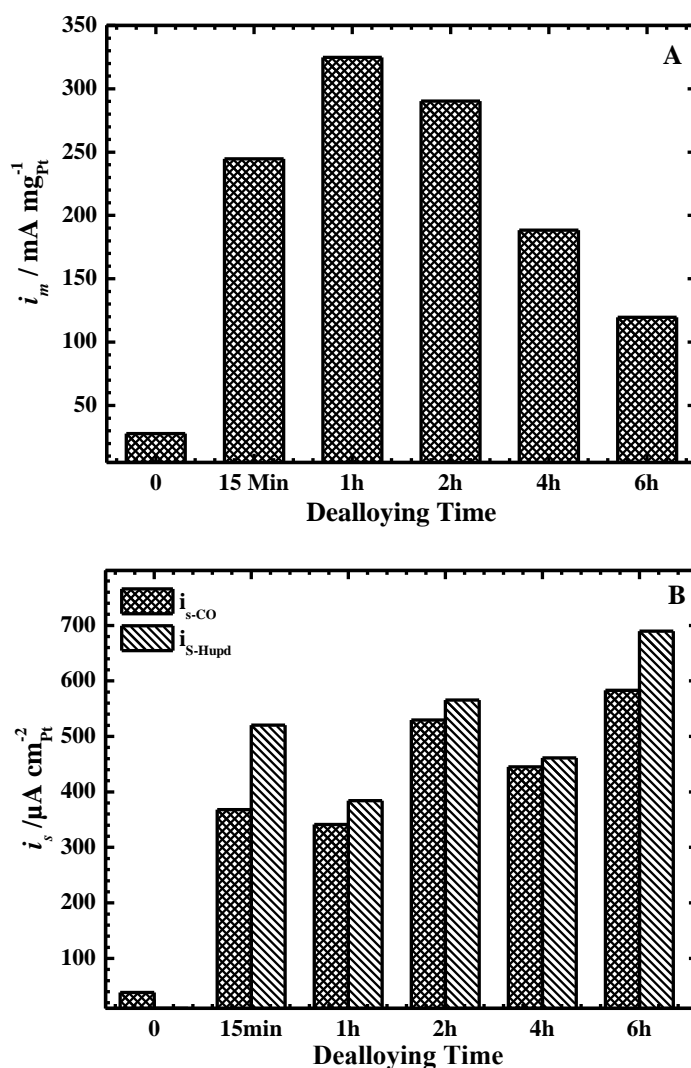


Figure 5.8: A) the mass activity (i_m) and B) the specific activity (i_s) of the dealloyed catalysts as a function in dealloying time, the activities were estimated at 0.9 V vs. RHE.

5.4 Conclusions

PtCu alloy catalysts with a Pt-rich shell were prepared via chemical dealloying of Cu-rich PtCu alloy nanoparticles in 1 M HClO₄. The influence of dealloying time was investigated. The CV profiles of the dealloyed catalysts exhibited characteristic feature of a Pt surface already after 15 min of dealloying but the H_{upd}/CO stripping peaks and their ORR activities were significantly changing with dealloying time. The results show that 1 h chemical dealloying in 1 M HClO₄ seems to lead to a skeleton-like structure which collapses during longer dealloying. While the mass specific activity shows a clear trend with surface area, the surface specific activities increase with dealloying time attributed to the higher activity of a smooth, skin-like Pt shell.

5.5 Supporting Information

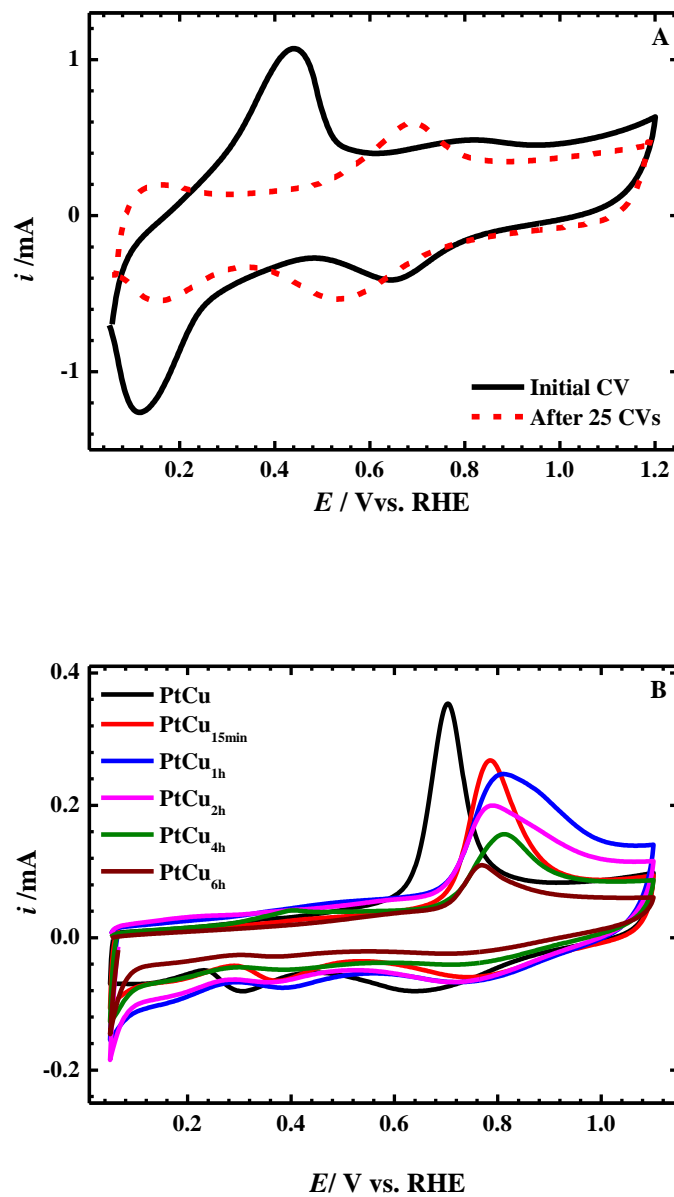


Figure SI 5.1: A) The initial CV profile of the PtCu alloy precursor and the voltammetrically activated one, B) CO stripping voltammogram of the activated PtCu alloy and the dealloyed catalysts.

6 Enhanced Oxygen Reduction Reaction Activity on Core-Shell Nanocatalysts Synthesized via Dealloying of Cu@Pt/CNTs Catalyst.

**The following chapter is part of a publication currently prepared for submission ^[b].*

6.1 Introduction

Referring to our earlier results in chapter 3 & 4 on the preparation of PtCu electrocatalysts supported on carbon nanotubes for ORR, it has become obvious that one or two reduction steps using the polyol method are not sufficient for metal loading optimization. This chapter provides an attempt to optimize the nominal loading of the Pt and Cu metals supported on the functionalized multiwall carbon nanotubes (O-CNTs). The Cu@Pt/CNTs catalyst has been prepared through a two-step synthesis approach (see section 2.2.4) in order to reduce the metal lost caused by surfactant addition, as earlier discussed in chapter 3& 4, and therefore enhance the catalytic activity of the prepared core-shell catalysts produced by electrochemical dealloying of the Cu@Pt/CNTs catalyst. The effect of alloying temperature of the catalysts on their structural features and properties has been studied and correlated with their catalytic activity towards oxygen reduction reaction.

6.2 Electrochemical Measurements Protocol

The electrochemical measurements were conducted in a one compartment three electrode electrochemical cell containing 0.1 M HClO₄ as electrolyte solution at room temperature. The working electrode was a catalyst coated glass carbon (GC) substrate with 4 mm diameter inserted into a Teflon tip. The reference electrode was a reversible hydrogen electrode (RHE), consisting of a Pt net immersed in 0.1 M HClO₄ and activated by hydrogen evolution prior to the measurements. A Pt mesh was used as counter electrode. The thin layer catalyst electrode was prepared as described earlier in section 2.3.2.1.

Prior to establish the catalytic activity, the electrochemical dealloying step of the alloyed catalysts the Cu@Pt_x, was performed in N₂-deaerated 0.1 M HClO₄ electrolyte with keeping N₂ atmosphere passing through the cell during the conduction of the

[b]"Enhanced Oxygen Reduction Reaction Activity on Core-Shell Nanocatalysts Synthesized via Dealloying of Cu@Pt/CNTs Catalyst.", Heba El-Deeb, Abu Bakr Ahmed Amine Nassr, Ilja Sinev, Wolfgang Grünert, Michael Bron, in preparation.

measurements. The electrochemical dealloying protocol was initiated by 3 CVs in a potential range between 0.05-1.2 V vs. RHE with 100 mV s^{-1} sweep rate to acquire the initial profiles for the Cu dissolution. Then the actual dealloying was carried out on the catalyst-coated electrode using 200 potential cycles with scan rate of 200 mV s^{-1} , throughout, more Cu atoms were leached out from the alloy precursors. Thereafter, the dealloying protocol concludes with 3 CV in a potential range between 0.05 and 1.1 V vs. RHE and scan rate of 100 mV s^{-1} and the last CV was used to estimate the electrochemical active surface area ($\text{ECSA}_{\text{Hupd}}$) of the catalysts. The pretreatment of the Pt/CNTs catalysts and the chemically dealloyed samples (see section 2.2.4 for catalyst synthesis) consists of 20 CVs in a potential range between 0.05 and 1.1 V vs. RHE at 100 mV s^{-1} in N_2 -deaerated 0.1 M HClO_4 electrolyte and the final CV was used to estimate the electrochemical surface area. The electrochemical active surface areas were also determined by carbon monoxide stripping (ECSA_{CO}) according to the procedure described in section 2.3.2.4.1. Subsequently, linear sweep voltammetry (LSV) measurements using an RDE were carried out to evaluate the catalytic activity and the kinetic parameters for the oxygen reduction reaction (ORR) in oxygen-saturated 0.1 M HClO_4 . The potential was swept positively from 0.05 to 1.1 V vs. RHE with a scan rate of 5 mV s^{-1} at different rotation speeds of 400, 900 and 1600 revolutions per minute (rpm). An O_2 atmosphere was kept passing over the surface of the solution during all the measurements. The ORR currents of the catalysts were corrected from the capacitive current by subtracting the background current of the sweeps measured in N_2 -saturated electrolyte from those measured in O_2 -saturated electrolyte. Moreover, the ORR current density was corrected for mass transport limitation to obtain the kinetic current density according to Koutecky-Levich equation (Equations 3.1). The mass and surface specific activities of the catalysts were established at 0.85 and 0.9 V vs. RHE and rotation rate of 900 rpm using Equations 4.1& 4.2.

6.3 Results and Discussion

6.3.1 Structural Characterization

The XRD diffraction patterns of the prepared catalysts were gathered in Figure 6.1 and organized in three sections for comparison. All XRD patterns of the catalysts display a broad diffraction peak at 2θ ca. 25° corresponding to the diffraction at the graphene layers of CNTs beside three main peaks characteristic to the 111, 002

and 022 planes of Pt with the disordered face centered cubic structure (fcc). The bottom section in Figure 6.1 compares the diffraction patterns of the pure Pt/CNTs catalysts. Noticeably, the diffraction peaks of the Pt/CNTs_{HT} are found at slightly higher 2θ values compared to those of Pt/CNTs, where the former are identical to the diffraction peak of Pt/C (E-TEK) (see chapter 4).

The XRD diffraction patterns in the middle section visualized the influence of the annealing temperature on the structure Cu@Pt/CNTs catalyst. There are three features of interest in these patterns. First, the diffraction peaks of the annealed catalysts (Cu@Pt_x) were located at a 2θ higher than that of the Pt catalysts and the peaks became sharper and taller as the annealing temperature is increased from 600 °C to 1000 °C (i.e. increase the crystallite size, as evident from the reduction in the peak full width half maximum (FWHM)). Shifting the fundamental peaks of the alloyed catalysts to a higher 2θ with decreasing the inter planer distance and the lattice parameter of the unit cell indicate the alloy formation between Pt and Cu by incorporation of Cu into the unit cell of Pt. The second feature is the extra diffraction peaks observed in the Cu@Pt₆₀₀ and Cu@Pt₈₀₀ XRD pattern at $2\theta = 43^\circ, 51^\circ$ and 74° (marked with •) and corresponding to the planes 111, 002 and 022 of the pure Cu respectively. These extra peaks indicate that the temperatures of 600 °C and 800 °C are insufficient to achieve well-alloyed catalysts. The third feature of interest is the absence of the unalloyed copper diffraction peaks from the XRD pattern of the Cu@Pt₁₀₀₀ catalyst and emergence instead of four diffraction peaks at $2\theta = 24.1^\circ, 34.4^\circ, 55.7^\circ$ and 61.7° (marked with *) characteristic to the PtCu superlattice planes [125] (i.e. well-alloyed catalyst). The chemical dealloying of the Cu@Pt₁₀₀₀ catalyst for 1h and 4h in 1M HClO₄ gives rise to a broader diffraction peaks situated at diffraction angles between those of the Cu@Pt₁₀₀₀ catalyst and those of the pure Pt catalysts, beside disappearance of the diffraction peaks corresponding to the ordered intermetallic structure as presented in the upper section in Figure 6.1. Leaching out the Cu atoms from the catalyst surface during the acid treatment cause a partial re-expansion in the Pt lattice, since the Pt lattice still suffers from a compressive strain as demonstrated from the lattice constant values listed in Table 6.1. The Pt:Cu atomic ratio of the catalysts was established from the XRD patterns using Vegard's law (Equation 2.1), and ICP-OES analysis. However, the elemental surface composition was measured by XPS, see Table 6.2. The data suggest that the nanostructure of the Cu@Pt₁₀₀₀ alloy had

transformed upon chemical dealloying from a Cu-rich alloy to a Pt-rich alloy. Moreover, the electrochemical dealloyed Cu@Pt₆₀₀₋₁₀₀₀ catalysts also show a Pt surface enrichment as established from the XPS analysis Table 6.2.

Table 6.1: Average particle size established from TEM and XRD parameters.

Catalyst	Particle Size/nm ^[a]	Crystallite size/ nm ^[b]	2 θ ₁₁₁	d Å ^[c]	a _{alloy} Å ^[d]
Pt/CNTs	2.76	3.11	39.38	2.28	3.959
Pt/CNTs _{HT}	2.83	3.76	39.62	2.27	3.936
Cu@Pt ₆₀₀	3.53	4.57	40.79	2.21	3.828
Cu@Pt ₈₀₀	5.81	6.31	42.16	2.14	3.708
Cu@Pt ₁₀₀₀	12.52	17.70	42.58	2.12	3.674
Cu@Pt _{1h}	11.54	5.31	41.19	2.19	3.792
Cu@Pt _{4h}	10.57	7.03	40.69	2.21	3.837

[a]: the mean particle size of ca. 200 nanoparticles measured from TEM image, [b] crystallite size established from the FWHM, [c] the interplaner distance established from Bragg's law ($\lambda=2\sin\theta$), [d] lattice parameter according to the 111 peak ($a = d\sqrt{h^2 + k^2 + l^2}$).

The thermogravimetric analysis of the pure Pt systems displayed in Figure 6.2A show that the surface of the as-prepared Pt/CNTs still covered by PVP traces even after catalyst washing. The microwave heating profiles displayed in Figure 6.2B show that the temperature of the reaction mixture during the reduction step of the Pt precursor is higher than the melting point of the PVP molecules (ca. 150°C). In consequence, the PVP molecules were gradually melted during the heating process with possibility of forming an adhesive layer over the Pt nanoparticles surface. Apparently, the heat treatment process of the Pt/CNTs catalyst is an essential step for accomplishing the removal of PVP.

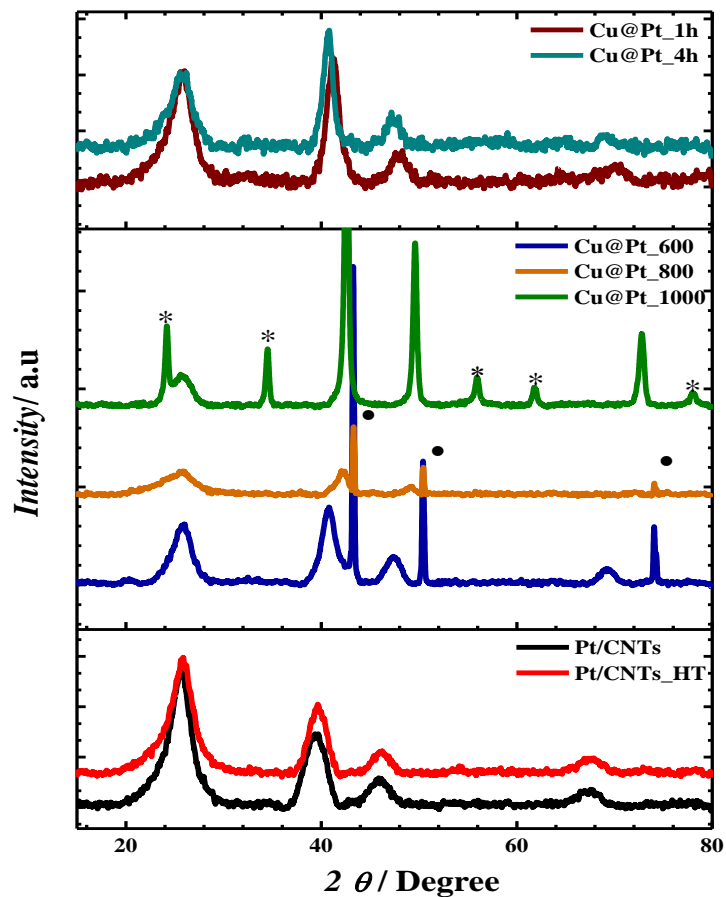
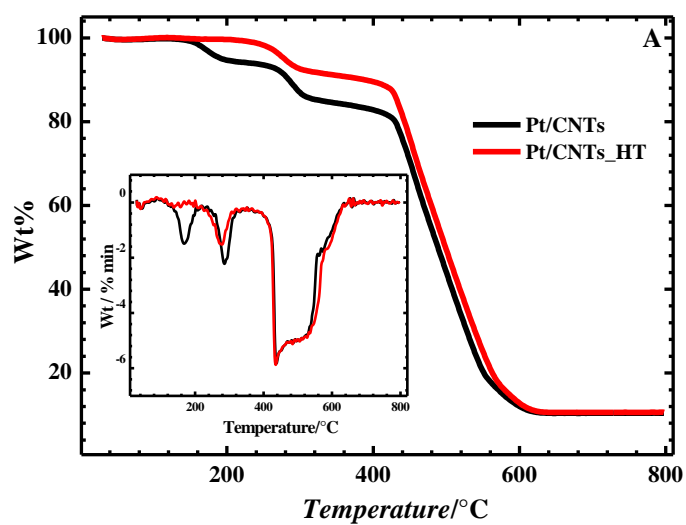


Figure 6.1: XRD patterns of the as-prepared catalysts.



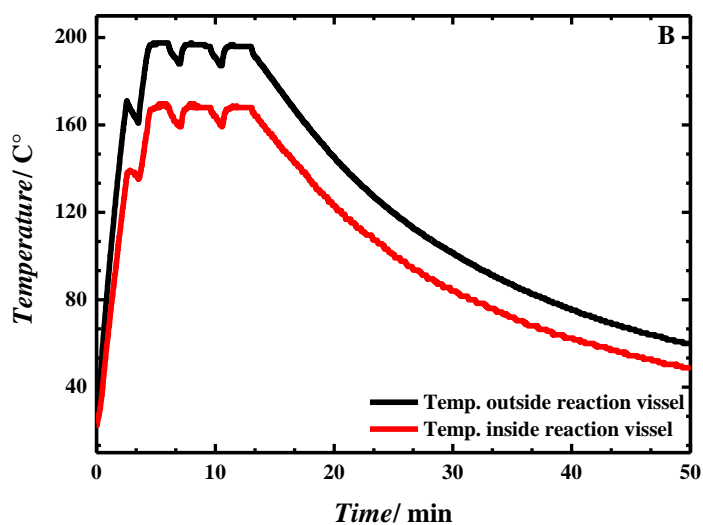


Figure 6.2: A) TGA curves of the as-prepared and heat treated Pt/CNTs catalysts; inset: DTG curves, B) Microwave heating profile of the Pt-PVP/EG mixture.

The metal loading of the as-annealed catalysts, Cu@Pt_x, was assessed by the thermogravimetric analysis (TGA) as shown in Figure 6.3 while the data was listed in Table 6.2 with the metal contents established from ICP-OES analysis. In a typical synthesis method the nominal metal loading of the as-prepared Cu@Pt catalyst with was calculated to be ca. 21%. However, the total metal loading of the annealed catalysts as specified from TGA and ICP-OES analysis exhibit increase in the metal over the nominal ratio as the annealing temperate increases from 600 °C to 1000 °C, which could be assigned to removing almost all the oxygenated groups attached to the MWCNTs surface during the annealing process and decomposition/volatilization of the carbon nanotubes [126]. Moreover, The TGA analysis of the chemically dealloyed catalysts Cu@Pt_{1h} and Cu@Pt_{4h} in 1 M HClO₄ reveals decreasing in the metal loading from 24.5 wt.% to 14.5 wt.% when compared with the counterpart catalyst, Cu@Pt₁₀₀₀. Such drastic decrease in the metal content is attributed to the severe drop in the Cu content (i.e. Cu dissolution) as demonstrated from ICP-OES data in Table 6.2, while the Pt wt.% exhibits a slight increase. Extending the chemical dealloying time from 1 h to 4 h decreases the Pt and Cu loading which could be attributed to exfoliation of the passivation layer, i.e. Pt-skeleton formed during the chemical dealloying process consequently, diffusing the electrolyte to the under layers causing Cu dissolution (with longer dealloying time the Pt-skeleton will collapse) [127].

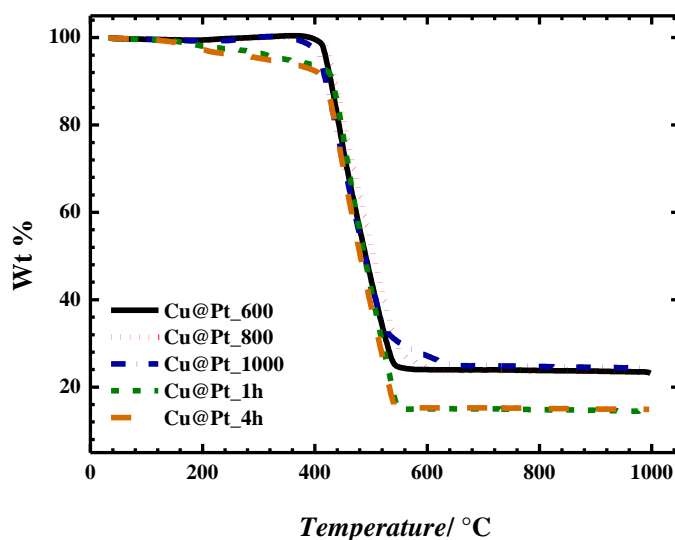


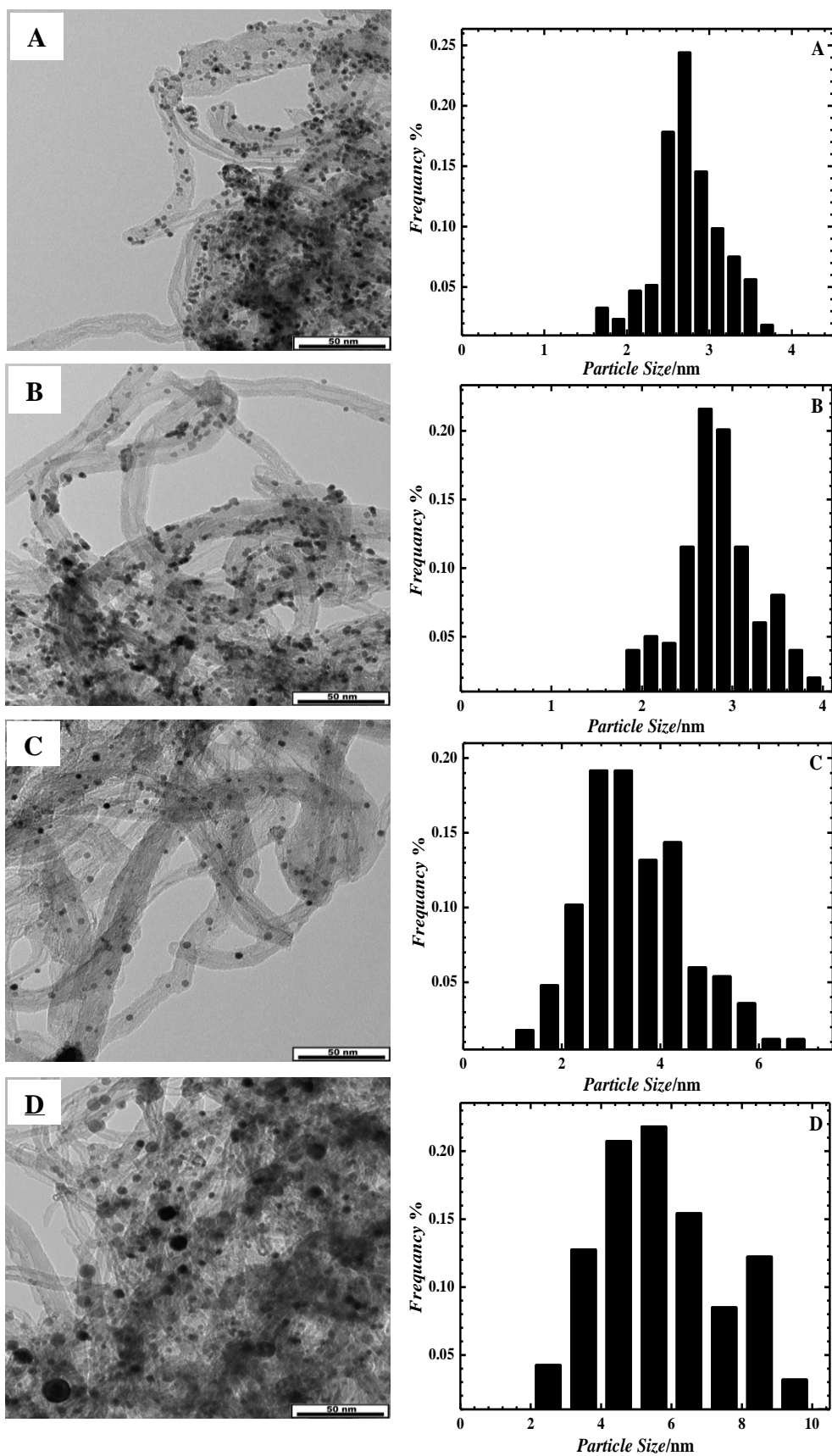
Figure 6.3: TGA curves of the as-annealed Cu@Pt_x catalysts.

Table 6.2: Total metal loading in wt.% estimated from the ICP-OES and TGA analysis, and the Pt:Cu atomic ratio determined from the XRD, ICP-OES and XPS for catalysts.

Catalyst	Pt	Cu	Total ^[a]	Total ^[b]	Pt:Cu			
	wt. %		wt. %		at. % ^[c]	at. % ^[a]	at. % ^[d]	at. % ^[e]
Pt/CNTs	10.6	—	10.6	10.6	—	—	—	—
Pt/CNTs _{HT}	10.5	—	10.5	10.5	—	—	—	—
Cu@Pt ₆₀₀	7.7	12.1	19.8	23.9	69:31	17:83	58:41	80:20
Cu@Pt ₈₀₀	10.1	13	23.2	23.9	30:70	20:80	43:57	70:30
Cu@Pt ₁₀₀₀	10.2	17.6	27.8	24.5	19:81	16:84	42:58	79:21
Cu@Pt _{1h}	13.3	2.7	16.05	14.5	57:43	61:39	—	57:43
Cu@Pt _{4h}	11.4	1.6	13.03	14.5	72:28	70:30	—	72:28

[a] determined from ICP, [b] as determined from TGA, [c] as determined from XRD, [d] as determined from XPS for the alloyed catalysts, and [e] as determined from XPS for the dealloyed catalysts

Figure 6.4A-G shows the TEM images of the synthesised catalysts and the corresponding particle size distribution histograms. Generally, the nanoparticles of the synthesised catalysts are well-dispersed on the supporting materials and have a narrow particle size distribution. The mean particle sizes of the catalysts were established from randomly counting ca. 200 particles which are in a good agreement with the crystalline sizes estimated from XRD analysis as shown in Table 6.1. It is clear from the TEM images and the corresponding histograms shown in Figure 6.4A-B that the as-prepared Pt/CNTs nanoparticles nearly retained their mean particle size after the heat treatment in open-air at 185°C for 5 h for PVP traces removal. However, the change in the mean particle size of the annealed catalysts, Cu@Pt_x, was severe ranging from 3.53 nm to 12.52 nm as the annealing temperature increased from 600°C to 1000°C, as presented in Figure 6.4C-E. The TEM images of the chemically dealloyed catalysts, Cu@Pt_{1h} and Cu@Pt_{4h} are shown in Figure 6.4F-G. It's clear from the TEM images that the formation of core-shell structure after 1 h chemical dealloying with mean particle size of 11.54 nm can be observed whilst prolonged dealloying, i.e. 4 h, resulting in a highly porous structure with mean particle size of 10.57 nm. Further, the HRTEM (Figure SI 6.1) demonstrate the formation of a core-shell structure and it can be also detected that the Cu@Pt particles with small size (10-15 nm) tend to form a core shell structure while the Cu@Pt particles with large particles than 15 nm tend to form a highly nanoporous structure [128, 61]. Even more investigation by EDX-STEM analysis (Figure SI 6.2) confirmed the formation of a core-shell structure with a pure Pt shell and an alloyed core with composition of Pt₂₅Cu₇₅. It has been suggested that during the chemical dealloying of Pt-based alloy the most active metal (i.e. Cu in this case) is selectively dissolved from the alloy surface while the less active metal (i.e. Pt) tends to diffused outward to passivate the surface and locally blocked further dissolution. However, this passivation layer cannot stand for ever in front of the harsh corrosion condition and start to exfoliate allowing dissolution to proceeds through considerable depth causing a three dimensional nanoporous structure (the stability of surface atoms is highly dependent on their coordination number, i.e. low coordination atoms will be more sensitive to dissolution) [62, 66].



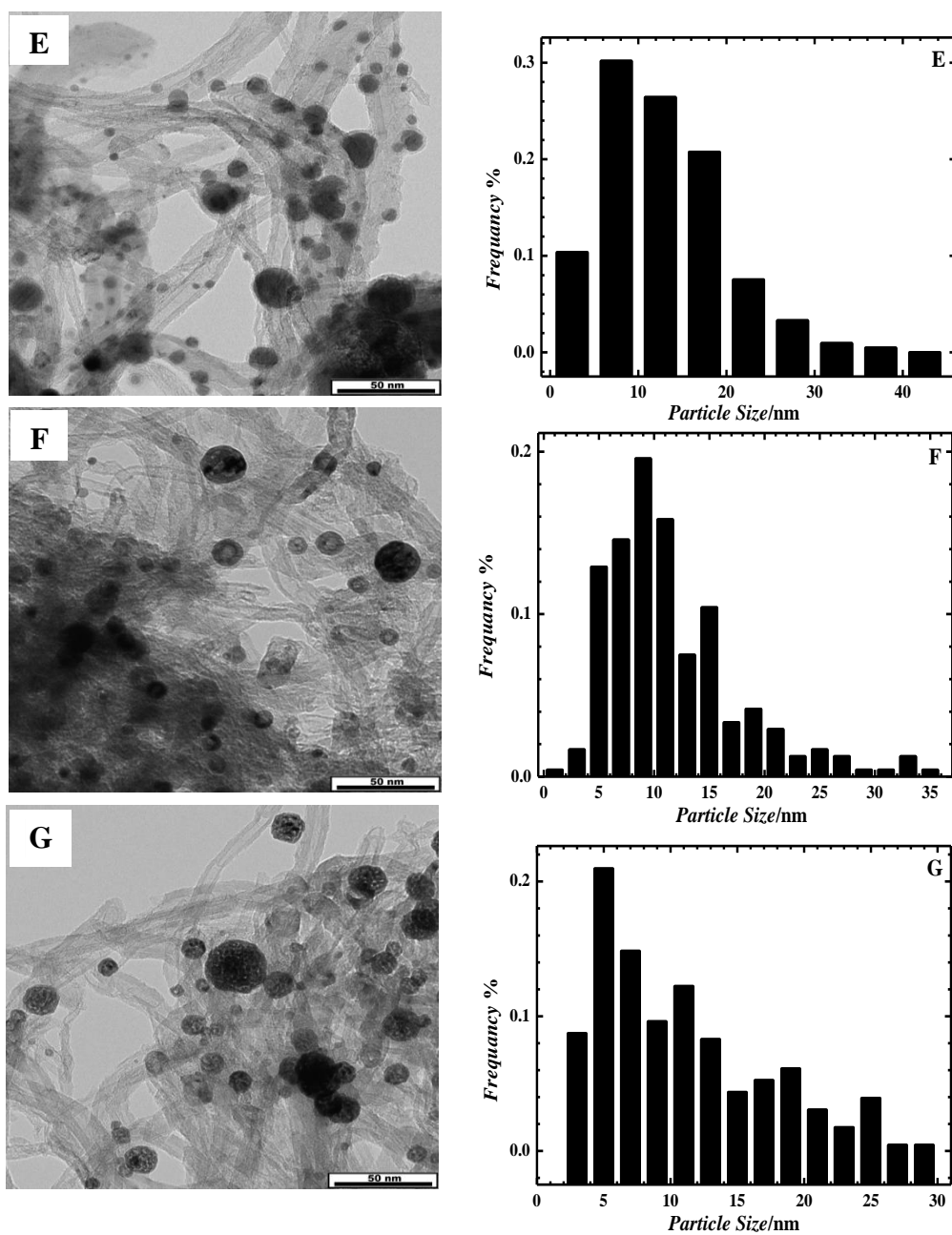


Figure 6.4: TEM images of the catalysts: **A)** Pt/CNTs, **B)** Pt/CNTs_{HT}, **C)** Cu@Pt₆₀₀, **D)** Cu@Pt₈₀₀, **E)** Cu@Pt₁₀₀₀, **F)** Cu@Pt_{1h}, **G)** Cu@Pt_{4h}.

6.3.2 Electrochemical Characterization

Figure 6.5 shows the first cyclic voltammograms (CVs) of the catalysts alloyed at various elevated temperatures, Cu@Pt_600-1000, performed in N₂-saturated 0.1 M HClO₄ solution with sweep rate of 100 mV s⁻¹. The first CVs do not display any distinct features of a Pt containing surface, i.e. the hydrogen adsorption desorption peaks (H_{UPD}) in the relevant potential range of 0.05 V to 0.3 V vs. RHE, the double layer region and the Pt oxide formation peak and its counterpart (i.e. reduction peak). Alternatively, a distinct broad faradic peak in a potential range between 0.3 V to 0.85 V vs. RHE was recorded consistent with Cu dissolution from Cu rich alloy surface. Furthermore, increasing the annealing temperature from 600°C, 800 °C to 1000°C leads to a gradual retraction in the Cu stripping peak height. Such retraction points to the reduction in the amount of the pure unalloyed Cu i.e. enhancing the alloying degree as described earlier in the XRD section. In contrast, the first CVs of the Pt/CNTs, Pt/CNTs_HT, Cu@Pt_1h, and Cu@Pt_4h catalysts didn't exhibit any characteristic feature of a Cu-segregated surface.

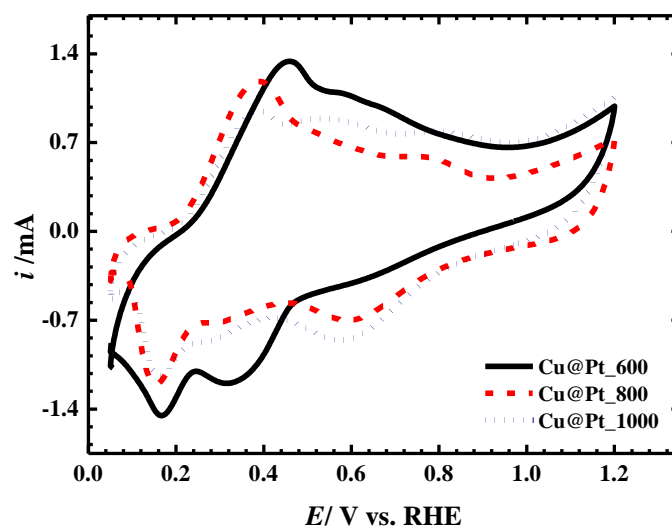
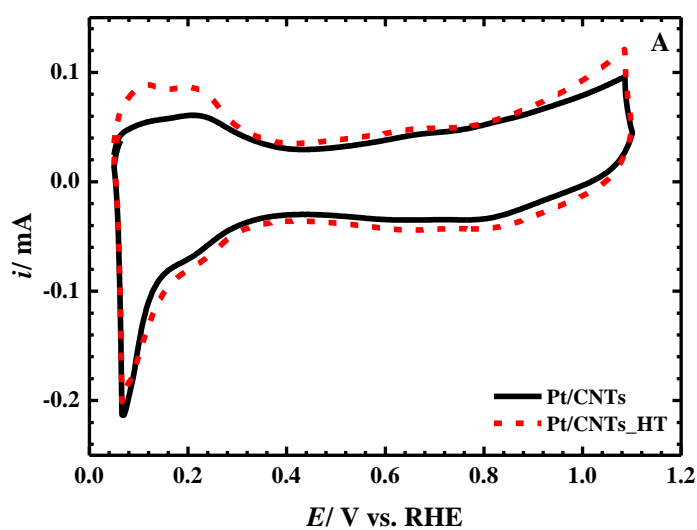


Figure 6.5: Initial cyclic voltammograms of the alloyed catalysts Cu@Pt_600-1000.

Figure 6.6A-C illustrates the definitive cyclic voltammograms of the different catalysts under investigation in N_2 -saturated 0.1M $HClO_4$ solution with scan rate of 100 mV s^{-1} . The CVs for the Cu@Pt_x were recorded after the electrochemical dealloying step (200 CVs at 200 mVs^{-1}) while the final CVs for the Pt/CNTs catalysts and chemically dealloyed catalysts were recorded after the electrochemical cleaning/activation of the catalysts electrode in N_2 -saturated 0.1M $HClO_4$ solution for 20 consecutive CVs with scan rate of 100 mV s^{-1} . Basically, the final CVs of the entire catalysts behave like pure Pt systems nevertheless with some remarks. First, the CV profiles of the heat treated Pt catalyst, Pt/CNTs_HT, display a higher H_{upd} than the as-prepared Pt/CNTs catalyst as shown in Figure 6.6A, consequently a ca. 1.25 times higher $ECSA_{H_{upd}}$ (Table 6.3). This difference in the $ECSA_{H_{upd}}$ could be assigned to blocking of ca. 25.45% of the adsorption active sites of the Pt/CNTs catalyst by the unremoved PVP traces, as aforementioned. Chung et al. [129] reported that the hydrogen underpotential deposition region of a surfactant treated commercial available Pt/C catalyst displays a significant decrease in the ECSA compared to the untreated Pt/C catalyst; they claim that the surfactant effectively adsorb on the Pt active sites and block about 70% of the ECSA. Secondly, the final cyclic voltammograms of the annealed catalysts, Cu@Pt_600-1000, after 200 dealloying cycles exhibit a dramatic transformation from Cu-rich alloy surfaces to a Pt-rich alloy surfaces as shown in Figure 6.6B compared to Figure SI 6.3 (Figure SI 6.3 shows the gradual fading of the Cu stripping peaks). Generally, electrochemical active surface areas of the catalysts were evaluated from the charge associated with the H_{upd} stripping (Q_H), namely $ECSA_{H_{upd}}$. To calculate the $ECSA_{H_{upd}}$, Q_H was normalized using the surface area specific charge of an ideal one-electron transfer for hydrogen adsorption on Pt surface (i.e. $210\text{ }\mu\text{C.cm}^{-2}$), see section 2.3.2.4.2. The $ECSA_{H_{upd}}$ for all catalysts were calculated and depicted in Table 6.3. Noticeable, the adsorbed hydrogen coverages, H_{upd} , of the electrochemically dealloyed catalysts dramatically decrease as the annealing temperature increases from $600\text{ }^\circ\text{C}$ to $1000\text{ }^\circ\text{C}$. This decrease in the H_{UPD} concomitant with reducing the $ECSA_{H_{upd}}$ of the Cu@Pt_800 and Cu@Pt_1000 catalysts by 61.9% and 64.9% respectively relative to Cu@Pt_600 catalyst, i.e. Cu@Pt_600 is expected to provide a larger reactive area and more active sites for oxygen reduction. The drastic decrease in the electrochemical surface area of the annealed catalysts at 800°C and $1000\text{ }^\circ\text{C}$ could be attributed to increasing the mean particle size of the catalysts (i.e. reduction the ECSA) resulting from the high temperatures at which these catalysts were prepared

as evidenced from the appearance of particles with large size in TEM analysis (Figure 6.4D, E) for the catalysts annealed at higher temperature. Finally, some remarks concerning the CVs feature of the chemically dealloyed catalysts shown in Figure 6.6C. The catalyst Cu@Pt_4h shows a ca. 1.5 times higher ECSA_{Hupd}, than that displayed by the Cu@Pt_1h; although, the former has a larger mean particle size and higher Pt content. Such ECSA enhancement could be attributed to the formation of a three-dimensional nanoporous structure [66] resulting from extending the chemical dealloying process to longer time (4 h), as aforementioned in the TEM discussion part. Furthermore, a positive shift of ca. 95 mV vs. RHE in the peak potential of the oxide reduction peak of the Cu@Pt_4h catalyst compared with the Cu@Pt_1h catalyst and the other catalysts can be observed. This shift indicates that the Cu@Pt_4h catalyst is more efficient in hindering the chemisorption of the oxygenated species on the active sites at high potentials.



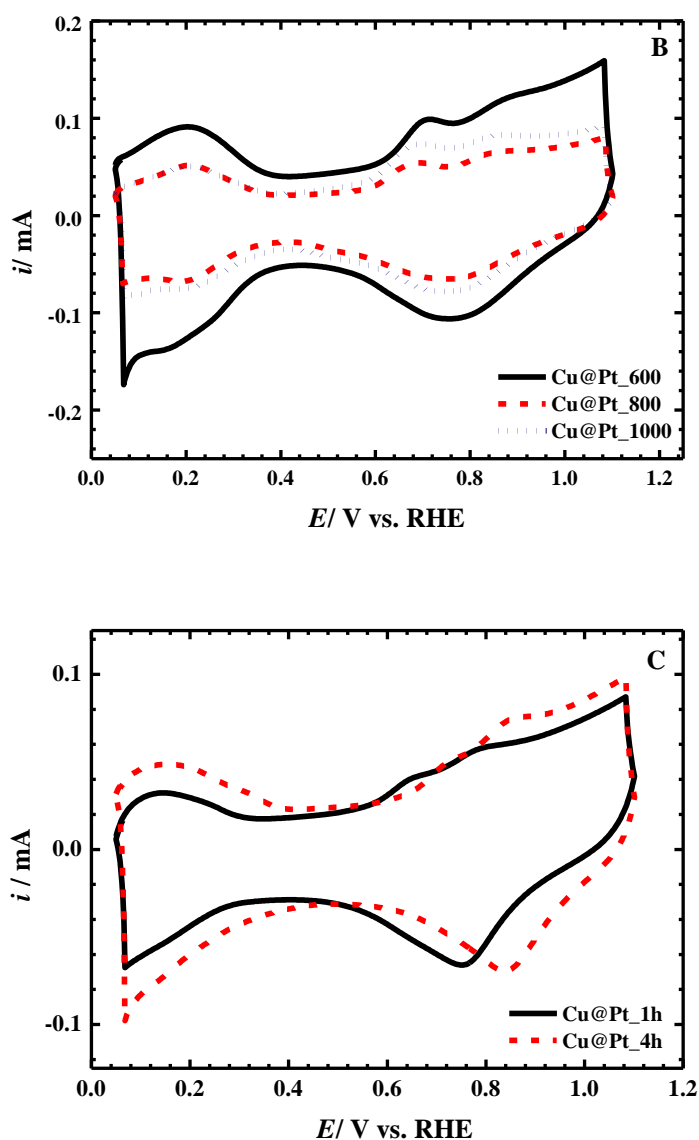


Figure 6.6: Cyclic voltammograms of: **A)** Pt/CNTs catalyst, **B)** the electrochemical dealloyed Cu@Pt_x catalysts and **C)** chemical dealloyed Cu@Pt₁₀₀₀ catalysts (in N₂-saturated 0.1 M HClO₄, 100 mV s⁻¹ scan rate).

It has been published in earlier reports [127, 120] that the electrochemical surface area of the Pt-based catalysts should be confirmed using CO stripping charge to avoid the underestimation of the ECSA owing to the possible suppression of H_{upd} adsorption, i.e. overestimation of the specific activity. Figure 6.7 summarized the representative CO stripping voltammograms for all catalysts under investigation. Apparently, prior to the electro-oxidation of the adsorbed CO monolayer from the catalyst surface the H_{UPD} was completely suppressed as result of blocking the active

sites for H_{upd} by CO molecules, while after CO electro-oxidation the peak associated with H_{UPD} emerged again. Furthermore, the onset potential of CO oxidation on the Cu@Pt_x catalysts surface irrespective they were chemically or electrochemically dealloyed was 60 to 180 mV lower than that on the pure Pt catalysts. The oxidation of the adsorbed CO proceeds at lower potentials on the dealloyed surface, this negative shift owes to the weaker interaction between the Pt surface atoms with the CO due to the modified electronic properties. However, the contribution of the geometrical effect (size dependent property) should not be excluded since the electronic and geometrical effects of the nanostructures are always interrelated to each other. A pronounced dependence was noticed between increasing the mean particle size and shifting the CO stripping peak potential negatively (see Table 6.1 for the mean particle size); this size dependence of CO monolayer electro-oxidation was also observed in previous investigations [130, 131]. The CO-based electrochemical active surface areas (ECSA_{CO}) were listed in Table 6.3. The most important finding is that dealloyed catalysts found to exhibit over 30% reduction in the $\text{ECSA}_{\text{H}_{\text{upd}}}$ relative to ECSA_{CO} ; on the other hand, no discrepancy has been recorded between the electrochemical active surface area estimated from the H_{upd} and CO stripping for the Pt/CNTs and Pt/CNTs_{HT} catalysts. Vliet et al. [132] and Wang et al. [133] demonstrated that the surface coverage of H_{UPD} on Pt-skin surface is about half of that found on pure Pt (111), whilst the surface coverage of a saturated CO monolayer is similar on both surfaces. Obviously the adsorption of H_{upd} on Pt surface layer formed after dissolution of the 3d element is greatly affected (i.e. suppressed adsorption of H_{upd}) [30, 134] due to the altered electronic properties; however, the CO adsorption is not affected due to the strong Pt-CO interaction [31]. Moreover, Vliet and Wang exploited this discrepancy in the ECSA obtained from H_{upd} vs. CO to proof the formation of Pt-skin surface layer over Pt-bimetallic systems. They reported that the ratio between the surface charges $Q_{\text{CO}}/2Q_{\text{H}}$ is nearly identical and close to unity in case of pure Pt systems (the H_{upd} charge was doubled in the ratio calculation ($Q_{\text{CO}}/2Q_{\text{H}}$) because CO electro-oxidation reaction is a two-electron process), while the $Q_{\text{CO}}/2Q_{\text{H}}$ ratio obtained for Pt-skin surfaces always greater than unity (i.e. $Q_{\text{CO}}/2Q_{\text{H}} > 1$ is indication of Pt-skin formation) [132, 133]. Thus, based on the afore mentioned argument and the results from CV and CO stripping we can conclude that a core-shell structure is formed after surface dealloying of Cu@Pt_x catalysts.

Table 6.3: Q_H values, Q_{CO} values, the ECSA obtained from H_{upd} and CO stripping, and the $Q_{CO}/2Q_H$ ratio of the Pt/CNTs, Pt/CNTs_{HT} and the electro/chemical dealloyed catalysts, the charges were normalized to the electrode geometric area.

Electro(Chemical) dealloyed catalysts	Q_H $\mu\text{C}\cdot\text{cm}^{-2}$	Q_{CO} $\mu\text{C}\cdot\text{cm}^{-2}$	$\text{ECSA}_{H_{upd}}$ $\text{m}^2/\text{g}_{\text{Pt}}$	ECSA_{CO} $\text{m}^2/\text{g}_{\text{Pt}}$	$Q_{CO}/2Q_H$
Pt/CNTs	86.88	185.36	68.80	73.40	1.06
Pt/CNTs _{HT}	112.80	237.6	88.51	93.22	1.05
Cu@Pt ₆₀₀	107.44	307.12	57.78	82.59	1.42
Cu@Pt ₈₀₀	64.24	168.88	26.45	34.77	1.31
Cu@Pt ₁₀₀₀	59.60	161.76	24.35	33.05	1.35
Cu@Pt _{1h}	36.80	107.60	23.04	33.70	1.46
Cu@Pt _{4h}	51.36	140.01	37.45	51.12	1.36

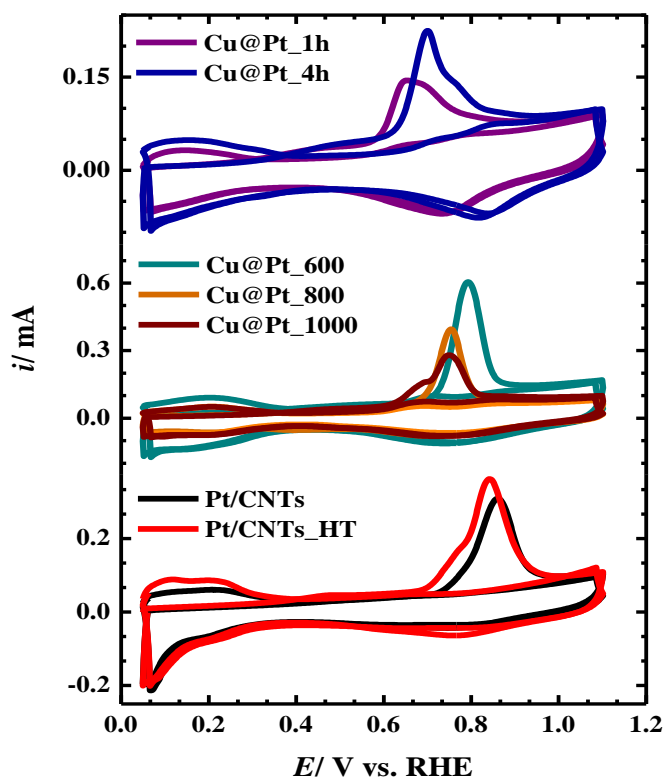


Figure 6.7: Representative CO stripping voltammogram of the Pt catalysts and the electrochemically/chemically dealloyed Cu@Pt_x catalysts in N_2 -saturated 0.1 M HClO_4 and sweep rate of 20 mV s^{-1} .

To study the catalytic activity, the ORR polarization curves for the catalysts were recorded using LSV combined with RDE technique at different rotation speeds in O₂-saturated 0.1M HClO₄ electrolyte between 0.05 to 1.1 V vs. RHE with a scan rate of 5 mV s⁻¹. The ORR polarization curves of the catalysts Pt/CNTs_HT, electrochemically dealloyed Cu@Pt_600 and chemically dealloyed Cu@Pt_4h are shown in Figure 6.8. The ORR polarization curve for the other catalysts at different rotation speeds are shown in the supporting information (Figure SI 6.4). As a general trend, the ORR polarization curves of the catalysts shows three distinct potential regimes, namely by sweeping positively, the well-defined diffusion-limiting regime (ca. E<0.75), the mixed kinetic-diffusion control regime, and the kinetic control regime (ca. E > 1.0). For determination of the kinetics of ORR, such as the number of electrons involved in ORR and hence the pathway of the ORR mechanism on the catalysts under investigation, the ORR curves at different rotation speeds were analyzed using the Koutecky–Levich equation (Equation 3.1).

According to the Koutecky–Levich equation, the average number of electrons transferred per O₂ molecule could be established from the slope of the straight-line obtained from a plot of j^{-1} vs. $\omega^{-1/2}$ (K-L plot, slope = 1/B). The K-L plots for the catalysts under investigation at a potential of 0.6 V vs. RHE are presented in Figure 6.9 A. The calculated average numbers of electron transferred per O₂ molecule (n) at 0.6 V vs. RHE are listed in Table 6.4. Apparently, the ORR mechanism on the catalysts Pt/CNTs, Pt/CNTs_HT, Cu@Pt_600, Cu@Pt_1h, and Cu@Pt_4h is dominated by a 4-electron transfer with $n \geq 3.6$ (i.e. O₂ to H₂O is the predominant reaction), and with a dominate 2-electron transfer for the catalysts Cu@Pt_800 and Cu@Pt_1000 with $n < 3$ (i.e. O₂ at most reduced to H₂O₂).

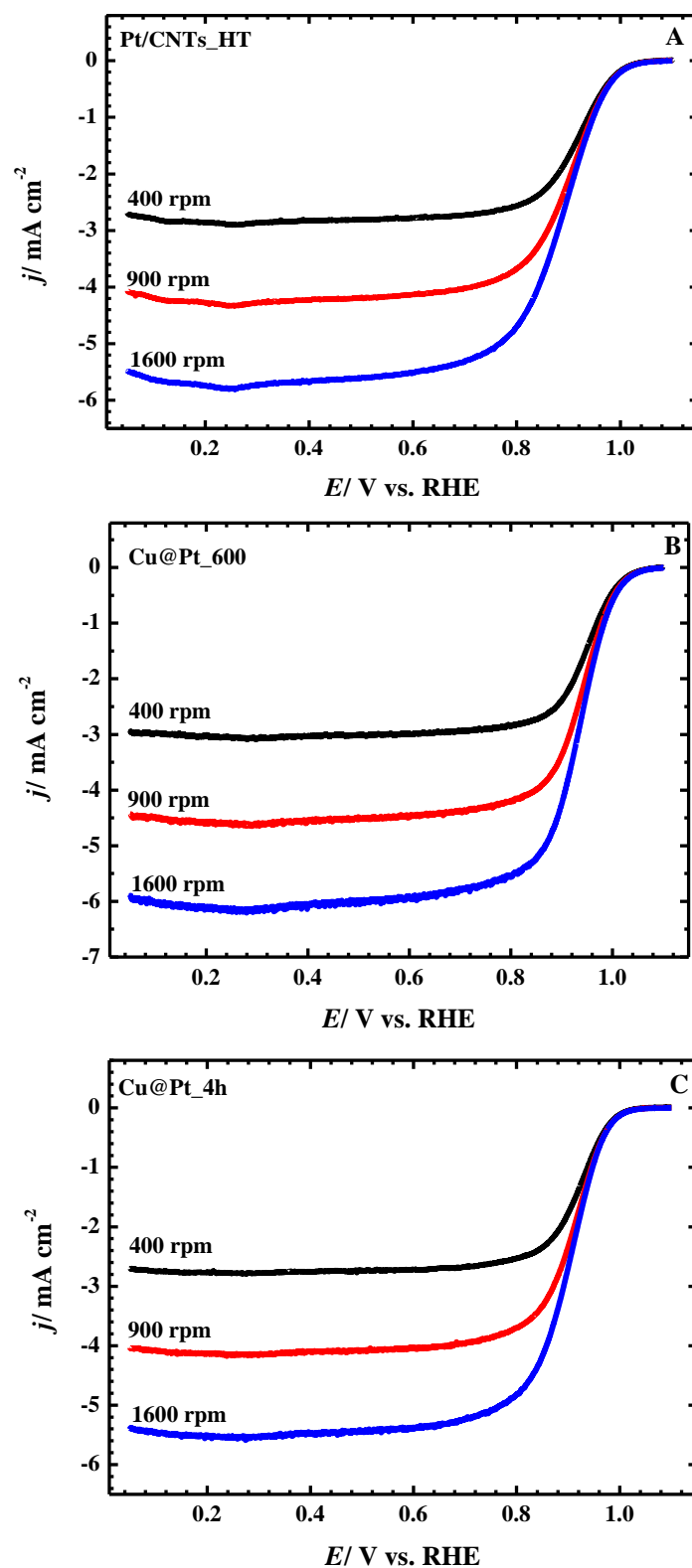


Figure 6.8: ORR polarization curves of different catalysts conducted in O_2 -saturated 0.1 M HClO_4 at various rotation speed and scanning rate of 5 mV s^{-1} .

The half wave potential ($E_{1/2}$) is one of the kinetic parameters that distinguishes the catalytic activity for a set of catalysts and is defined as the potential at which the current density reaches half its diffusion-limited value. $E_{1/2}$ for all catalysts is calculated from the ORR polarization curve for all catalysts at rotation rate of 900 rpm. The values for $E_{1/2}$ are listed in Table 6.4. From Figure 6.9B and the values tabulated in Table 4, the $E_{1/2}$ exhibits a considerable positive shift to a higher potential in sequence of: Pt/CNTs < Pt/CNTs-HT < Cu@Pt_1h < Cu@Pt_4h < Cu@Pt_1000 < Cu@Pt_800 < Cu@Pt_600. Obviously, Cu@Pt_600 catalyst possesses improved ORR activity relative to the other catalysts. However, this observation is an insufficient descriptor for ORR activity evaluation; therefore, the electrocatalytic activities for the catalysts were determined by determination of the specific kinetic current (mass activity and surface activity), both values were determined based on the value of kinetic current density (j_k) obtained from Tafel plot. Tafel plots (E vs. $\log j_k$) for all catalysts at the high potential region (higher than the half wave potential to avoid diffusion induced error, ca. $E > 0.9$ V) [135] are given in Figure 6.9C. The figure shows that the ORR kinetics of the Cu@Pt_600 is firmly superior among all the catalysts under investigation. The catalysts exhibit improved ORR kinetics in the same order as $E_{1/2}$. It is worth to mention that, the Tafel slope for pure Pt and Pt-based catalysts in the high potential region is well-known to be ca. 60 mV decade⁻¹ [136], while the extracted Tafel slopes as listed in Table 4 exhibit slight increases, this difference has also been reported in previous literatures [137-139] and could be attributed to the potential dependence of surface adsorption [136, 138]. The kinetic currents ($j_k \times A$, A: electrode surface area) at 0.85 V and 0.9 V were derived from the Tafel plots and used to estimate the mass specific activity (kinetic current normalized by Pt loading) and the surface specific activity (kinetic current normalized by the ECSA_{CO}) of the catalysts for more ORR evaluation, see Table 6.4. A significant improvement in the mass and surface activities of the dealloyed catalysts relative to pure Pt catalysts was observed suggesting that the dealloyed catalysts are adequate for oxygen reduction electrocatalysis. The enhanced activity for the dealloyed catalysts compare with their pure Pt counterpart could be attributed to the formation of a Pt-rich surface in combination with a PtCu core giving rise to a surface lattice strain resulting in a downshift in the d-band center which reduce the interaction between the oxygen containing species and Pt surface during the ORR [24]. Notably, the electrochemically dealloyed Cu@Pt_600 catalyst shows ca. 3 fold mass activity improvement than the pure Pt catalysts and ca. 1.7 fold (at least) than the rest of the dealloyed catalysts at 0.9

V vs. RHE, see Table 6.4. Further, it has been noticed that the chemically dealloyed catalysts, Cu@Pt_1h and Cu@Pt_4h, exhibit slight mass activity improvement compared to the electrochemical dealloyed counterpart, Cu@Pt_1000, as dealloying time increases from 1h to 4 h. The enormous reduction in the mass activity of the catalysts annealed at elevated temperatures higher than 600°C could be because the effect of the particle size growth defeats any beneficial effects of the better alloying [140] which cause decreases in the mass activity whilst, preserving the specific activity. The electro/chemical dealloyed catalysts achieved specific activity ranged between ca. 2.3 to 3.4 fold increments than that exhibited by the pure Pt catalysts.

Table 6.4: Electrochemical kinetics parameters extracted from the ORR polarization curves: the half wave potential ($E_{1/2}$), mass specific activity (i_m), surface specific activity (i_s), average number of electrons (n) at 0.6 V vs. RHE and Tafel slope.

Catalyst	$E_{1/2}$	i_m A/mg ⁻¹		i_s mA/cm ²		n	Tafel slope mVdec ⁻¹
		0.85 V	0.9 V	0.85 V	0.9 V		
Pt/CNTs	0.88	0.328	0.099	0.443	0.134	3.58	73
Pt/CNTs_HT	0.89	0.402	0.138	0.409	0.140	3.7	79
Cu@Pt_600	0.94	0.701	0.288	0.864	0.355	3.98	76
Cu@Pt_800	0.93	0.409	0.165	1.182	0.479	2.9	65
Cu@Pt_1000	0.92	0.276	0.123	0.836	0.373	2.9	66
Cu@Pt_1h	0.90	0.423	0.131	1.258	0.389	3.6	71
Cu@Pt_4h	0.91	0.523	0.163	1.027	0.321	3.6	64

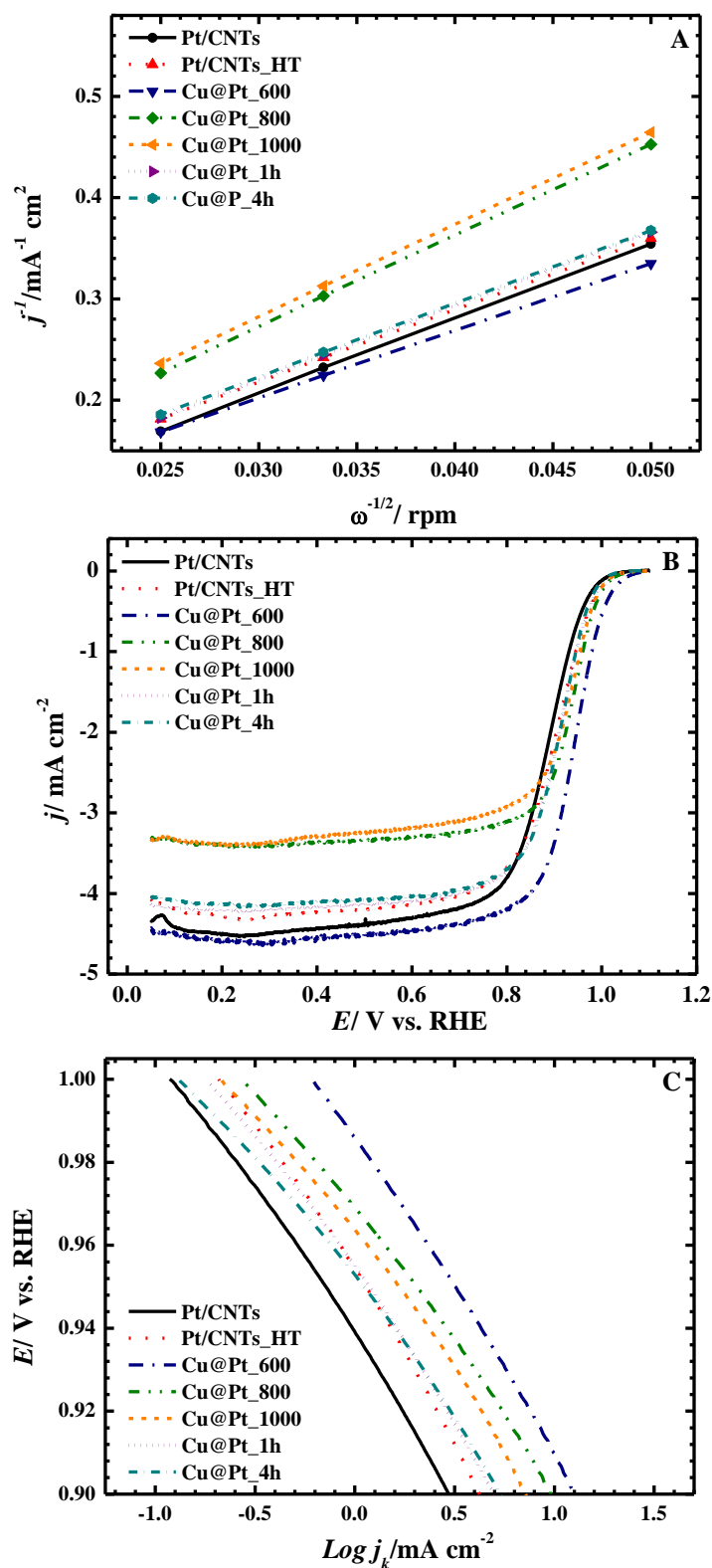


Figure 6.9: A) Koutecky-Levich plots produced from the ORR polarization curves, B) ORR polarization curves of the different catalysts in O_2 -saturated 0.1 M $HClO_4$ at rotation speed of 900 rpm and scanning rate of 5 mV s^{-1} and, C) Tafel plots of the different catalysts.

6.4 Conclusion

Pt nanoparticles supported onto MWCNTs were prepared via microwave-assisted polyol synthesis. Heat treatment of the as-prepared Pt/CNTs in open-air atmosphere at 185°C to remove any remaining PVP traces turned out to be a cardinal process. The electrochemical characterization showed that the as-prepared Pt/CNTs have lower $ECSA_{HUD}$ and a lower ORR activity than the Pt/CNTs_{HT}. The Cu@Pt₆₀₀₋₁₀₀₀ alloys were obtained through a two steps heat treatment protocol executed in H₂/Ar atmosphere. The XRD patterns of the alloyed catalysts clarify the following: i) the synthesized alloys have a face centered cubic structure, ii) increasing the annealing temperature from 600 °C to 1000 °C enhances the alloying and increases the particle size growth and, iii) gradual decreases in the lattice constant combined with shifting the diffraction peaks to a higher 2θ as the annealing temperature increase from 600 to 1000°C, due to the insertion of more Cu atom in the Pt lattice. The primary CVs of the alloyed catalysts illustrate that alloyed catalysts possess Cu-rich surfaces segregation; Pt-rich surfaces were accessible after electro/chemical dealloying as demonstrated from the Pt: Cu atomic ratio determined by the XPS. A discrepancy was found between the $ECSA_{HUD}$ and $ECSA_{CO}$ of the electro/chemical dealloyed catalysts with $Q_{CO}/2Q_H$ ratio greater than unity while, the pure Pt catalysts didn't show such contradiction with $Q_{CO}/2Q_H \approx 1$, which explains the difference in the adsorption properties between the dealloyed catalysts and Pt and also provides an indication of Pt-rich surface formation. The ORR activities were investigated using the RDE technique; the electro/chemical dealloyed catalysts were shown to possess improved ORR activity relative to pure Pt/C ETEK and their Pt/CNTs counterparts catalysts. In particular, the electrochemical dealloyed Cu@Pt₆₀₀ catalyst which showed higher catalytic activity in terms of mass and surface specific activities.

6.5 Supporting information

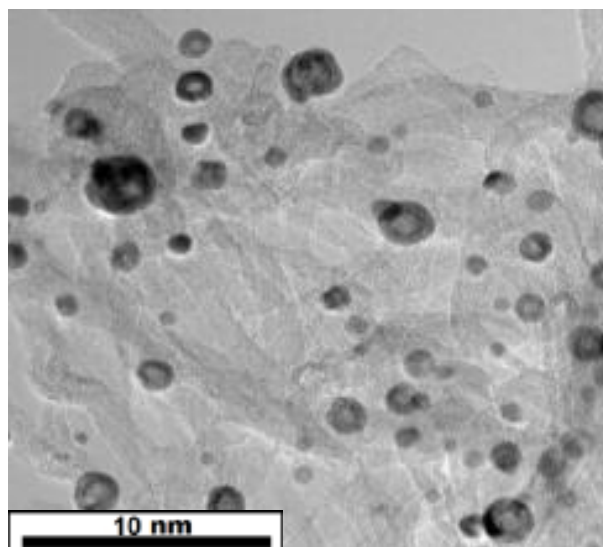


Figure SI 6.1: HRTEM of Cu@Pt_4h catalyst.

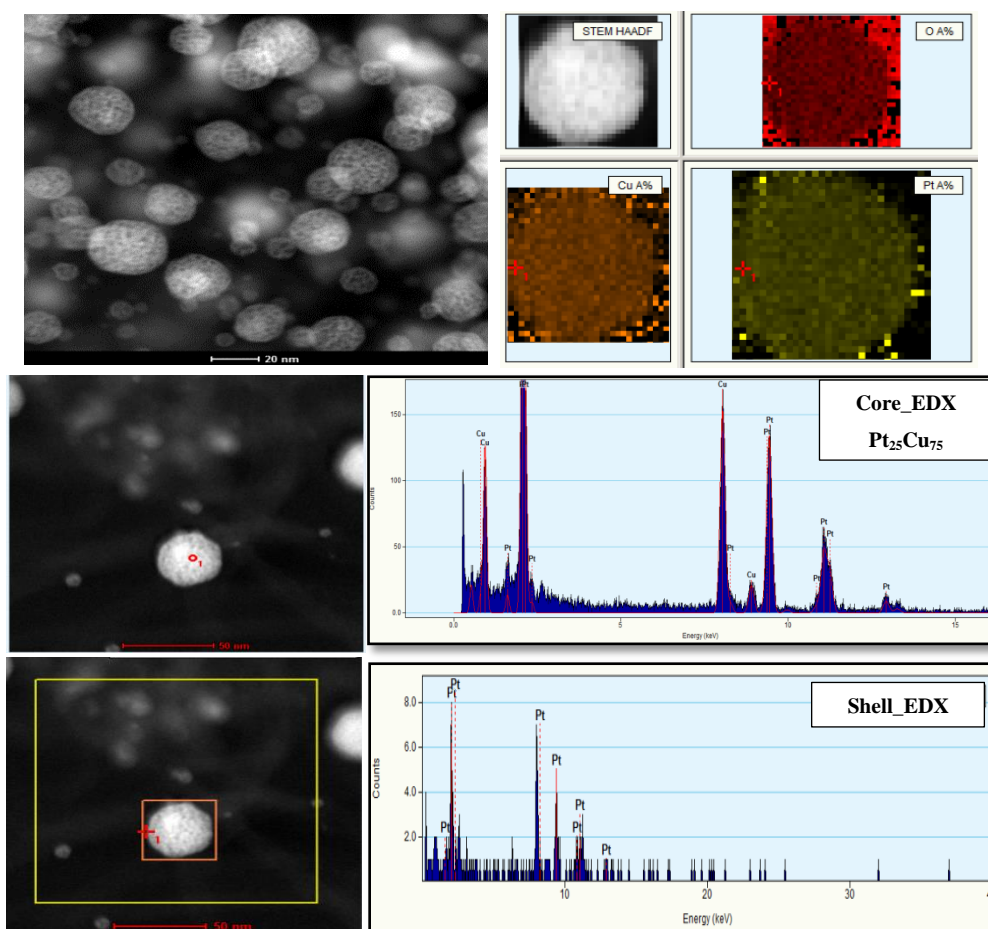


Figure SI 6.2: EDX-STEM analysis of the chemical dealloyed Cu@Pt_4h catalyst.

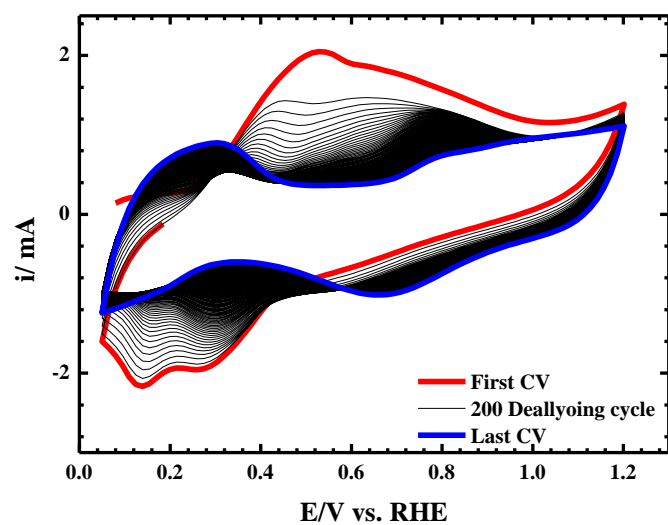
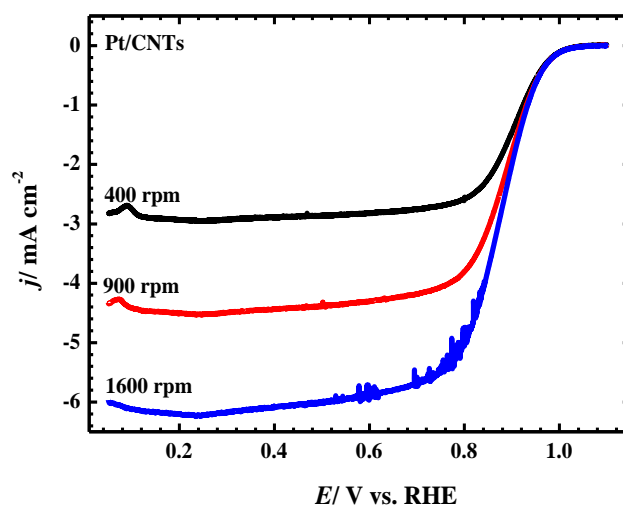


Figure SI 6.3: Dealloying cycles of the Cu@Pt₆₀₀ catalyst, the segregated Cu surface was completely absent after performing 200 CVs with sweep rate of 200 mV s^{-1} in N_2 -saturated 0.1M HClO_4 solution resulting in a stable Pt-like CV profile.



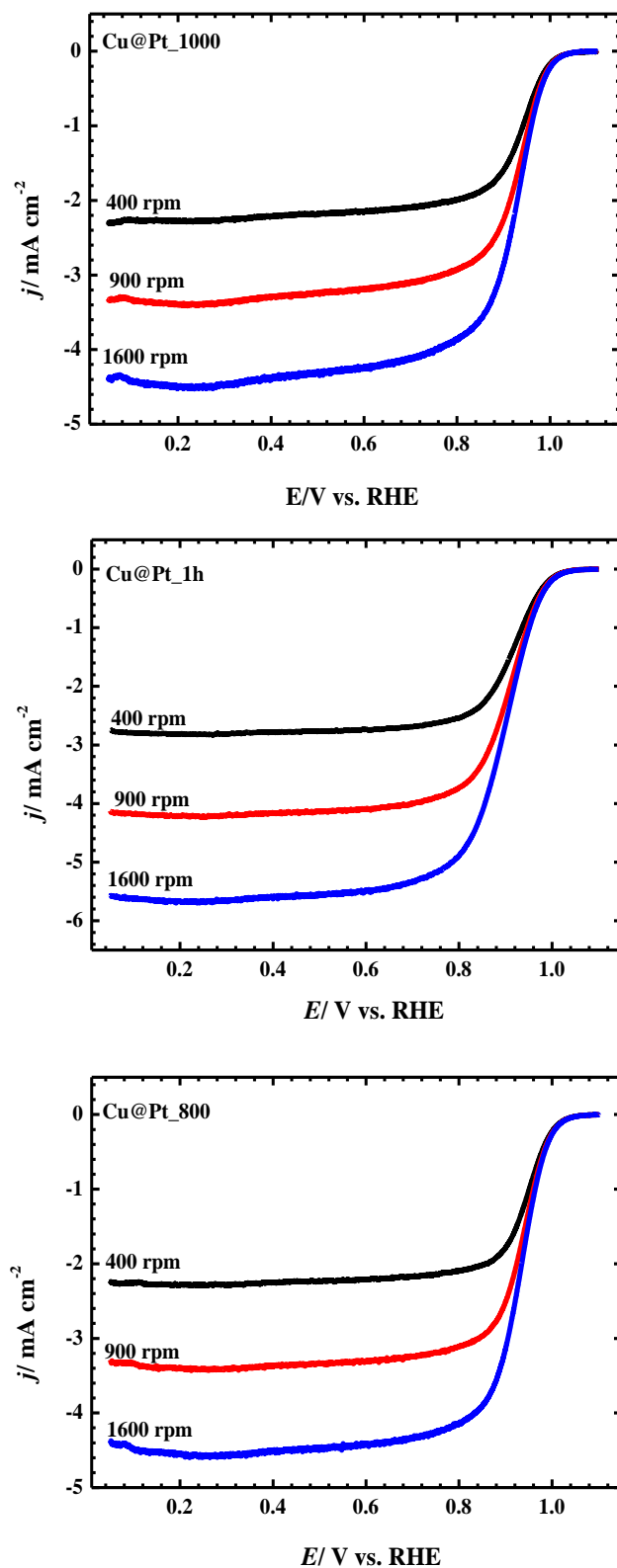


Figure SI 6.4: ORR polarization curves of the different catalysts in O_2 -saturated 0.1M HClO_4 at various rotation speed and scanning rate of 5 mVs^{-1} .

7 General Discussion

The polymer electrolyte membrane fuel cell (PEMFC) is a promising technology supplying electricity by converting the energy stored in chemical compounds into electrical energy with higher efficiency than combustion engines. However, the mass-market introduction of PEMFCs faces several obstacles among which are the high cost (PEMFC use Pt/C as a catalyst; Pt is a scarce and expensive metal) and the kinetic limitation of the oxygen reduction reaction (ORR) at the cathode side [28]. In this context, this dissertation addresses these two obstacles via synthesis of PtCu core-shell catalysts through chemical or electrochemical dealloying of PtCu bimetallic alloy nanoparticles in acidic medium, and investigates their ORR activity. However, “*why are Pt-based core-shell catalysts expected to overcome those obstacles?*” Alloying platinum with non-noble metals such as the 3d-metals decreases the amount of necessary Pt and thus the commercial challenges besides improving the ORR kinetics. The improved ORR kinetics originates from the changes occurs in the electronic and geometrical structure of the Pt lattice due to alloying.

Synthesizing PtCu alloy nanoparticles with high degree of alloying, small particle size and high activity for the ORR remains a challenge. In this dissertation, microwave-assisted polyol reduction is used for the first time for the synthesis of PtCu alloy systems. In the polyol process, the metal precursor is dispersed in a liquid polyol such as the commonly used ethylene glycol (EG). Three strategies have been developed sequentially for PtCu alloy nanoparticles synthesis during the experimental progress of this thesis as shown in Figure 7.1. The synthesis parameters such as the addition of PVP, the pH value, reduction conditions and alloying temperatures have been optimized to tune the particle size, morphology and composition of the catalysts to achieve enhanced ORR catalytic activity.

The left column from Figure 7.1 shows the main obstacle emerged during the preparation of PtCu alloy nanoparticles through the “*one-step reduction method*”, which is the low metal loading (the actual loading was ca. half that of the nominal one). At low pH (without EG modification and in presence of PVP) the Cu content was extremely low while the Pt was nearly completely deposited. However beneficially the nanoparticles were spherical and highly dispersed on the O-CNTs. Increasing the pH of the reaction mixture by adding 1 M NaOH/EG and in presence of PVP increased the Cu

content however due to copper species precipitation while the Pt content decreases and the formed nanoparticles were highly agglomerated. It has been reported [91] that PVP as stabilizer may impede nanoparticle deposition onto the support. On the other hand, also for catalyst samples prepared without PVP (PtCu), the metal loading was quite low. The nominal Pt loading is nearly reached however the Cu loading was extremely low. Considering the reduction potentials, it is well known that at least in aqueous solutions Pt ions should be more easily reduced than Cu ($\text{Cu} = \text{Cu}^{+2}$: 0.345 V vs. SHE; $\text{Pt} = \text{PtCl}_6^{-2}$: 0.726 V vs. SHE). Furthermore redox exchange may occur in a way that PtCl_6^{-2} oxidizes already reduced Cu to Cu ions while it is reduced to Pt. Obviously only parts of the Cu ions are finally reduced to Cu during these complex redox equilibria (for more details see chapter 3).

The second preparation strategy, a **“two-steps reduction method”**, (middle column in Figure 7.1), aims to enhance the Cu loading of the PtCu/CNTs catalyst prepared at low pH, namely the PtCu/PVP₆₀₀ catalyst (see chapter 3), while keeping the high Pt loading and the high dispersion on the supporting CNTs by introducing a second reduction step. The additional (first) reduction step was performed by using NaBH₄ as a reducing agent while the second step was accomplished by the polyol reduction where the polyol was agitated either by microwave irradiation or conventional heating. The ICP-OES results of the synthesized catalysts show that the nominal metal loading (30%) has not been accomplished (see chapter 4). As described before the presence/absence of PVP leads to loadings lower than the nominal one. In this case (i.e. two-reduction steps) high metal loadings are achieved in the absence of PVP, but at the price of high agglomeration (Figure SI 4.1). It seems that even with two-reduction steps achieving high metal loadings remains a challenge when PVP is used (for more details see section 4.3.2). However, the two-step reduction method is clearly advantageous compared to the previously used one-step procedure employing only the polyol-reduction step since the relative copper loading is much higher in the two-step approach. It should be mentioned that NaBH₄ reduction alone equally does not lead to high loading.

We could conclude that while the polyol approach is appropriate to prepare monometallic Pt catalysts, it is less suited to prepare PtCu catalysts with a high Cu loading.

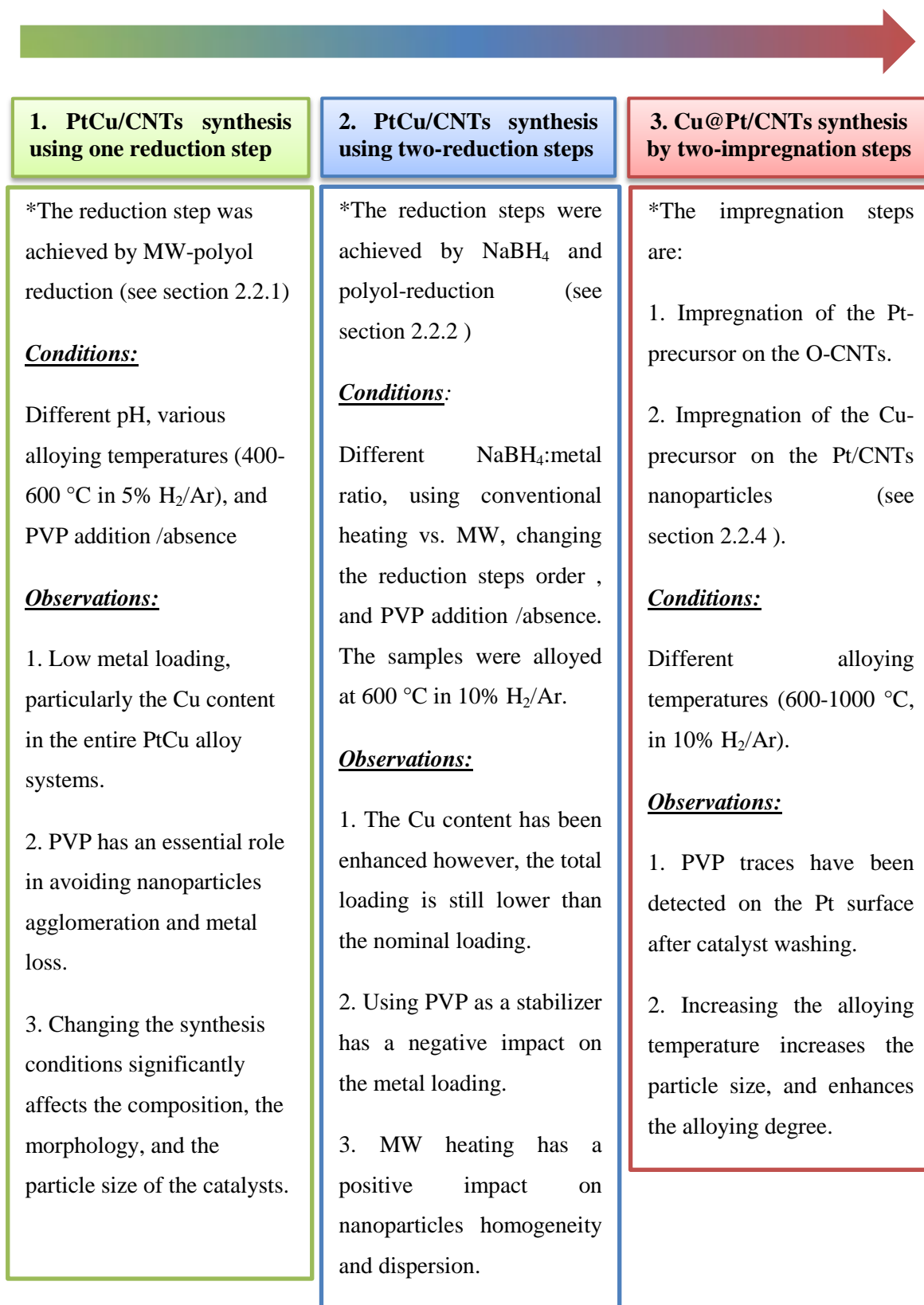


Figure 7.1: Comparison between the PtCu alloy nanoparticles synthesis strategies in terms of the synthesis conditions and observations.

The third strategy “*Cu@Pt/CNTs synthesis by two-impregnation steps*” shown in the right column of Figure 7.1, has been developed in an attempt to reduce the metal loss caused by surfactant addition. In this method Cu@Pt/CNTs catalyst systems have been synthesized through two impregnation steps. The first impregnation step utilizes the benefits of the MW-polyol-reduction (i.e. one reduction step) for the preparation of platinum nanoparticles supported on O-CNTs (Pt/CNTs). The second impregnation step involves Cu impregnation on the supported Pt nanoparticles, see Figure 2.2. However, prior to Cu impregnation the as-prepared Pt/CNTs nanoparticles should be heat treated in an open-air atmosphere at 185 °C for 5 h, to assure the complete removal of any PVP traces remaining after the washing step (for details see chapter 6).

The PtCu alloy nanoparticles prepared by the aforementioned strategies served as precursor materials to form one of the most active kinds of Pt-based alloy catalysts that have been developed for the electroreduction of oxygen over the past decades, namely the Pt-based core-shell-structure catalysts, using the dealloying approach. Dealloying is the selective dissolution of the non-precious metal component to some extent from the alloy leaving behind a structure with an alloy in the core and Pt enriched in the shell and could be carried out chemically or electrochemically (for more details see section 1.3.5).

The dealloying process for preparation of the prospective active catalyst (core-shell) is carried out electrochemically (see chapter 3, 4& 6) and chemically (see chapter 5& 6) in acid solution. Table 7.1 shows the dealloying conditions used for each PtCu alloy catalyst besides highlighting the most efficient catalyst developed by each route towards ORR and comparing its activities with the commercial Pt/C catalyst (20% Pt on carbon Vulcan XC-72) and with other Pt-based bimetallic systems reported in the literature however prepared with different synthesis routes.

Table 7.1: PtCu alloy catalysts, dealloying conditions and the ORR activity with respect to the literatures.

Catalysts	Dealloying Conditions	ORR Activity
<i>one-step reduction method (Chapter 3)</i>		
PtCu/PVP ₆₀₀	*For core-shell structure formation the alloyed catalyst in the form of thin layer electrode was subjected to an <i>electrochemical dealloying</i> step by cycling the electrode in 0.1 M HClO ₄ for 1600 potential cycles in potential window of 0.05-1.2 V vs. RHE and scan rate of 1000 mV s ⁻¹	*Compared with the dealloyed catalysts prepared with the same route, PtCu/PVP_{pH=11} catalyst exhibit the highest mass and surface specific activities. Moreover PtCu/PVP_{pH=11} display mass activity approaching the commercial Pt/C catalyst while, the specific activity was 3 times higher. <i>*Compared to the literature</i> PtCu/PVP_{pH=11} shows higher mass and surface specific activity than those reported for the following catalysts: Pt _x Cu _{1-x} /NCNT [102], Pt _x Pd _{1-x} /MCNTs [103], PtNi@Pt/C [104], PtCo/C, PtCr/C, and PtCoCr/C [105].
PtCu/PVP ₅₀₀		
PtCu/PVP ₄₀₀		
PtCu/PVP_{pH=11}		
PtCu/PVP _{pH=8}		
PtCu		
<i>Two-steps reduction method (Chapter 4)</i>		
PtCu _{10SM}	*For core-shell structure formation the alloyed catalyst in the form of thin layer electrode was subjected to an <i>electrochemical dealloying</i> step by cycling the	*The catalyst PtCu_{50SM} is the most active system towards ORR compared to the other dealloyed PtCu systems prepared by the one or two-steps reduction method, and exhibits 3.3 and 4.3 fold increases in the mass and surface
PtCu _{10SC}		
PtCu_{50SM}		
PtCu _{50MS}		
PtCu _{50S}		

	electrode in 0.1 M HClO ₄ for 1600 potential cycles in potential window of 0.05-1.2 V vs. RHE and scan rate of 1000 mV s ⁻¹	specific activities respectively, compared to the commercial Pt/C catalyst. <i>*Compared to the literature</i> The ORR activities exhibited by the PtCu_{50SM} catalyst was found to be higher than those exhibited by: PtCu catalyst prepared by the polyol method reported in ref. [114], Pt _x M _{1-x} (M = Co, Ni, Cu) catalysts [115], and approaching those demonstrated by PtCo ₃ and PtCu ₃ catalysts [116].
Two-steps reduction method (Chapter 5)		
PtCu _{15min}	*Core-shell structures were obtained by <i>chemical dealloying</i> of the PtCu_{50SM} catalyst in 1 M HClO ₄ for different dealloying times at ambient temperature.	*Chemical dealloying the PtCu_{50SM} (referred to as PtCu in chapter 5) catalyst for 1 h " PtCu_{1h} " is sufficient to yield higher mass and specific activities than the electrochemical approach. *Moreover, increasing or decreasing the dealloying times with respect to 1 h decreases the activity as a result of degradation of the Pt-shell and collapse of the core-shell structure. <i>*Compared to the literatures</i> The PtCu_{1h} exhibits higher ORR activities than those reported in the aforementioned literatures, and displays enhanced activities
PtCu_{1h}		
PtCu _{2h}		
PtCu _{4h}		
PtCu _{6h}		

		compared to the literature values obtained on Pt [122-124] due to the strain effects in the core-shell structures.
<i>Cu@Pt/CNTs synthesis by two impregnation steps (Chapter 6)</i>		
Pt/CNTs	*For core-shell formation, the annealed catalyst in form of a thin layer electrode was subjected to 200 <i>electrochemical dealloying</i> cycles in 0.1 M HClO ₄ at a scan rate of 200 mV s ⁻¹ and in a potential window of 0.05-1.2 V vs. RHE.	*The electro/chemical dealloyed catalysts Cu@Pt_x displayed a significant improvement in the mass and surface activities relative to pure Pt catalysts, suggesting that the dealloyed catalysts are adequate for oxygen reduction electrocatalysis. *The electrochemically dealloyed Cu@Pt₆₀₀ catalyst activity towards the ORR was the optimum; it shows ca. 3 fold mass activity improvement compared to the pure Pt catalysts and ca. 1.7 fold (at least) compared to the other dealloyed catalysts. However, it was lower than the ORR activities displayed by the electro/chemically dealloyed PtCu_{50SM} catalysts <i>Compared to the literatures</i> Cu@Pt₆₀₀ displayed higher ORR activity than those reported in Refs. [102-105,114, 115, 122-124]
Pt/CNTs _{HT}		
Cu@Pt₆₀₀		
Cu@Pt ₈₀₀		
Cu@Pt ₁₀₀₀		
Cu@Pt _{1h}	Cu@Pt₁₀₀₀ catalyst was <i>chemically dealloyed</i> for different times (1 h & 4 h) in 1 M HClO ₄ at room temperature.	
Cu@Pt _{4h}		

In accordance with Table 7.1 the electro/chemically dealloyed catalysts PtCu/PVP_{pH=11}, PtCu_{50SM}, PtCu_{1h}, and Cu@Pt₆₀₀ are the optimum ORR catalysts. Among the mentioned electro/chemical dealloyed catalysts, the PtCu/PVP_{pH=11} catalyst exhibit the lowest electrochemical active surface area (ECSA, estimated from CO) and ORR activities (i.e. mass (i_m) and surface (i_s) specific activities) than the other electro/chemical dealloyed catalysts (see Table 7.2).

Table 7.2: Electrochemical active surface area (ECSA), mass (i_m), and surface (i_s) specific activities of the optimized PtCu catalysts, in comparison with the pure benchmark Pt/C catalyst.

Catalysts	ECSA $\text{m}^2 \text{g}^{-1}_{\text{Pt}}$	i_m $\text{mA mg}^{-1}_{\text{Pt}}$	i_s $\mu\text{A cm}^{-2}$
Pt/C	87.18	94.19	109.04
PtCu/PVP _{pH=11}	24.52	83.72	341.30
PtCu _{50SM}	66.42	305.25	459.41
PtCu _{1h}	95.16	324.88	388.35
Cu@Pt ₆₀₀	82.59	288.00	355.00

The aforementioned catalysts were prepared by various routes however in presence of PVP as a capping agent to keep the nanoparticles physically isolated from each other to prevent agglomeration. The affirmative role of using the PVP in isolating the nanoparticles from each other was apparent on the PtCu_{50SM}, PtCu_{1h}, and Cu@Pt₆₀₀ nanoparticles, the nanoparticles were spherical, uniform, well dispersed on the surface of the supporting material, and were close in sizes (see chapters 4, 5 & 6). However, the PtCu/PVP_{pH=11} nanoparticles shows high extent of agglomeration (see chapter 3), and it was difficult to calculate the mean particle size because of this agglomerations. Such agglomerations were not observed for the PtCu catalysts prepared by the same route (i.e. one-step reduction method) but at lower pH (see section 3.3.2). In accordance with that, the nanoparticles dispersion on the supporting material affects significantly the ECSA and ORR activity of the catalysts and could be controlled by the pH and PVP.

Moreover, the disparity in the catalysts activity towards ORR enhancement could be also explained in terms of metal loading. As stated-above during PtCu alloys preparation the challenge of low Cu loading was observed. Consequently the experimental strategy was varied in order to optimize the loading, particularly the Cu content. For example in case of PtCu_{pH=11} catalyst prepared by the “*one-step reduction method*”, the copper species was in the form of copper oxides and hydroxides as confirmed from XRD (Figure 3.2 in chapter 3), which consequently affect the ORR activity. On the other side, use of a second reduction step by NaBH₄ (“*two-step reduction method*”) enhanced the metallic Cu content and the majority of copper species were in alloyed form with Pt besides pure copper phase however in minor quantity as demonstrated from XRD (Figure 4.1 in chapter 4). Increasing the copper content by using the second reduction affects the electronic and geometrical structure of platinum lattice, i.e. due to incorporation of copper atoms into the platinum fcc structure, which in turn enhances the ORR activity for the electro/chemical dealloyed catalysts prepared by this method, i.e. namely PtCu_{50SM} and PtCu_{1h}.

For the catalyst prepared by the two-step impregnation method, Cu@Pt₆₀₀, although the impregnation step of Pt/CNTs with the copper precursor leads to higher amounts of Cu in the catalyst, the amount of the alloyed Cu was lower than that of PtCu_{50SM} (XRD Figure 6.1 in chapter 6) which is also confirmed from the lattice constant of the catalysts, 3.828 Å versus 3.67 Å for the PtCu_{50SM} catalyst. Increasing the annealing temperature up to 1000 °C enhance the incorporation of Cu atom into the Pt-lattice (lattice constant= 3.67 Å), i.e. as the annealing temperature increase the Cu insertion into Pt-lattice increased, however has an adverse effect on the ECSA and the catalytic activity due to the particle size effect (see section 6.3.2). From this comparative discussion on the methods using in this thesis for the preparation of PtCu alloy as precursors for PtCu core-shell structure catalysts, we can say that one-pot reduction of Pt and Cu precursor is more beneficial for PtCu alloys preparation at lower alloying temperature.

As a general conclusion this dissertation provides a novel approach using the microwave-assisted polyol reduction to prepare improved PtCu electrocatalysts supported on carbon nanotubes for ORR enhancement in polymer electrolyte membrane fuel cells (PEMFCs).

8 Appendices

8.1 Acknowledgment

First and foremost, I am thankful for “Allah Almighty”, the most gracious and the most merciful. I would like to express my sincerely appreciation and gratitude to Prof. Dr. Michael Bron for his untiring support, valuable advices, endless encouragement, great guidance through the past five years, and the last but not the least his great efforts to resolve any problems I had during my stay in Germany.

I am sincerely grateful to Prof. Dr. Wolfgang Grünert, and Dr. Ilya Sinev, for their kind co-operation, performing some XPS measurements and a great help in the interpretation of data.

I would like to express my gratitude to Dr. Abu Bakr Nassr for his help in experimentation and stimulating discussions, which helped to firm up my ideas and concepts. I’m also thankful to Dr. Sabine Schimpf, Eik Koslowski, and Annett Quetschke for their technical support. Appreciation and gratitude to Alexander Hartmann and Matthias Steimecke for their efforts in translating the dissertation abstract to German language. More gratitude and appreciation for the current and former members of professor Bron’s group for their valuable advices and comments

I would like to express my appreciation to Prof. Dr. Michael Bron and the protectorate for structural and strategic development (Grants for foreign female students at the final stage of their PhD) Martin-Luther-University Halle-Wittenberg for the financial support.

A special thanks to my family. Words cannot express how grateful I am to my mother, sister, and brother for all of the good deeds that they’ve made on my behalf. Your prayer for me was what sustained me thus far. I owe a deep appreciation to my beloved husband Abu Bakr, my little princess Aisha and my naughty boy Mohamed whom were always my support in the harsh moments.

At the end immeasurable appreciation and deepest gratitude for all those persons either in Egypt or Germany whom in a way or another made this dissertation possible.

8.2 Curriculum Vitae

Personal Information

Name: Heba Ali Ibrahim Khalil El-Deeb

Date of Birth: 07/06/1981

Nationality: Egyptian

Marital Status: Married

Contact Telephone: +49-017653419831 “Germany”

E-mail: hebaeldeeb2002@gmail.com

heba.el-deeb@chemie.uni-halle.de

Spoken Languages: very good in English, Fair in German, and Arabic (native)

Current Address: Richard-Paulick Straße 1, 06124, Halle (Saale)

Education

2012-up to now: PhD student in Industrial Chemistry at Institute of Chemistry,
Martin Luther University Halle-Wittenberg, Germany

Thesis Title: Synthesis And Characterization of Core-shell Electrocatalysts
for Fuel Cells Application

Supervisor: Prof. Dr. Michael Bron.

2010: M.Sc. in Materials Science, Institute of Graduate Studies and
Research, Alexandria University.

Thesis Title: Preparation and characterization of carbon nanotubes

2007-2009: M.Sc. student, Institute of Graduate Studies and Research,
Alexandria University.

2007: Postgraduate student ‘M.Sc. courses’



2005-2006: Material Science Diploma, Institute of Graduate Studies and Research, Alexandria University, Grade Very Good.

Project Title: Metal Removal from Industrial Waste Water Using
Functionalized Polymer

2004: Training Course in Business Analysis and System Design, Fujitsu.

1998-2002: B.Sc. in Chemistry and physics, Faculty of Science, Alexandria University, General Grade Very Good.

Employment

2005-2010: Assistance Researcher

2010-up to now: Associate Researcher

Employer: Department of Fabrication Technology, Institute of Advanced Technology and New Materials, City of Scientific Research and Technological Application, Alexandria, Egypt.

8.3 List of Publications

8.3.1 Research Articles

1. **Heba El-Deeb**, Ilja Sinev, Wolfgang Grünert, Michael Bron, Electrocatalytic reduction of oxygen on chemically dealloyed PtCu/MWCNTs: influence of dealloying time on structure and activity. *(To be submitted)*
2. **Heba El-Deeb**, Abu Bakr Ahmed Amine Nassr, Ilja Sinev, Wolfgang Grünert, Michael Bron, Enhanced Oxygen Reduction Reaction Activity on Core-Shell Nanocatalysts Synthesized via Dealloying of Cu@Pt/CNTs Catalyst. *(To be submitted)*
3. **Heba El-Deeb**, Michael Bron, Microwave-assisted polyol synthesis of PtCu/carbon nanotube catalysts for electrocatalytic oxygen reduction, Journal of Power Sources 2015, 275, 893-900.
4. **Heba El-Deeb**, Michael Bron, Electrochemical Dealloying of PtCu/CNT Electrocatalysts Synthesised Assisted Polyol-Reduction: Influence of Preparation Parameters on Oxygen Reduction Activity, 2015,164, 315-322.
5. Azza El-Maghraby, **Heba A. El-Deeb** , Mohammed A. Khattab , Influence of FeNi/Al₂O₃ Catalyst Compositions on the Growth of Carbon Nanotubes, Fullerenes, Nanotubes and Carbon Nanostructures journal , 2014, 23 , 27-34.
6. El-Maghraby, **H.A. El Deeb**, Removal of a basic dye from aqueous solution by adsorption using rice hulls, Global NEST Journal, 2011, 13, 90-98.
7. Azza El-Maghraby, **Heba A. El-Deeb**, Different Methods to Derive Pure Silica from Agriculture Waste, International Journal of Environment and Waste Management, 2012, 6, 47-55.

8.3.2 Conferences Contributions

1. Azza El-Maghraby, Mohammed A. Khattab, **Heba A.El-Deeb** , Effect of catalyst composition on the carbon nanotubes growth, The Third Arab International Conference in Physics and Materials Science, 2009.

9 References

- [1] W.R. Grove, On Voltaic Series and the Combination of Gases by Platinum, *Philos. Mag. Third Ser.*, 1839, 14, 127–130.
- [2] W.R. Grove, On a Gaseous Voltaic Battery, *Philos. Mag. Third Ser.*, 1843, 21, 417–420.
- [3] D. Linden, in: D. Linden, T. B. Reddy (Ed.), *Handbook of batteries*, McGraw-Hill Handbooks, 3rd Edition, 2001, P. 1.
- [4] F. Barbir, *PEM Fuel Cells: Theory and Practice*, Elsevier, 1st edition, 2005, P. 1.
- [5] S. Ping Jiang, X. Wang, in: V. V. Kharton (Ed.), *Solid State Electrochemistry II: Electrodes, Interfaces and Ceramic Membranes*, Wiley-VCH Verlag & Co. KGaA., 2011, P. 179.
- [6] M. L. Perry and T. F. Fuller, A Historical Perspective of Fuel Cell Technology in the 20th Century, *J. Electrochem. Soc.*, 2002, 149, 59–67.
- [7] K. Strasser, In: W. Vielstich, H. A. Gasteiger, A. Lamm, H. Yokokawa (Ed.), *Handbook of Fuel Cells—Fundamentals, Technology and Applications*, John Wiley & Sons, 2010, Ch. F304064.
- [8] J. Garche, L. Jörissen, In: W. Vielstich, H. A. Gasteiger, A. Lamm, H. Yokokawa (Ed.), *Handbook of Fuel Cells – Fundamentals, Technology and Applications*, John Wiley & Sons, 2010, Ch. F311105.
- [9] N. M. Markovic, P. N. Ross, Surface Science Studies Of Model Fuel Cell Electrocatalysts, *Surf. Sci. Rep.*, 2002, 45, 117–229.
- [10] C. Song, J. Zhang, in: J. Zhang (Ed.), *PEM Fuel Cell Electrocatalysts and Catalyst Layers: Fundamentals and Applications*, Springer, 2008, P. 89.
- [11] Damjanovic, M. A. Genshaw, J. O. M. Bockris, Distinction between Intermediates Produced in Main and Side Electrode Reactions, 1966, *J. Chem. Phys.*, 45, 4057–4059.
- [12] K. L. Hsueh, D.T. Chin, S. Srinivasan, Electrode Kinetics of Oxygen Reduction, *J. Electroanal. Chem.*, 1983, 153, 79–95.
- [13] N. A. Anastasijevic, V. B. Vesovi, R. R. Adzic, Determination of The Kinetic Parameters of the Oxygen Reduction Reaction Using the Rotating Ring-Disk Electrode, *J. Electroanal. Chem.*, 1987, 229, 305–316.
- [14] K. Kinoshita, *Electrochemical Oxygen Technology*, John Wiley & Sons, 1992, p.19.

- [15] F. Si, Y. Zhang, L. Yan, J. Zhu, M. Xiao, C. Liu, W. Xing, J. Zhang, In: W. Xing, G. Yin, J. Zhang (Ed.), *Rotating Electrode Methods and Oxygen Reduction Electrocatalysts*, Elsevier, 2014, P.133.
- [16] H. S. Wroblowa, Y.C. Pan, G. Razumney, *Electroreduction of Oxygen: A New Mechanistic Criterion*, *J. Electroanal. Chem.*, 1976, 69, 195–201.
- [17] E. Yeager, *Dioxygen Electrocatalysis: Mechanisms in Relation to Catalyst Structure*, *J. Mol. Catal.*, 1986, 38, 5–25.
- [18] P. N. Ross, In: W. Vielstich, H. A. Gasteiger, A. Lamm, H. Yokokawa (Eds.), *Handbook of Fuel Cells—Fundamentals, Technology and Applications*, 2010, John Wiley & Sons, Ltd., Ch. F205035.
- [19] G. J. K. Acres, J. C. Frost, G. A. Hards, R. J. Potter, T. R. Ralph, D. Thompsett, G. T. Burstein, G. J. Hutchings, *Electrocatalysts for fuel cells*, *Catal. Today*, 1997, 38, 393–400.
- [20] J. K. Norskov, J. Rossmeisl, A. Logadotir, L. Lindqvist, J. R. Kitchin, T. Bligaard, *Origin of the Overpotential for Oxygen Reduction at a Fuel-Cell Cathode*, *J. Phys. Chem. B.*, 2004, 108, 17886–17892.
- [21] X. Zi. Yuan, C. Song, H. Wang, J. Zhang, *Electrochemical Impedance Spectroscopy in PEM Fuel Cells*, Springer, 2010, P. 1.
- [22] J. X. Wang, N. M. Markovic, R. R. Adzic, *Kinetic Analysis of Oxygen Reduction on Pt(111) in Acid Solutions: Intrinsic Kinetic Parameters and Anion Adsorption Effects*, *J. Phys. Chem. B*, 2004, 108, 4127–4133.
- [23] H. Liu, D. Xia, J. Zhang, In: J. Zhang (Ed.), *PEM Fuel Cell Electrocatalysts and Catalyst Layers: Fundamentals and Applications*, Springer, 2008, P. 631.
- [24] B. Hammer, J. K. Norskov, *Theoretical Surface Science and Catalysis—Calculations and Concepts*, *Advances in catalysis*, 2000, 45, 71–129.
- [25] L. Xiong, A. Manthiram, *Effect of Atomic Ordering on the Catalytic Activity of Carbon Supported PtM (M= Fe, Co, Ni, And Cu) Alloys For Oxygen Reduction in PEMFS*, *J. Electrochem. Soc.*, 2005, 152, A697–A703.
- [26] P. Mani P, R. Srivastava, P. Strasser, *Dealloyed Pt-Cu Core-Shell Nanoparticle Electrocatalysts for Use in PEM Fuel Cell Cathodes*, *J. Phys. Chem. C*, 2008, 112, 2770–2778.
- [27] U. A. Paulus , A. Wokaun , G. G. Scherer , T. J. Schmidt , V. Stamenkovic , V. Radmilovic , N. M. Markovic , *Oxygen Reduction on Carbon-Supported Pt-Ni and Pt-Co Alloy Catalysts*, *J. Phys. Chem. B*, 2002, 106, 4181–4191.

- [28] H. A. Gasteiger, S.S. Kocha, B. Sompalli, F.T. Wagner, Activity Benchmarks and Requirements for Pt, Pt-Alloy, and Non-Pt Oxygen Reduction Catalysts for PEMFCs, *Appl. Catal. B*, 2005, 56, 9–35.
- [29] M. K. Debe, Electrocatalyst Approaches and Challenges for Automotive Fuel Cells, *Nat.*, 2012, 486, 43–51.
- [30] V. R. Stamenkovic, B. Fowler, B. S. Mun, G. Wang, P. N. Ross, C. A. Lucas and N. M. Markovic, Improved Oxygen Reduction Activity on Pt₃Ni(111) via Increased Surface Site Availability, *Sci.*, 2007, 315, 493–497.
- [31] V. R. Stamenkovic, B. S. Mun, M. Arenz, K. J. J. Mayrhofer, C. A. Lucas, G. Wang, P. N. Ross, N. M. Markovic, Trends in Electrocatalysis on Extended and Nanoscale Pt-Bimetallic Alloy Surfaces. *Nat. Mat.*, 2007, 6, 241–247.
- [32] T. Bligaard, J. K. Nørskov, Ligand Effects in Heterogeneous Catalysis and Electrochemistry, *Electrochim. Acta*, 2007, 52, 5512–5516.
- [33] M. Wakisaka, S. Mitsui, Y. Hirose, K. Kawashima, H. Uchida, M. Watanabe, Electronic Structures of Pt-Co and Pt-Ru Alloys for CO-Tolerant Anode Catalysts in Polymer Electrolyte Fuel Cells Studied by EC-XPS, *J. Phys. Chem. B*, 2006, 110, 23489–23496.
- [34] K. Jiang, H. X. Zhang, S. Zou, W. B. Cai, Electrocatalysis of Formic Acid on Palladium and Platinum Surfaces: From Fundamental Mechanisms to Fuel Cell Applications, *Phys. Chem. Chem. Phys.*, 2014, 16, 20360–20360.
- [35] A. Ruban, B. Hammer, P. Stoltze, H. L. Skriver, J. K. Nørskov, Surface Electronic Structure and Reactivity of Transition and Noble Metals, *J. Mol. Catal. A: Chemical*, 1997, 115, 421–429.
- [36] V. Jalan, E. J. Taylor, Importance of Interatomic Spacing in Catalytic Reduction of Oxygen in Phosphoric Acid, *J. Electrochem. Soc.*, 1983, 130, 2299–2302.
- [37] S. Koh, P. Strasser, Electrocatalysis on Bimetallic Surfaces: Modifying Catalytic Reactivity for Oxygen Reduction by Voltammetric Surface Dealloying, *J. Am. Chem. Soc.*, 2007, 129, 12624–12625.
- [38] V. R. Stamenkovic, B. S. Mun, K. J. J. Mayrhofer, P.N. Ross, N. M. Markovic, Effect of Surface Composition on Electronic Structure, Stability, and Electrocatalytic Properties of Pt-Transition Metal Alloys: Pt-Skin Versus Pt-Skeleton Surfaces, *J. Am. Chem. Soc.*, 2006, 128, 8813–8819.
- [39] J. Greeley, I. E. L. Stephens, A. S. Bondarenko, T. P. Johansson, H. A. Hansen, T. F. Jaramillo, J. Rossmeisl, I. Chorkendorff, J. K. Nørskov, Alloys of Platinum

- and Early Transition Metals as Oxygen Reduction Electrocatalysts, 2009, *Nat. Chem.*, 1, 552–556.
- [40] J. Zhang, M. B. Vukmirovic, K. Sasaki, A. U. Nilekar, M. Mavrikakis, R. R. Adzic, Mixed-Metal Monolayer Electrocatalysts for Enhanced Oxygen Reduction Kinetics, *J. Am. Chem. Soc.*, 2005, 127, 12480–12481.
- [41] U. Nilekar, Y. Xu, J. Zhang, M. B. Vukmirovic, K. Sasaki, R. R. Adzic, M. Mavrikakis, Bimetallic and Ternary Alloys for Improved Oxygen Reduction Catalysis, *Top. Catal.*, 2007, 46, 276–284.
- [42] R. Subramanian, P. E. Denney, J. Singh, M. Otooni, A Novel Technique for Synthesis of Silver Nanoparticles by Laser-Liquid Interaction, *J. Mat. Sci.*, 1998, 33, 3471–3477.
- [43] P. Kumar, R. Kumar, D. Kanjilal, M. Knobel, P. Thakur, K. H. Chae, Ion beam Synthesis of Ni Nanoparticles Embedded in Quartz, *J. Vac. Sci. Technol., B*, 2008, 26, L36.
- [44] L. Hong, R. M. Vilar, W. Youming, Laser Beam Processing of a SiC Particulate Reinforced 6061 Aluminium Metal Matrix Composite, *J. Mat. Sci.*, 1997, 32, 5545–5550.
- [45] C. Dodd, A Comparison of Mechanochemical Methods for the Synthesis of Nanoparticulate Nickel Oxide, *Powder Technol.*, 2009, 196, 30–35.
- [46] W. J. Deng, W. Xia, C. Li, Y. Tang, Formation of Ultra-fine Grained Materials by Machining and the Characteristics of the Deformation Fields, *J. Mater. Process. Technol.*, 2009, 209, 4521–4526.
- [47] M. Salari, S. M. M. khoie, P. Marashi, M. Rezaee, Synthesis of TiO₂ Nanoparticles via a Novel Mechanochemical Method, *J. Alloys Compd.*, 2009, 469, 386–390.
- [48] R. Sasikumar, R. M. Arunachalam, Synthesis of Nanostructured Aluminium Matrix Composite (AMC) Through Machining, *Mater. Lett.*, 2009, 63, 2426–2428.
- [49] O. Sneh, R. B. Clark-Phelps, A. R. Londergan, J. Winkler, T. E. Seidel, Thin Film Atomic Layer Deposition Equipment for Semiconductor Processing, *Thin Solid Films*, 2002, 402, 248–261.
- [50] Y.Y. Wang, K. F. Cai, X. Yao, Facile Synthesis of PbTe Nanoparticles and Thin films in Alkaline Aqueous Solution at Room Temperature, *J. Solid State Chem.*, 2009, 182, 3383–3386.

- [51] S. H. Yoo, L. Liu, S. Park, Nanoparticle Films as a Conducting Layer for Anodic Aluminum Oxide Template-Assisted Nanorod Synthesis, *J. Colloid Interface Sci.*, 2009, 339, 183–186.
- [52] J. Zhang, F. H. B. Lima, M. H. Shao, K. Sasaki, J. X. Wang, J. Hanson, R. R. Adzic, Platinum Monolayer on Nonnoble Metal–Noble Metal Core–Shell Nanoparticle Electrocatalysts for O₂ Reduction, *J. Phys. Chem. B*, 2005, 109, 22701–22704.
- [53] K. Lee, H. Y. Park, H. C. Ham, S. J. Yoo, H. J. Kim, E. Cho, A. Manthiram, J. H. Jang, Reversible Surface Segregation of Pt in a Pt₃Au/C Catalyst and its Effect on the Oxygen Reduction Reaction, *J. Phys. Chem. C*, 2013, 117, 9164–9170.
- [54] D. Wang, H. L. Xin, H. Wang, Y. Yu, E. Rus, D. A. Muller, F. J. DiSalvo, H. D. Abruña, Facile Synthesis of Carbon-Supported Pd–Co Core–Shell Nanoparticles as Oxygen Reduction Electrocatalysts and Their Enhanced Activity and Stability with Monolayer Pt Decoration, *Chem. Mater.*, 2012, 24, 2274–2281.
- [55] R. R. Adzic, F. H. B. Lima, In: W. Vielstich, H. A. Gasteiger, A. Lamm and H. Yokokawa, *Handbook of Fuel Cells – Fundamentals Technology and Applications*, John Wiley & Sons, 2010, Volume 5, Ch. F500001.
- [56] C. Kulp, X. Chen, A. Puschhof, S. Schwamborn, C. Somsen, W. Schuhmann, M. Bron, Electrochemical Synthesis of Core–Shell Catalysts for Electrocatalytic Applications, *ChemPhysChem*, 2010, 11, 2854–2861.
- [57] C. Kulp, K. Gillmeister, W. Widdra, M. Bron, Synthesis of CuCorePtShell Nanoparticles as Model Structures for Core–Shell Electrocatalysts by Direct Platinum Electrodeposition on Copper, *ChemPhysChem*, 2013, 14, 1205–1210.
- [58] X. Li, Q. Chen, I. McCue, J. Snyder, P. Crozier, J. Erlebacher, K. Sieradzki, Dealloying of Noble-Metal Alloy Nanoparticles, *Nano Lett.*, 2014, 14, 2569–2577.
- [59] P. Strasser, S. Gorer, M. Devenney, H. Oyanagi, D. Giaquinta, K. Fukuda, H. Cendak, K. Chondroudis, Platinum-Copper Fuel Cell Electrocatalyst, 2005, PCT International Application, WO2005/024982.
- [60] P. Strasser, In: W. Vielstich, H. A. Gasteiger, A. Lamm, H. Yokokawa, *Handbook of Fuel Cells–Fundamentals, Technology and Applications*, John Wiley & Sons, 2010, Volume 5, Ch. F500003.

- [61] D. Wang, Y. Yu, H. L. Xin, R. Hovden, P. Ercius, J. A. Mundy, H. Chen, J. H. Richard, D. A. Muller, F. J. DiSalvo, H. D. Abruña, Tuning Oxygen Reduction Reaction Activity via Controllable Dealloying: A Model Study of Ordered Cu₃Pt/C Intermetallic Nanocatalysts, *Nano Lett.*, 2012, 12, 5230–5238.
- [62] R. C. Newman, K. Sieradzki, *Metallic Corrosion, Sci.*, 1994, 263 1708–1709.
- [63] D. Wang, H. L. Xin, R. Hovden, H. Wang, Y. Yu, D. A. Muller, F. J. DiSalvo, H. D. Abruña, *Nat. Mater.*, 2013, 12, 82–87.
- [64] M. Luo, L. Wei, F. Wang, K. I. Han, H. Zhu, Gram-Level Synthesis of Core–Shell Structured Catalysts for the Oxygen Reduction Reaction in Proton Exchange Membrane Fuel Cells, *J. Power Sources*, 2014, 270, 34–41.
- [65] H. El-Deeb, M. Bron, Electrochemical Dealloying of PtCu/CNT Electrocatalysts Synthesized by NaBH₄-Assisted Polyol-Reduction: Influence of Preparation Parameters on Oxygen Reduction Activity, *J. Electrochim. Acta*, 2015, 164, 315–322.
- [66] J. Erlebacher, M. J. Aziz, A. Karma, N. Dimitrov, K. Sieradzki, Evolution of Nanoporosity in Dealloying, *Nat.*, 2001, 410, 450–453.
- [67] C. Wang, M. Chi, G. Wang, D. V. Vliet, D. Li, K. More, H. H. Wang, J. A. Schlueter, N. M. Markovic, V. R. Stamenkovic, Correlation Between Surface Chemistry and Electrocatalytic Properties of Monodisperse Pt_xNi_{1-x} Nanoparticles, *Adv. Funct. Mater.*, 2011, 21, 147–152.
- [68] H. El-Deeb, M. Bron, Microwave-Assisted Polyol Synthesis of Pt-Cu/CNTs Catalysts for Electrocatalytic Oxygen Reduction, *J. Power Sources*, 2015, 275, 893–900.
- [69] H. Yue, Y. Zhao, X. Ma, Ji. Gong, Ethylene Glycol: Properties, Synthesis, and Applications, *Chem. Soc. Rev.*, 2012, 41, 4218–4244
- [70] S. E. Skrabalak, B. J. Wiley, M. Kim, E. V. Formo, Y. Xia, On the Polyol Synthesis of Silver Nanostructures: Glycolaldehyde as a Reducing Agent, *Nano Lett.*, 2008, 8, 2077–2081.
- [71] Z. Liu, M. Shamsuzzoha, E. T. Ada, W. M. Reichert, D. E. Nikles, Synthesis and Activation of Pt Nanoparticles With Controlled Size for Fuel Cell Electrocatalysts, *J. Power Sources*, 2007, 164, 472–480.
- [72] D. Li, C. Wang, D. Tripkovic, S. Sun, N. M. Markovic, V. R. Stamenkovic, Surfactant Removal for Colloidal Nanoparticles from Solution Synthesis: the Effect on Catalytic Performance, *ACS Catal.*, 2012, 2, 1358–1362.

- [73] C. Kittel, Introduction to Solid State Physics, 8th Edition., Wiley, New York, 2005, P. 20.
- [74] S. Chen, In: C. G. Zoski, Handbook of Electrochemistry, 2007, Elsevier, 1st Edition, P. 33.
- [75] P. N. Ross, In: J. Lipkowski, P. N. Ross, Electrocatalysis, Wiley-VCH Inc., 1998, P. 43.
- [76] J. Li, In: J. Zhang (Ed.), PEM Fuel Cell Electrocatalysts and Catalyst Layers: Fundamentals and Applications, Springer, 2008, P. 1041.
- [77] F. C. Nart, W. Vielstich, In: W. Vielstich, H. A. Gasteiger, A. Lamm , H. Yokokawa (Ed.), Handbook of Fuel Cells–Fundamentals, Technology and Applications, John Wiley & Sons, 2010, Ch. F203023.
- [78] D. Zhan, J. Velmurugan, M. V. Mirkin, Adsorption/Desorption of Hydrogen on Pt Nanoelectrodes: Evidence of Surface Diffusion and Spillover, J. Am. Chem. Soc., 2009, 131, 14756–14760.
- [79] F. Fiévet F, J.P. Lagier, M. Figlarz, Preparing Monodisperse Metal Powers in Micrometer and Submicrometer Sizes by the Polyol Process, MRS Bull., 1989, 14, 29–34.
- [80] F. Fiévet, J.P. Lagier, B. Blin ,B. Beaudoin ,M. Figlarz , Homogeneous and Heterogeneous Nucleations in the Polyol Process for the Preparation of Micron and Submicron Size Metal Particles , Solid State Ionic , 1989, 32, 198–205.
- [81] F. Fiévet, F. F Vincent, J. P. Lagier, B. Dumont, M. Figlarz, Controlled Nucleation and Growth of Micrometre-Size Copper Particles Prepared by the Polyol Process, J. Mater. Chem., 1993, 3, 627–632.
- [82] X. Li, W.X. Chen, J. Zhao, W. Xing, Z.D. Xu, Microwave Polyol Synthesis of Pt/CNTs Catalysts: Effects of pH on Particle Size and Electrocatalytic Activity for Methanol Electrooxidization, Carbon, 2005, 43 , 2168–2174.
- [83] C. Gabriel, S. Gabriel, E. H. Grant, B. S. J. Halstead , D. M. P. Mingos , Dielectric Parameters Relevant to Microwave Dielectric Heating, Chem. Soc. Rev., 1998, 27, 213–224.
- [84] K. Rao, J. Vaidhyanathan, M. Ganguli, P. Ramkrishnan, Synthesis of Inorganic Solids Using Microwaves, Chem. Mater. 1999, 11, 882–895.
- [85] E. Werner, Systems Biology: the New Darling of Drug Discovery?, Drug Discovery Today, 2002 7, 947–949.

- [86] S. Horikoshi, N. Serpone, *Microwaves in Nanoparticle Synthesis: Fundamentals and applications*, Wiley-VCH Verlag GmbH & Co, 2013, P. 25.
- [87] AB. A. A. Nassr, I. Sinev, M. Pohl, W. Grünert, M. Bron, Rapid Microwave-Assisted Polyol Reduction for the Preparation of Highly Active PtNi/CNTs Electrocatalysts for Methanol Oxidation, *ACS Catal.*, 2014, 4, 2449–2462.
- [88] D. Z. Mezalira, M. Bron, High Stability of Low Pt Loading High Surface Area Electrocatalysts Supported on Functionalized Carbon Nanotubes, *J. Power Sources*, 2013, 231, 113–121.
- [89] Y. Zhao, J.J. Zhu, J.M. Hong, N. Bian, H.Y. Chen, Microwave-Induced Polyol-Process Synthesis of Copper and Copper Oxide Nanocrystals with Controllable Morphology, *Eur. J. Med. Chem.*, 2004, 4072–4080.
- [90] S. Komarneni, R. Pidugu, Q. H. Li, R. Roy, Microwave-Hydrothermal processing of Metal Powders, *J. Mater. Res.*, 1995, 10, 1687–1692.
- [91] W. X. Chen, J. Y. Lee, Z. Liu, Microwave-Assisted Synthesis of Carbon Supported Pt Nanoparticles for Fuel Cell Applications, *Chem. Commun.*, 2002, 21, 2588–2589.
- [92] H. Oh, J. G. Oh, Y. G. Hong, H. Kim, Investigation of Carbon-Supported Pt Nanocatalyst Preparation by the Polyol Process for Fuel Cell Applications, *Electrochim. Acta*, 2007, 52, 7278–7285.
- [93] L. Ren, Y. Xing, Effect of pH on PtRu Electrocatalysts Prepared via a Polyol Process on Carbon Nanotubes, *Electrochim. Acta*, 2008, 53, 5563–5568.
- [94] AB. A. A. Nassr, I. Sinev, W. Grünert, M. Bron, PtNi Supported on Oxygen Functionalized Carbon Nanotubes: in Depth Structural Characterization and Activity for Methanol Electrooxidation, *Appl. Catal. B*, 2013, 142–143, 849–860.
- [95] Dutta, M. K. Carpenter, M. P. Balogh, J.M. Ziegelbauer, T.E. Moylan, M. H. Atwan, N. P. Irish, Electrochemical and Structural Study of a Chemically Dealloyed PtCu Oxygen Reduction Catalyst, *J. Phys. Chem. C*, 2010, 114, 16309–16320.
- [96] L. Su, S. Shrestha, Z. Zhang, W. Mustain, Y. Lei, Platinum–Copper Nanotube Electrocatalyst With Enhanced Activity and Durability for Oxygen Reduction Reactions *J. Mater. Chem. A*, 2013, 1, 12293–12301.

- [97] S.H. Park, H.J. Kim, Unidirectionally Aligned Copper Hydroxide Crystalline Nanorods from Two-Dimensional Copper Hydroxy Nitrate, *J. Am. Chem. Soc.*, 2004, 126, 14368–14369.
- [98] G.H. Du, G.V. Tendeloo, Cu(OH)₂ nanowires, CuO Nanowires and CuO Nanobelts, *Chem. Phys. Lett.*, 2004, 393, 64–69.
- [99] M. Yin, C. K. Wu, Y. Lou, C. Burda, J. T. Koberstein, Y. Zhu, S. O'Brien, Copper Oxide Nanocrystals, *J. Am. Chem. Soc.*, 2005, 127, 9506–9511.
- [100] C. Hsu, C. Huang, Y. Haoa, F. Liu, Synthesis of Highly Active and Stable Au–PtCu Core–Shell Nanoparticles for Oxygen Reduction Reaction, *Phys. Chem. Chem. Phys.*, 2012, 14, 14696–14701.
- [101] N.M. Markovic, H. A. Gasteiger, P. N. J. Ross, Oxygen Reduction on Platinum Low-Index Single-Crystal Surfaces in Sulfuric Acid Solution: Rotating Ring–Pt(hkl) Disk Studies, *J. Phys. Chem.*, 1995, 99, 3411–3415.
- [102] Z. Sun, J. Masa, W. Xia, D. König, A. Ludwig, Z. A. Li, M. Farle, W. Schuhmann, M. Muhler, Rapid and Surfactant-Free Synthesis of Bimetallic Pt–Cu Nanoparticles Simply via Ultrasound-Assisted Redox Replacement, *ACS catal.*, 2012, 2, 1647–1653.
- [103] S. Ghosh, R. K Sahu, C.R. Raj, Pt–Pd Alloy Nanoparticle-Decorated Carbon Nanotubes: a Durable and Methanol Tolerant Oxygen Reduction Electrocatalyst, *Nanotechnology*, 2012, 23, 385602.
- [104] W. Li, P. Haldar, Highly Active Carbon Supported Core-Shell PtNi@Pt Nanoparticles for Oxygen Reduction Reaction, *Electrochem. Solid State Lett.*, 2010, 13, B47–B49.
- [105] M. K. Jeon, Y. Zhang, P. J. McGinn, A Comparative Study of PtCo, PtCr, and PtCoCr Catalysts for Oxygen Electro-Reduction Reaction, *Electrochim. Acta*, 2010, 55, 5318–5325.
- [106] AB. A. A. Nassr, M. Bron, Microwave-Assisted Ethanol Reduction as a New Method for the Preparation of Highly Active and Stable CNT-Supported PtRu Electrocatalysts for Methanol Oxidation, *ChemCatChem.*, 2013, 5, 1472–1480.
- [107] R. J. D. Tilley, *Understanding Solids: The Science of Materials* 2nd Edition, John Willy& Sons Ltd, 2013, P. 115.
- [108] Y. K. Du, P. Yang, Z. G. Mou, N. P. Hua, L. Jiang, Thermal Decomposition Behaviors of PVP Coated on Platinum Nanoparticles, *Appl. Polymer Sci.*, 2006, 99, 23–26.

- [109] M. Ammam, E. B. Easton, PtCu/C and Pt(Cu)/C catalysts: Synthesis, Characterization and Catalytic Activity Towards Ethanol Electrooxidation, *J. Power Sources*, 2013, 222, 79–87.
- [110] P. Strasser, Dealloyed Core-Shell Fuel Cell Electrocatalysts, *Rev. Chem. Eng.*, 2009, 25, 255–295.
- [111] S. Dennis, G. Corrigan, M. J. Weaver, Mechanisms of Formic Acid, Methanol, and Carbon Monoxide Electrooxidation at Platinum Examined by Stray Single Potential Alteration Infrared Spectroscopy, *J. Electroanal. Chem.*, 1988, 241, 143–162.
- [112] M. Oezaslan, F. Hasche, P. Strasser, PtCu₃, PtCu and Pt₃Cu Alloy Nanoparticle Electrocatalysts for Oxygen Reduction Reaction in Alkaline and Acidic Media, *J. Electrochem. Soc.*, 2012, 159, B444–B454.
- [113] J. R. Kitchin, J. K. Norskov, M. A. Barteau, J. G. Chen, Modification of the Surface Electronic and Chemical Properties of Pt(111) By Subsurface 3d Transition Metals, *J. Chem. Phys.*, 2004, 120, 10240–10246.
- [114] C. J. Tseng, S.T. Lo, S. C. Lo, P.P. Chu, Characterization of Pt-Cu Binary Catalysts for Oxygen Reduction for Fuel Cell Applications, *Mater. Chem. Phys.*, 2006, 100, 385–390.
- [115] K. Jayasayee, J. A. R.V. Veen, T. G. Manivasagam, S. Celebi, E. J. M. Hensen, F. A. Bruijn, Oxygen Reduction Reaction (ORR) Activity and Durability of Carbon Supported PtM (Co, Ni, Cu) Alloys: Influence of Particle Size and Non-Noble Metals, *Appl. Catal. B*, 2012, 111, 515–526.
- [116] M. Oezaslan, P. Strasser, Activity of Dealloyed PtCo₃ and PtCu₃ Nanoparticle Electrocatalyst for Oxygen Reduction Reaction in Polymer Electrolyte Membrane Fuel Cell, *J. Power Sources*, 2011, 196, 5240–5249.
- [117] S. Koh, P. Strasser, Dealloyed Pt Nanoparticle Fuel Cell Electrocatalysts: Stability and Aging Study of Catalyst Powders, Thin Films, and Inks, *J. Electrochem. Soc.*, 2010, 157, B585–B591.
- [118] O. Petrova, C. hristian Kulp, M-M Pohl, R. T. Veen, L. Veith, T. Grehl, M. van den Berg, H.H. Brongersma, M. Bron, W. Grünert, Chemical leaching of Pt-Cu/C catalysts for electrochemical oxygen reduction – a study of activity, particle structure, and relation to electrochemical leaching, (Accepted *Chemelectrochem*).

- [119] Y. S. Lee, K. Y. Lim, Y. D. Chung, C. N. Whang, Y. Jeon, XPS core-level shifts and XANES studies of Cu–Pt and Co–Pt alloys, *Surf. Interface Anal.*, 2000, 30, 475–478.
- [120] S. Rudi, C. Cui, L. Gan, P. Strasser, Comparative Study of the Electrocatalytically Active Surface Areas (ECSAs) of Pt Alloy Nanoparticles Evaluated by Hupd and CO-stripping voltammetry, *Electrocatalysis*, 2014, 5, 408–418.
- [121] L. Feng, X. Sun, S. Yao, C. Liu, W. Xing, J. Zhang, in: W. Xing, G. Yin, J. Zhang, *Rotating Electrode Methods and Oxygen Reduction Electrocatalysts*, Elsevier, 2014, P.68.
- [122] J. Speder, L. Altmann, M. Baumer, J. J. K. Kirkensgaard, K. Mortensen, M. Arenz, The Particle Proximity Effect: From Model to High Surface Area Fuel Cell Catalysts, *RSC Adv.*, 2014, 4, 14971–14978.
- [123] J. Speder, L. Altmann, M. Roefzaad, M. Baumer, J. J. K. Kirkensgaard, K. Mortensen, M. Arenz, Pt Based PEMFC Catalysts Prepared From Colloidal Particle Suspensions—a Toolbox for Model Studies, *Phys. Chem. Chem. Phys.*, 2013, 15, 3602–3608.
- [124] M. Nesselberger, M. Roefzaad, R. F. Hamou, P. U. Biedermann, F. F. Schweinberger, S. Kunz, K. Schloegl, G. K. H. Wiberg, S. Ashton, U. Heiz, K. J. J. Mayrhofer, M. Arenz, The Effect of Particle Proximity on the Oxygen Reduction Rate of Size-Selected Platinum Clusters, *Nat. Mat.*, 2013, 12, 919–924.
- [125] M. Oezaslan, F. Hasche, P. Strasser, In Situ Observation of Bimetallic Alloy Nanoparticle Formation and Growth Using High-Temperature XRD, *Chem. Mater.* 2011, 23, 2159–2165.
- [126] K. A. Wepasnick, B. A. Smith, J. L. Bitter, D. H. Fairbrother, Chemical and Structural Characterization of Carbon Nanotube Surfaces, *Anal. Bioanal. Chem.*, 2010, 396, 1003–1014.
- [127] H. El-Deeb, I. Sinev, W. Grünert, M. Bron, Electrocatalytic Reduction of Oxygen on Chemically Dealloyed PtCu/MWCNTs: Influence of Dealloying Time on Structure and Activity.(to be submitted)
- [128] M. Oezaslan, M. Heggen, P. Strasser, Size-Dependent Morphology of Dealloyed Bimetallic Catalysts: Linking the Nano to the Macro Scale, *J. Am. Chem. Soc.*, 2012, 134, 514–524.

- [129] Y. H. Chung, S. J. Kim, D. Y. Chung, H. Y. Park, Y. E. Sung, S. J. Yoo, J. H. Jang, Third-Body Effects of Native Surfactants on Pt Nanoparticle Electrocatalysts in Proton Exchange Fuel Cells, *Chem. Commun.*, 2015, 51, 2968–2971.
- [130] F. Maillard, M. Eikerling, O. V. Cherstiouk, S. Schreier, E. Savinova, U. Stimming, Size Effects on Reactivity of Pt Nanoparticles in CO Monolayer Oxidation: The Role of Surface Mobility, *Faraday Discuss*, 2004, 125, 357–377.
- [131] F. Maillard, E. R. Savinova, U. Stimming, CO monolayer oxidation on Pt nanoparticles: Further Insights into the Particle Size Effects, *J. Electroanal. Chem.*, 2007, 599, 221–232.
- [132] D. F. V. Vliet, C. Wang, D. Li, A. P. Paulikas, J. Greeley, R.B. Rankin, D. Strmcnik, D. Tripkovic, N. M. Markovic, V. R. Stamenkovic, Unique electrochemical Adsorption Properties of Pt-Skin Surfaces, *Angew. Chem.*, 2012, 124, 3193–3196.
- [133] C. Wang, M. Chi, D. Li, D. Strmcnik, D.V. Vliet, G. Wang, V. Komanicky, K. Chang, A. P. Paulikas, D. Tripkovic, J. Pearson, K. L. More, N. M. Markovic, V. R. Stamenkovic, Design and Synthesis of Bimetallic Electrocatalyst with Multilayered Pt-Skin Surfaces, *J. Am. Chem. Soc.*, 2011, 133, 14396–14403.
- [134] C. Wang, D. V. Vliet, K. L. More, N. J. Zaluzec, S. Peng, S. Sun, H. Daimon, G. Wang, J. Greeley, J. Pearson, A. P. Paulikas, G. Karapetrov, D. Strmcnik, N. M. Markovic, V. R. Stamenkovic, Multimetallic Au/FePt₃ Nanoparticles as Highly Durable Electrocatalyst, *Nano Lett.*, 2011, 11, 919–926.
- [135] D. F. Vliet, C. Wang, D. Tripkovic, D. Strmcnik, X. F. Zhang, M. K. Debe, R. T. Atanasoski, N.M. Markovic, V. R. Stamenkovic, Mesostructured Thin Films as Electrocatalysts With Tunable Composition and Surface Morphology, *Nat. Mat.*, 2012, 11, 1051–1058.
- [136] S. Chen, A. Kucernak, Electrocatalysis under Conditions of High Mass Transport Rate: Oxygen Reduction on Single Submicrometer-Sized Pt Particles Supported on Carbon, *J. Phys. Chem. B*, 2004, 108, 3262–3276
- [137] Y. Qian, W. Wen, P. A. Adcock, Z. Jiang, N. Hakim, M. S. Saha, S. Mukerjee, PtM/C Catalyst Prepared Using Reverse Micelle Method for Oxygen Reduction Reaction in PEM Fuel Cells, *J. Phys. Chem. C*, 2008, 112, 1146–1157.
- [138] H. Yang, S. Kumar, S. Zou, Electroreduction of O₂ on uniform Arrays of Pt Nanoparticles, *J. Electroanal. Chem.*, 2013, 688, 180–188.

- [139] C. Coutanceau, M.J. Croissant, T. Napporn, C. Lamy, Electrocatalytic Reduction of Dioxygen at Platinum Particles Dispersed in a Polyaniline Film, *Electrochim. Acta*, 2000, 46, 579–588.
- [140] S. Koha, N. Hahn, C. Yuc, P. Strasser, Effects of Annealing Conditions on Catalytic Activities of Pt-Cu Nanoparticle Electrocatalysts for PEM Fuel Cells, *ECS Trans.*, 2008, 16, 1093–1103.